AD-A172 712 ANALYSES OF THE RAMAN SPECTRA OF THE INCOMMENSURATE FERROELECTRICS RB(2)ZNCL(4) AND K(2)SEO(4)(U) NEBRASKA UNI LINCOLN V KATKANANT ET AL 30 JUN 86 1/2

UNCLASSIFIED ARO-19393.4-PH DAAG29-83-K-0080 F/G 7/4 NL

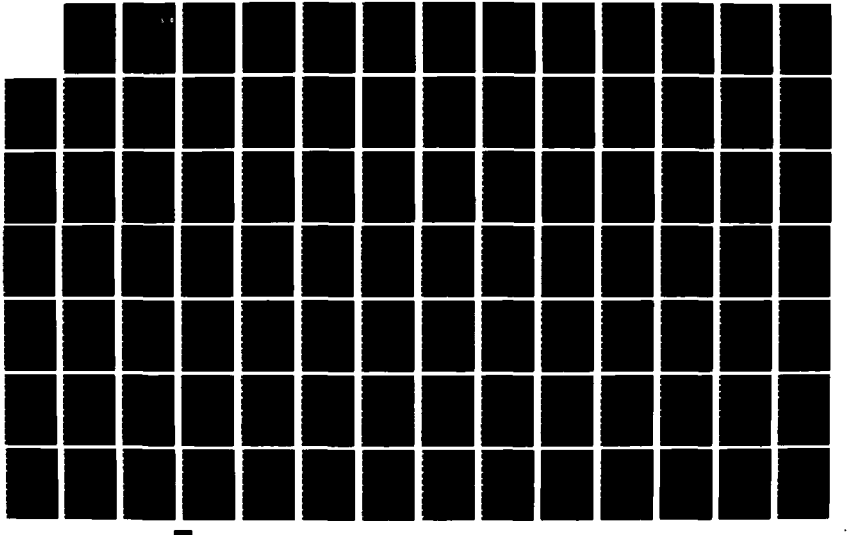

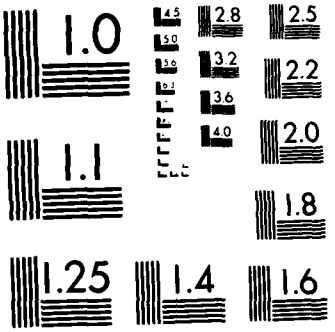

(2)

ANALYSES OF THE RAMAN SPECTRA OF THE INCOMMENSURATE FERROELECTRICS RB_2ZNCL_4 AND K_2SEO_4

INTERIM TECHNICAL REPORT

BY

V. KATKANANT, POST-DOCTORAL RESEARCH ASSOCIATE,

F.G. ULLMAN, PROFESSOR OF ELECTRICAL ENGINEERING AND PHYSICS AND CO-PRINCIPAL INVESTIGATOR,

P.J. EDWARDSON, POST-DOCTORAL RESEARCH ASSOCIATE,

AND

J.R. HARDY, PROFESSOR OF PHYSICS AND CO-PRINCIPAL INVESTIGATOR

JUNE 30, 1986

U.S. ARMY RESEARCH OFFICE
CONTRACT DAAG29-83-K-0080
UNIVERSITY OF NEBRASKA-LINCOLN

UNCLASSIFIED
SECURITY CLASSIFICATION OF THIS PAGE

AD-A172 712

REPORT DOCUMENTATION PAGE

1a. REPORT SECURITY CLASSIFICATION: Unclassified	1b. RESTRICTIVE MARKINGS
2a. SECURITY CLASSIFICATION AUTHORITY	3. DISTRIBUTION/AVAILABILITY OF REPORT: Approved for public release; distribution unlimited.
2b. DECLASSIFICATION/DOWNGRADING SCHEDULE	
4. PERFORMING ORGANIZATION REPORT NUMBER(S)	5. MONITORING ORGANIZATION REPORT NUMBER(S): ARO 19393.4-PH
6a. NAME OF PERFORMING ORGANIZATION: Univ of Nebraska; 6b. OFFICE SYMBOL (If applicable)	7a. NAME OF MONITORING ORGANIZATION: U. S. Army Research Office
6c. ADDRESS (City, State, and ZIP Code): Lincoln, Nebraska	7b. ADDRESS (City, State, and ZIP Code): P. O. Box 12211, Research Triangle Park, NC 27709-2211
8a. NAME OF FUNDING/SPONSORING ORGANIZATION: U. S. Army Research Office; 8b. OFFICE SYMBOL (If applicable)	9. PROCUREMENT INSTRUMENT IDENTIFICATION NUMBER: DAAG29-83-K-0080
8c. ADDRESS (City, State, and ZIP Code): P. O. Box 12211, Research Triangle Park, NC 27709-2211	10. SOURCE OF FUNDING NUMBERS: PROGRAM ELEMENT NO. / PROJECT NO. / TASK NO. / WORK UNIT ACCESSION NO

11. TITLE (Include Security Classification)
Analyses of the Raman Spectra of the Incommensurate Ferroelectrics RB_2ZNCL_4 and K_2SEO_4

12. PERSONAL AUTHOR(S)
V. Katkanant, F. G. Ullman, P. J. Edwardson, J. R. Hardy

13a. TYPE OF REPORT	13b. TIME COVERED	14. DATE OF REPORT (Year, Month, Day)	15. PAGE COUNT
Technical	FROM _____ TO _____	~~September~~ 1986 June 30	57

16. SUPPLEMENTARY NOTATION
The view, opinions and/or findings contained in this report are those of the author(s) and should not be construed as an official Department of the Army positio policy, or decision, unless so designated by other documentation.

17. COSATI CODES		
FIELD	GROUP	SUB-GROUP

18. SUBJECT TERMS (Continue on reverse if necessary and identify by block number)
Raman Spectra, Ferroelectrics, Potassium Selenate
Rubidium Tetrachlorozincate

19. ABSTRACT (Continue on reverse if necessary and identify by block number)

This report describes experimental results on Rb_2ZnCl_4, the analytical procedures, and the results of the analysis. The results are compared with earlier studies on K_2SeO_4 and with the predictions of the model offered previously.

The second chapter describes some new measurements of the potassium selenate internal mode spectra, made with more precise frequency calibration, for comparison with work reported by other laboratories.

20. DISTRIBUTION/AVAILABILITY OF ABSTRACT	21. ABSTRACT SECURITY CLASSIFICATION
☐ UNCLASSIFIED/UNLIMITED ☐ SAME AS RPT. ☐ DTIC USERS	Unclassified
22a. NAME OF RESPONSIBLE INDIVIDUAL	22b. TELEPHONE (Include Area Code) / 22c. OFFICE SYMBOL

DD FORM 1473, 84 MAR — 83 APR edition may be used until exhausted. All other editions are obsolete.

SECURITY CLASSIFICATION OF THIS PAGE
UNCLASSIFIED

THE VIEW, OPINIONS, AND/OR FINDINGS CONTAINED IN THIS REPORT ARE THOSE OF THE AUTHOR(S) AND SHOULD NOT BE CONSTRUED AS AN OFFICIAL DEPARTMENT OF THE ARMY POSITION, POLICY, OR DECISION, UNLESS SO DESIGNATED BY OTHER DOCUMENTATION.

CONTENTS

FOREWORD

Previously, a study (1) of the Raman spectrum of the incommensurate ferroelectric, potassium selenate (K_2SeO_4) was reported from this Laboratory. A qualitative model was proposed in that work to explain the universal observation, that in its paraelectric phase, there is a higher multiplicity of lines in the internal mode spectra (selenium-oxygen vibrations within the selenate tetrahedra) than predicted. The predictions came from conventional symmetry analysis of the x-ray-determined (for the selenate) β-potassium sulfate structure (Pnam). The main features of that qualitative model suggested the true structure to be slightly deviated from the inversion symmetry of the Pnam space group as a result of small rotations (both static and dynamic) of the selenate tetrahedra out of their centrosymmetric positions. Further, it was necessary to postulate that these rotations did not posess translational symmetry but were disordered in the lattice, and that the selenate-selenate coupling was weak, in order to explain the numbers of lines observed in each Raman-scattering configuration.

More recently ~~(i.e., since June, 1983)~~, in addition to refining some of our measurements of the selenate spectra, we have made a detailed study and analysis of the Raman spectra of an isomorph of K_2SeO_4, rubidium tetrachlorozincate (Rb_2ZnCl_4), also known (like K_2SeO_4), to exhibit incommensurate behavior ~~(2,3)~~. This experimental study paralleled (and reinforced) an intensive theoretical study of the lattice dynamics of Rb_2ZnCl_4, to be described elsewhere, but from which calculated Raman peak frequencies were taken and are cited in

this report. (A brief preliminary report of some major results of the theoretical work has been submitted for publication (4)).

In the following sections, we describe our experimental results on Rb_2ZnCl_4, our analytical procedures,and the results of our analysis, and we compare these results with our earlier studies on K_2SeO_4 and with the predictions of the model offered previously and described briefly above.

We also present in a second chapter some new measurements of the potassium selenate internal mode spectra, made with more precise frequency calibration, for comparison with work reported by other laboratories.

Portions of this report are being prepared for the appropriate journals. However, this material is presented also as a technical report since many of the details will be omitted in journal publications because of space limitations.

The authors are especially indebted to their colleague, Professor R. D. Kirby, for many helpful suggestions on instrumentation, and on the analysis and interpretation of the data.

CHAPTER 1

I. INTRODUCTION

Potassium selenate and some of its isomorphs exhibit several phase transitions on cooling from high temperature. One of these phases is incommensurate (modulated structure); it "locks-in" to a ferroelectric phase at its low temperature limit. The discovery of these incommensurate phases in insulator crystals generated a number of studies of these systems by a variety of experimental techniques. Among the ferroelectrics, next to K_2SeO_4, rubidium tetrachlorozincate, Rb_2ZnCl_4, has been the most studied. Results of Raman and infrared spectroscopy (2,5-7), measurements of optical properties combined with dilatometric measurements (8,9), x-ray diffraction (10,11), neutron scattering (12), Cl-NQR and NMR (13,14), and dielectric susceptibility measurements (15-18), have been reported.

Four successive phase transitions have been reported for Rb_2ZnCl_4 between 302 and 74 K (as shown in Table I). Above T_i=302 K, Rb_2ZnCl_4 is paraelectric with space group Pnam (D_{2h}^{16}) (our axes are chosen as c<a<b) with four molecules per unit cell (Z=4). A displacive second-order transition takes place at T_L=189 K to an improper commensurate ferroeelctric phase with space group $Pna2_1$ (Z=12) (C_{2v}^{9}) and a spontaneous polarization P_s // c. Finally, a further transition to a monoclinic structure takes place at T_o=74.6 K; the space group A1a1 (Z=24) has been proposed (12) for this phase.

TBALE I

Crystal Structure and Successive Phase Transitions in Rb_2ZnCl_4

Transition	T	T_0=74.6K	T_1=189K	T_i=302K
Phase	V	IV	III	II
	Antiferro-distortive	Ferroelectric	Paraelectric	Paraelectric
Space Group	A1a1*	$Pna2_1(C_{2v}^9)$ (Commensurate)	(Incommensurate)	$Pnam(D_{2h}^{16})$ (Prototype)
Molecules/ Cell (z)	24	12	~ 12	4
Lattice Constants		3a	~3a	a= 9.257 A
		b	b	b=12.726 A
		c	c	c= 7.282 A
	Monoclinic	Orthorhombic		Orthorhombic

*M. Quilichini and J. Pannetier, Acta Cryst. B39, 657(1983).

In this report, we describe the results of our Raman scattering measurements on Rb_2ZnCl_4 crystals in all four phases. Initially, we undertook a detailed investigation of the Raman spectrum over a wide range of temperature and for all non-redundant scattering geometries. Previous investigations (2,5,6) concentrated on the low frequency part of the spectrum with only minimal information given on the higher frequency portion. Wada et.al.(2) do show the higher frequency spectra at 77 K and 315 K but give no other information. Our objective was to study the complete spectrum at all temperatures of interest. We wished to obtain accurate line frequencies for comparison with the predictions of our theoretical calculations and also to determine in detail the temperature dependence of the internal mode spectrum (i.e., the vibrational modes of the $ZnCl_4^{2-}$ ions).

II. EXPERIMENTAL

Single crystals of Rb_2ZnCl_4 were grown by slow evaporation at room temperature from saturated aqueous solutions containing RbCl and $ZnCl_2$ in a 2:1 molar mixture. Most of these crystals appeared to be striated but otherwise clear. Examination under a microscope revealed the striations to be hollow tubes. It was also observed that the faster the crystal growth rate, the more pronounced were the striations. All crystals used in this study were carefully selected to avoid this crystal-defect. The selected clear crystals were cut and polished into right-angle-sided cubes with the sides parallel to the orthorhombic crystallographic axes. The crystals then were examined between crossed polarizers for light travelling along all three axes to ensure that no twin boundaries were present. The crystals' orientations were determined by comparing the main lines of their room-temperature Raman spectra with those previously-reported (2). Raman measurements were also made on melt-grown crystals obtained from H. Arend, ETH, Switzerland. The Raman spectra from these two different growth sources and processes are identical; the spectra contain no evident signs of crystal-dependence.

The Raman measurements were made using an argon-ion laser as the monochromatic light source operating at either 514.5 nm or 488.0 nm at a power output of 100 mW from the laser. The 488.0 nm laser line was found to give a better signal than the 514.5 nm line, but the experiment was done with both laser lines to determine if there was any interference from laser-plasma fluorescent lines. A block diagram of the Raman spectrometer is shown in Fig. 1. The signal was detected with a Spex model 1401 double monochromator in conjunction with photon

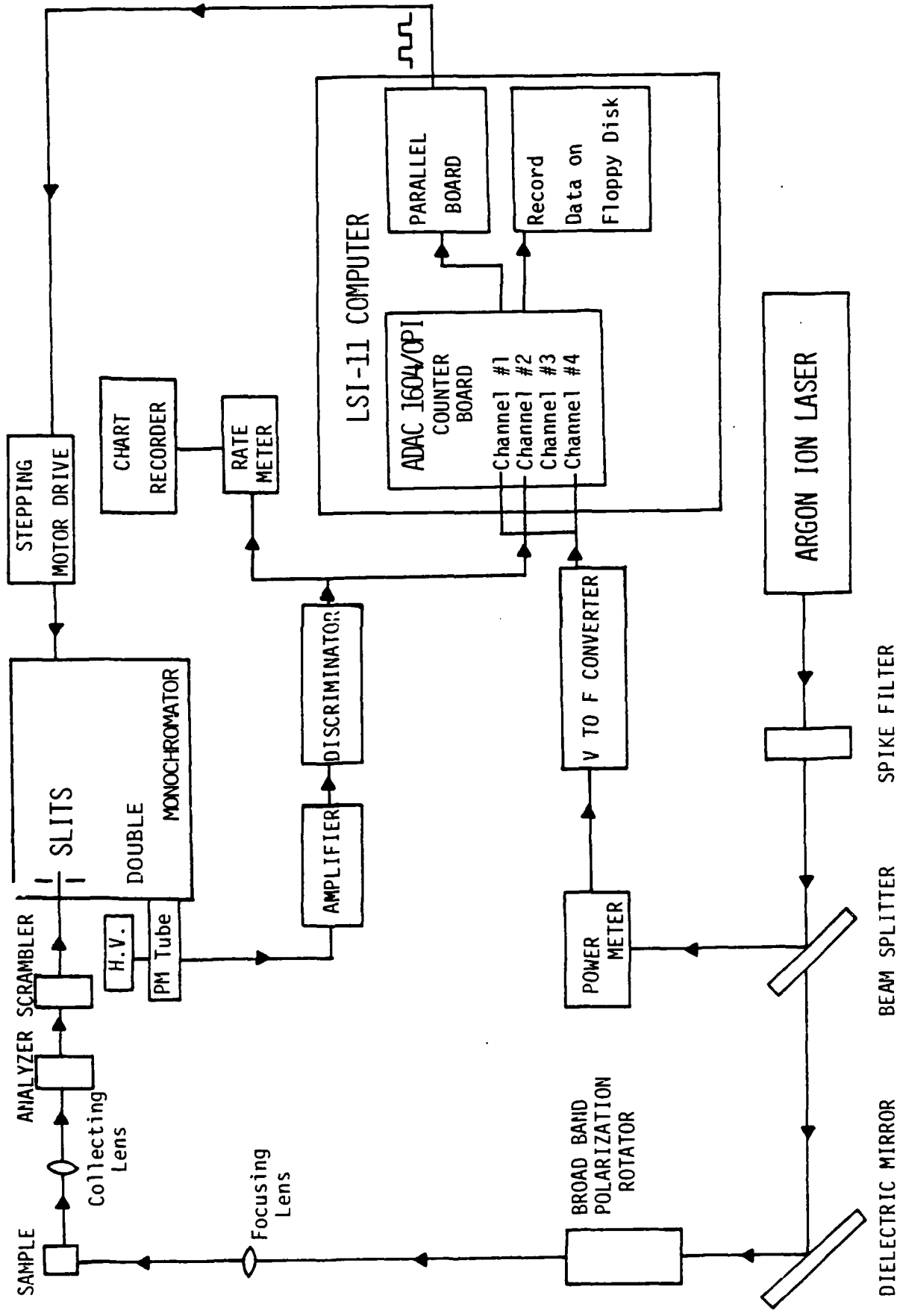

Fig. 1 Diagram of Raman scattering experimental system.

counting electronics. Data were recorded and stored directly on a floppy disk using an on-line LSI-11 minicomputer. This system counts the signal for a pre-selected length of time and the spectrometer is then automatically advanced by a pre-selected step (0.5 wavenumber in our case) to the next frequency where the data accumulation begins again.

In our current and improved data collection system, an ADAC 1604/OPI counter board is mounted in the computer backplane. This board is used to obtain the photon count (correcting for laser power fluctuations) and store it directly in the computer memory. It replaces an Ortec 715, dual counter-timer for which a computer controller was required to interface the counter to the computer. The count is then recorded on floppy disks. With these hardware improvements and rewritten software, the experimenter can automatically skip any undesired spectral region. This results in a more accurate frequency-shift record by eliminating the error which was introduced by the manual scanning that was necessary with the previous system. Furthermore, the process can be interrupted at any time to insert any reference line desired and also to automatically end the scan.

All measurements were made in a right-angle scattering geometry with the polarizations selected to allow each element of the Raman tensor to be obtained separately.

The samples were mounted on a copper substrate on a holder in an exchange-gas-coupled, liquid-nitrogen cryostat for measurements from 77 K to 400 K. Below 77 K, a flowing-gas helium cryostat (19) was

used. Sample temperatures were determined by a platinum resistance thermometer mounted close to the sample. The helium exchange gas ensures good agreement between sample and thermometer temperature but local heating by the incident laser beam can also occur, producing significant temperature changes at the laser beam focus in the sample. Stokes-antiStokes integrated Raman line intensity ratios were measured to estimate the laser beam heating. In most cases, the results suggested that the local heating was insignificant. Further discussion of this is deferred to a later section.

The temperature of the specimen during each scan was kept constant within ±0.5 K by a Wheatstone-bridge heater-controller, shown schematically in Fig. 2. First, we manually let the temperature of the sample settle down to close to the desired temperature and then started the controller which programs the power supply to switch the current to the heater on and off. In the near future, when the writing of the software is completed, an Analog Devices RTI 1251, 12-bit analog-to-digital converter (ADC), which is also directly mounted in the computer backplane, will be used to control the sample temperature. This will increase the precision of the temperature control to within 0.01 K; it also can be programmed to automatically heat or cool the sample between measurements for a sequence of temperatures. This assumes that the measurement scan can be automatically started and stopped with pre-programming as long as the cooling source (liquid nitrogen or liquid helium) is not depleted.

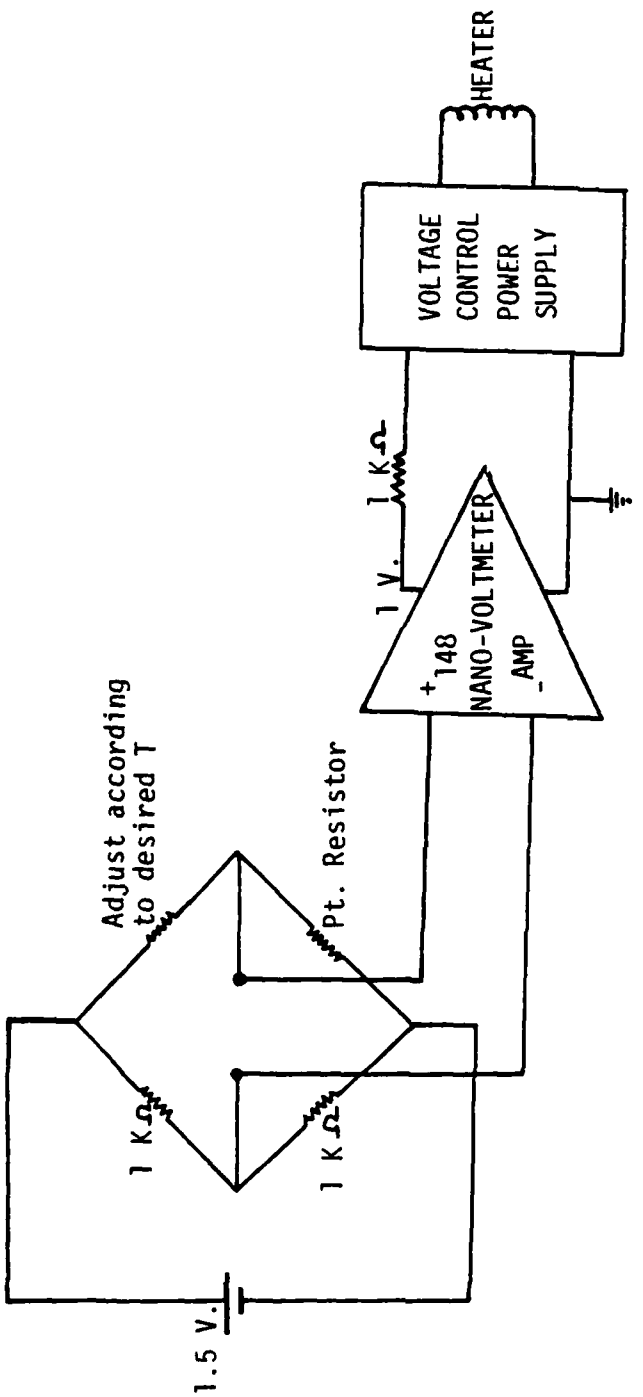

Fig. 2 Constant-temperature control.

III. RESULTS

A. Group Theoretical Analysis

Raman spectroscopy provides a powerful and valuable technique for the study of ferroelectric materials since the structural phase transitions that are associated with the ferroelectricity arise from lattice-dynamical instabilities that are usually Raman-active. To classify the Raman spectra according to the classifications of the zone-center normal modes by their crystal structure symmetries, a group-theoretical analysis should be performed. Most of these details have been derived previously for K_2SeO_4 (20) in its paraelectric phase and also apply to isomorphous Rb_2ZnCl_4: therefore, only a brief summary will be given here.

The symmetries of the Raman-active phonons that can appear in a given scattering geometry can be determined by inspection of the matrix representations of the Raman tensors tabulated by Loudon (21) and by Wallis et.al.(22). Table II shows the Raman tensors for the paraelectic (D_{2h}, T>189 K) and ferroelectric (C_{2v}, T<189 K) phases. The correlation tables for the D_{2h} and C_{2v} point groups and their selection rules are also presented in Table III, below.

TABLE II

RAMAN TENSOR COMPONENTS FOR THE D_{2h} AND C_{2v} POINT GROUPS

Crystal Class	Raman Tensor			
	$\begin{pmatrix} aa & & \\ & bb & \\ & & cc \end{pmatrix}$	$\begin{pmatrix} & ab & \\ ba & & \\ & & \end{pmatrix}$	$\begin{pmatrix} & & ac \\ & & \\ ca & & \end{pmatrix}$	$\begin{pmatrix} & & \\ & & bc \\ & cb & \end{pmatrix}$
D_{2h}	A_g	B_{1g}	B_{2g}	B_{3g}
C_{2v}	$A_1(z)$	A_2	$B_1(x)$	$B_2(y)$

TABLE III

CORRELATION TABLE FOR D_{2h} AND C_{2v}

POINT GROUP AND THEIR RELECTION RULES.

D_{2h}	Selection Rules		C_{2v}	Selection Rules	
A_g		xx(aa), yy(bb) zz(cc)	A_1	T_z	xx(aa), yy(bb) zz(cc)
B_{1g}	R_z	xy(ab)	A_2	R_z	xy(ab)
B_{2g}	R_x^y	xz(ac)	B_2^1	R_x^y	xz(ac)
B_{3g}		yz(bc)	A_2^2		yz(bc)
A_u			A_1^2		
B_{1u}	T_z		B_2^2	T_z	
B_{2u}	T_x^y		B_1^2	T_x^y	
B_{3u}					

From these analyses, it was shown that in the D_{2h} phase, of 81 optic phonons at the zone center, there are 42 Raman-active (gerade) modes, as shown in Table IV.

TABLE IV

SYMMETRY CLASSIFICATION OF THE ZONE-CENTER MODES

FOR Rb_2ZnCl_4 IN THE PARAELECTRIC PHASE (Pnam)

Mode Assignment and Polarization	Number of Internal Modes	Number of External Modes T	L	Optical Activity	Total
A_g (aa,bb,cc)	6	6	1	Raman	13
B_{1g} (ab)	6	6	1	Raman	13
B_{2g} (ac)	3	3	2	Raman	8
B_{3g} (bc)	3	3	2	Raman	8
A_u	3	3	2	not active	8
B_{1u}	3	2	2	Infrared	8
B_{2u}	6	5	1	Infrared	13
B_{3u}	6	5	1	Infrared	13

The acoustic modes are also included in the totals in Column 6 for the B_{1u}, B_{2u}, and B_{3u} modes.

The analysis for the low-temperature phase by the correlation method is shown in Table V.

TABLE V

SYMMETRY CLASSIFICATION FOR THE FERROELECTRIC PHASE

($Pna2_1$) WHICH HAS POINT GROUP C_{2v}.

Mode Assignment and Polarization	Number of Internal Modes	Number of External Modes	Optical Activity	Total
A_1 (aa,bb,cc)	9	11	Raman, ir	21
A_2 (ab)	9	12	Raman	21
B_1 (ac)	9	11	Raman, ir	21
B_2 (bc)	9	11	Raman, ir	21

Note that ir represents an infrared-active mode. Also, the acoustic modes are included in the totals in Column 5 for the A_1, B_1, and B_2 modes.

In this low-temperature phase (T<189 K), the cell of Rb_2ZnCl_4 triples in the "a" direction, so it is expected that there will be three times as many modes in this ferroelectric phase than predicted for the paraelectric phase, i.e., the optic phonons at the zone center should be $62A_1 + 63A_2 + 62B_1 + 62B_2$. Finally, the space group for the lowest-temperature monoclinic phase is not known conclusively. No analysis was made for this phase since any group-theoretical analysis given here would be purely speculative. However, it was reported that in this phase, there are 24 molecules per unit cell (Z=24) and thus, more Raman-active phonons; at least twice the number in the ferroelectric phase are expected.

B. Raman Spectra of the External Modes of Rb_2ZnCl_4

The results of Raman measurements of the external mode spectrum of Rb_2ZnCl_4 is presented in this section. There have been several previous studies of this low-frequency region ranging from about 9-315 K (2,5,8). For completeness, and to check these earlier results, and also to be able to compare these spectra with our lattice-dynamical calculations, a detailed measurement and analysis of the frequencies in this range was made. The following figures, 3a)-3f), show the Raman spectra of Rb_2ZnCl_4 in the 10 to 200 cm^{-1} region in all four successive phases from 20 K up to 315 K for the scattering polarizations (aa), (bb), (cc), (ab), (ac), and (bc) (the first letter in parentheses gives the incident polarization, the second, the scattered polarization). The observed lines which will be discussed below are listed together with the internal modes in the next section. These results are in general agreement with previously reported work (2).

C. Raman Spectra of the Internal Modes of Rb_2ZnCl_4

Unlike K_2SeO_4, the external and internal mode frequencies of Rb_2ZnCl_4 are not well separated. In the low frequency region containing the external modes, there are also internal mode frequencies from the internal vibrations of the tetrahedral $ZnCl_4^{2-}$ ion. Because of this overlap of the external and internal mode spectra, the analysis of the spectra is more difficult and less straightforward than for K_2SeO_4. However, the highest frequency group of four internal modes is well separated from the rest of the spectrum and so, many of our measurements concentrated on this spectral

Fig. 3 Raman spectra of the external modes (10-200 cm^{-1}) of Rb_2ZnCl_4 at 20 K, 100 K, 200 K, room, and 315 K for the

a) A_g modes: b(aa)c

b) A_g modes: a(bb)c

c) A_g modes: a(cc)b

d) B_{1g} mode: (ab)

e) B_{2g} mode: (ac)

f) B_{3g} mode: (bc)

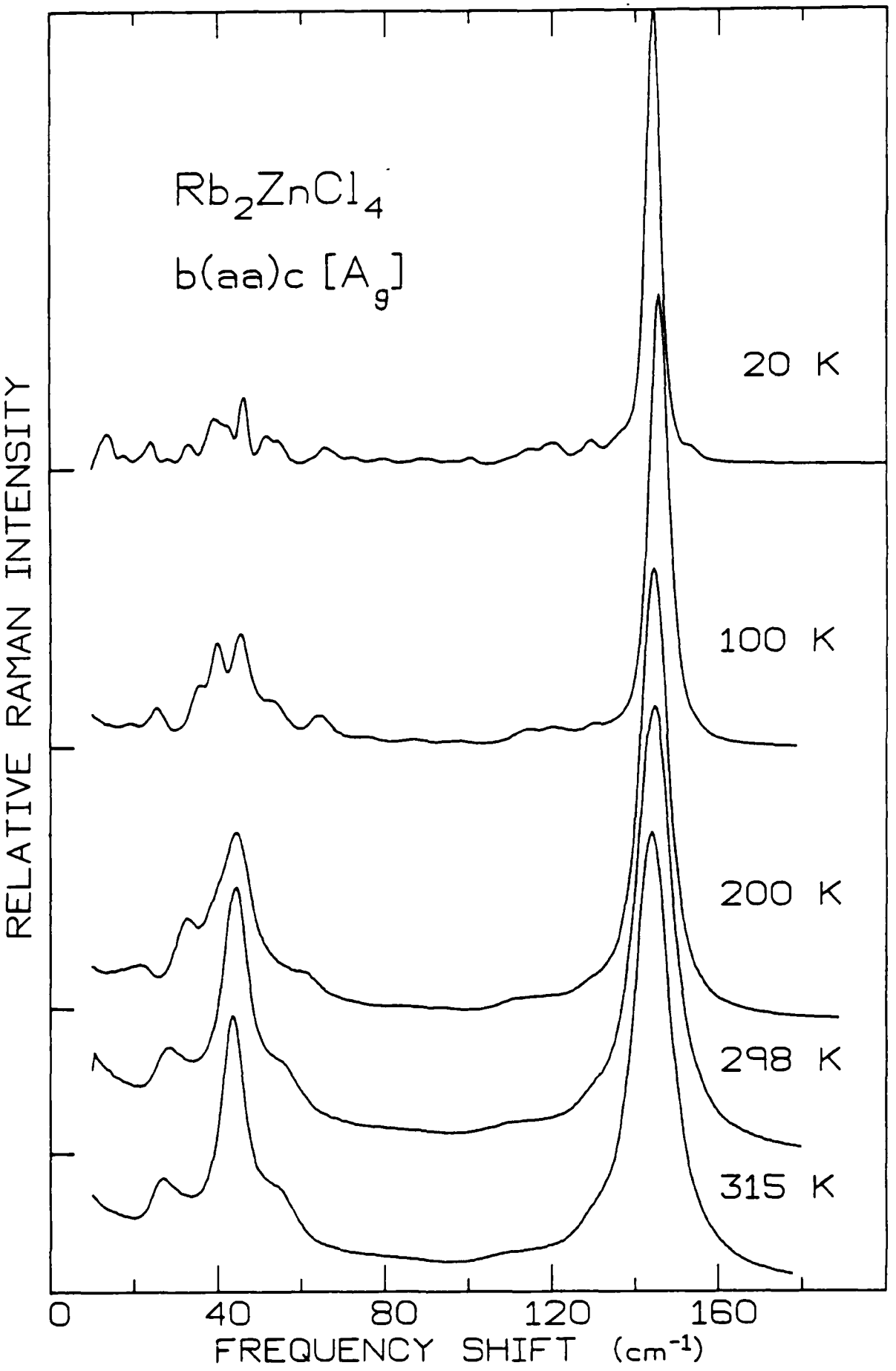
Rb_2ZnCl_4
b(aa)c [A_g]
20 K
100 K
200 K
298 K
315 K
RELATIVE RAMAN INTENSITY
0
40
80
120
160
FREQUENCY SHIFT (cm^{-1})

3a

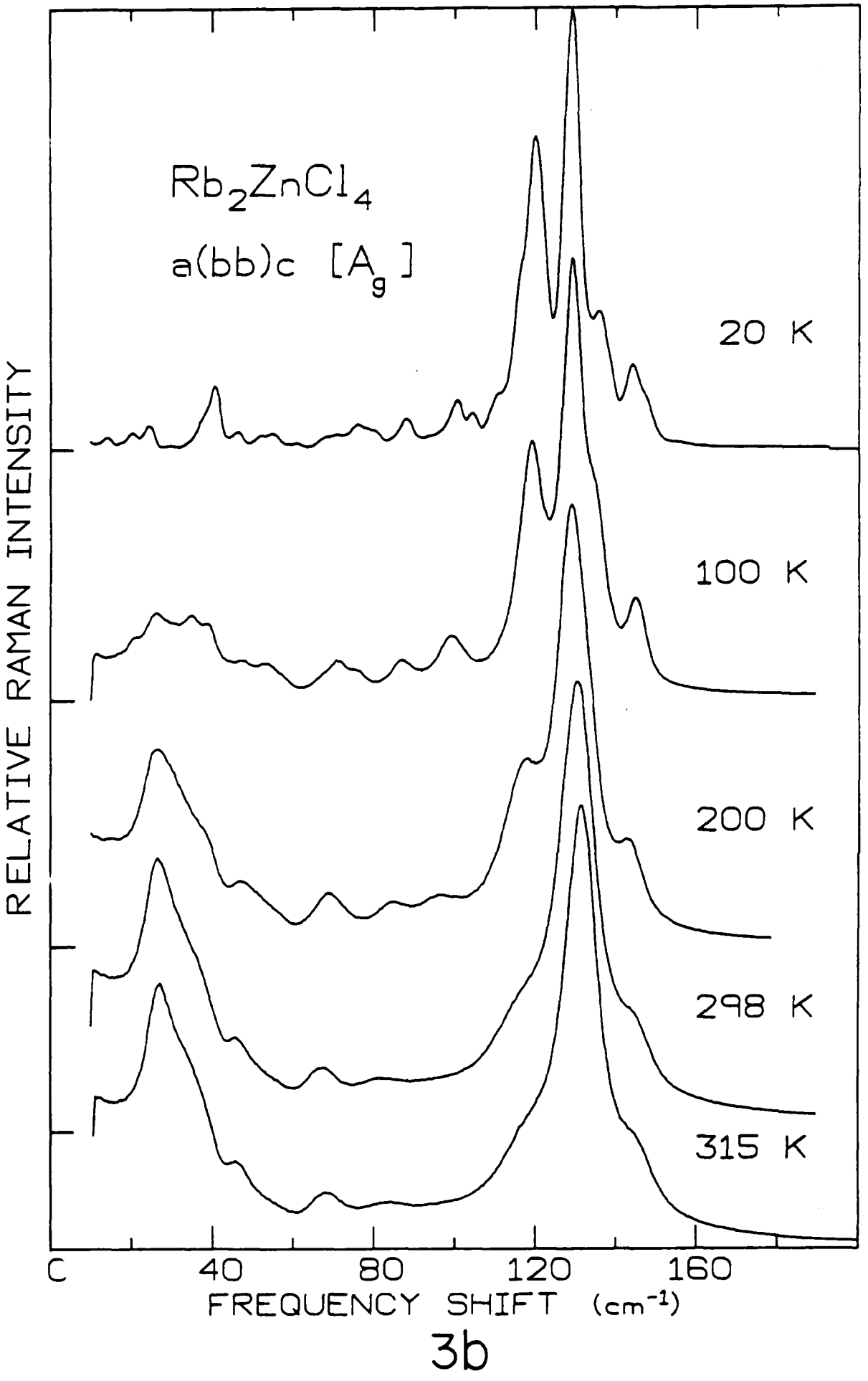
Rb_2ZnCl_4
a(bb)c [A_g]
20 K
100 K
200 K
298 K
315 K
RELATIVE RAMAN INTENSITY
0
40
80
120
160
FREQUENCY SHIFT (cm^{-1})

3b

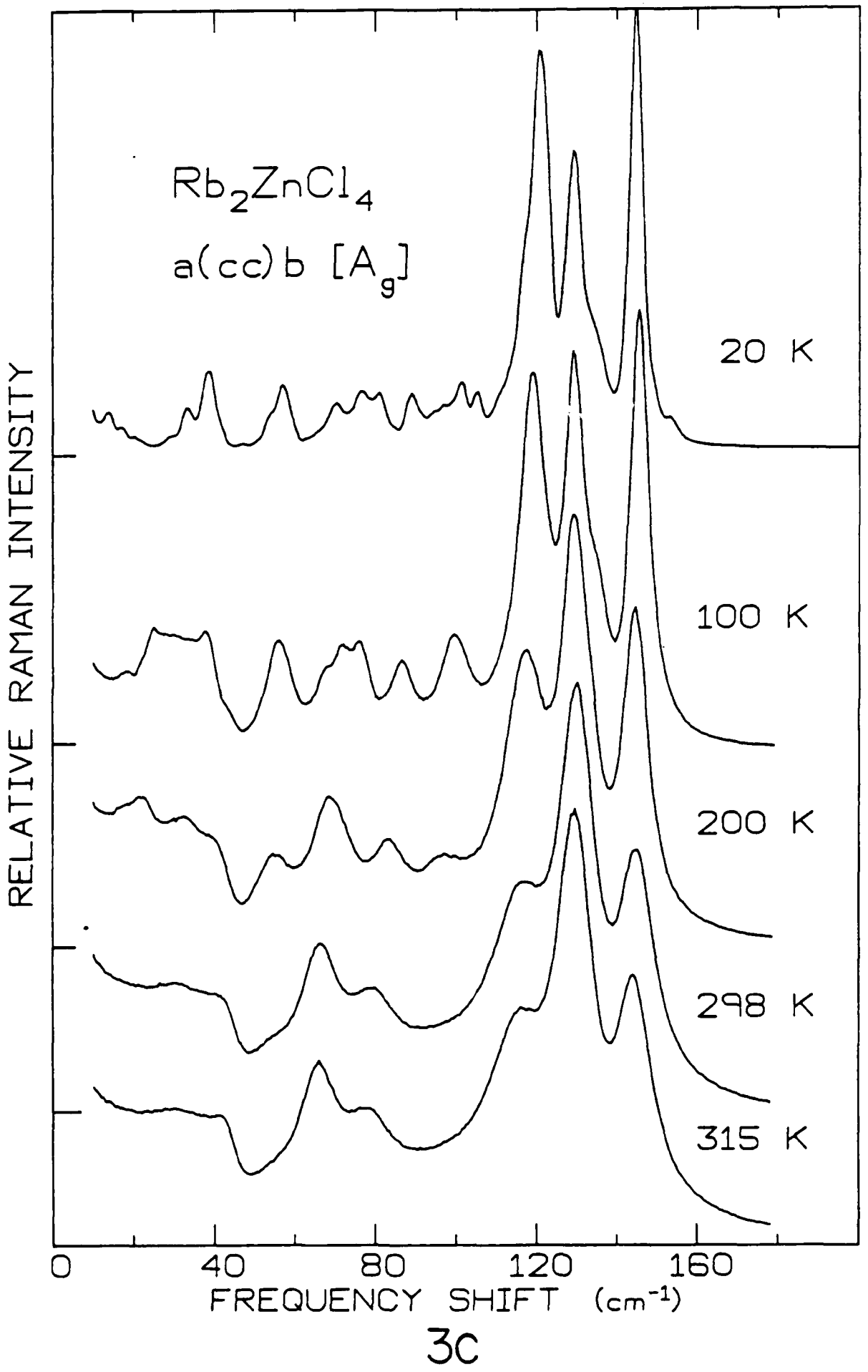
Rb_2ZnCl_4
a(cc)b [A_g]
20 K
100 K
200 K
298 K
315 K
RELATIVE RAMAN INTENSITY
0
40
80
120
160
FREQUENCY SHIFT (cm^{-1})

3C

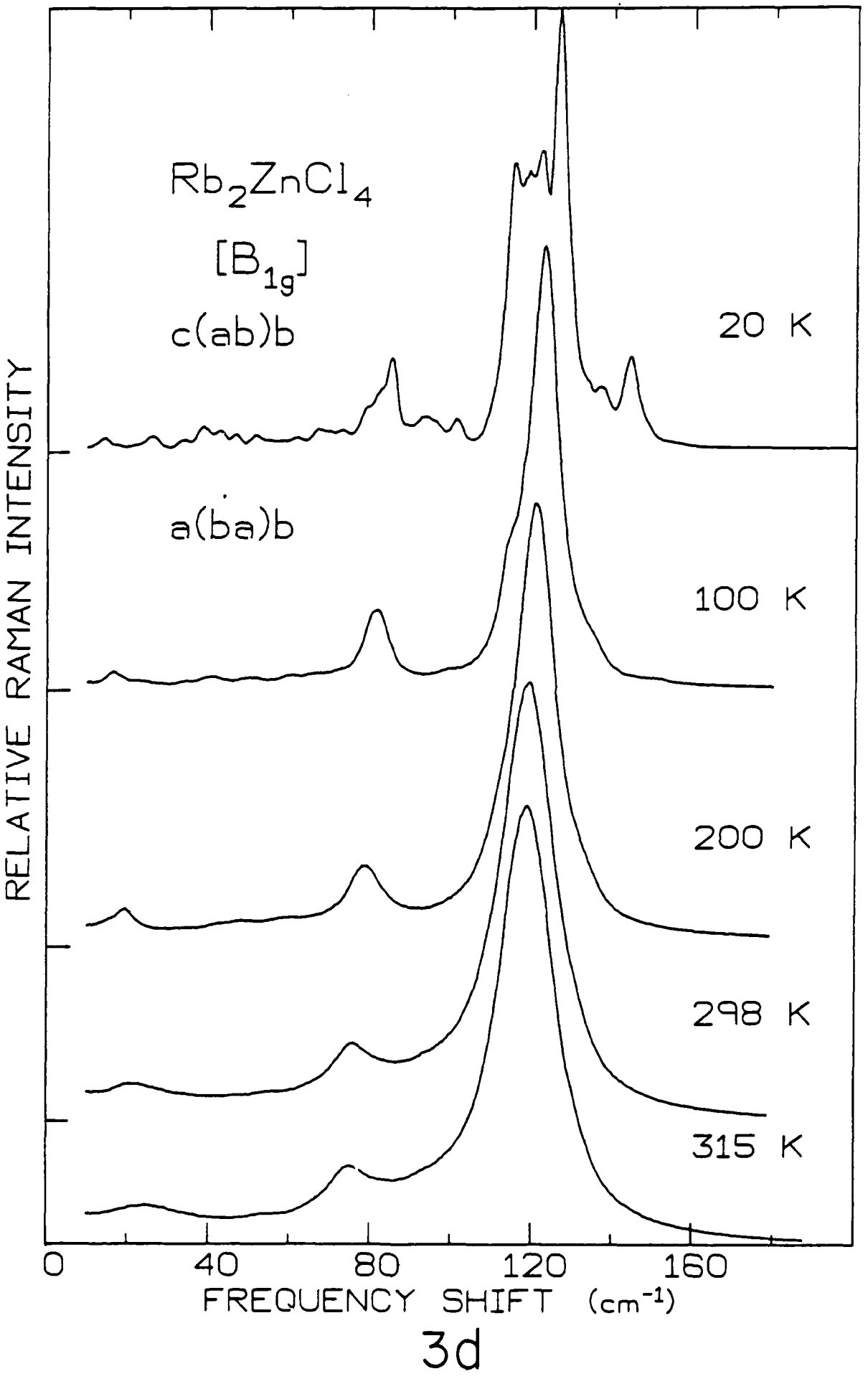
Rb_2ZnCl_4
$[B_{1g}]$
c(ab)b
a(ba)b
20 K
100 K
200 K
298 K
315 K
RELATIVE RAMAN INTENSITY
0
40
80
120
160
FREQUENCY SHIFT (cm^{-1})

3d

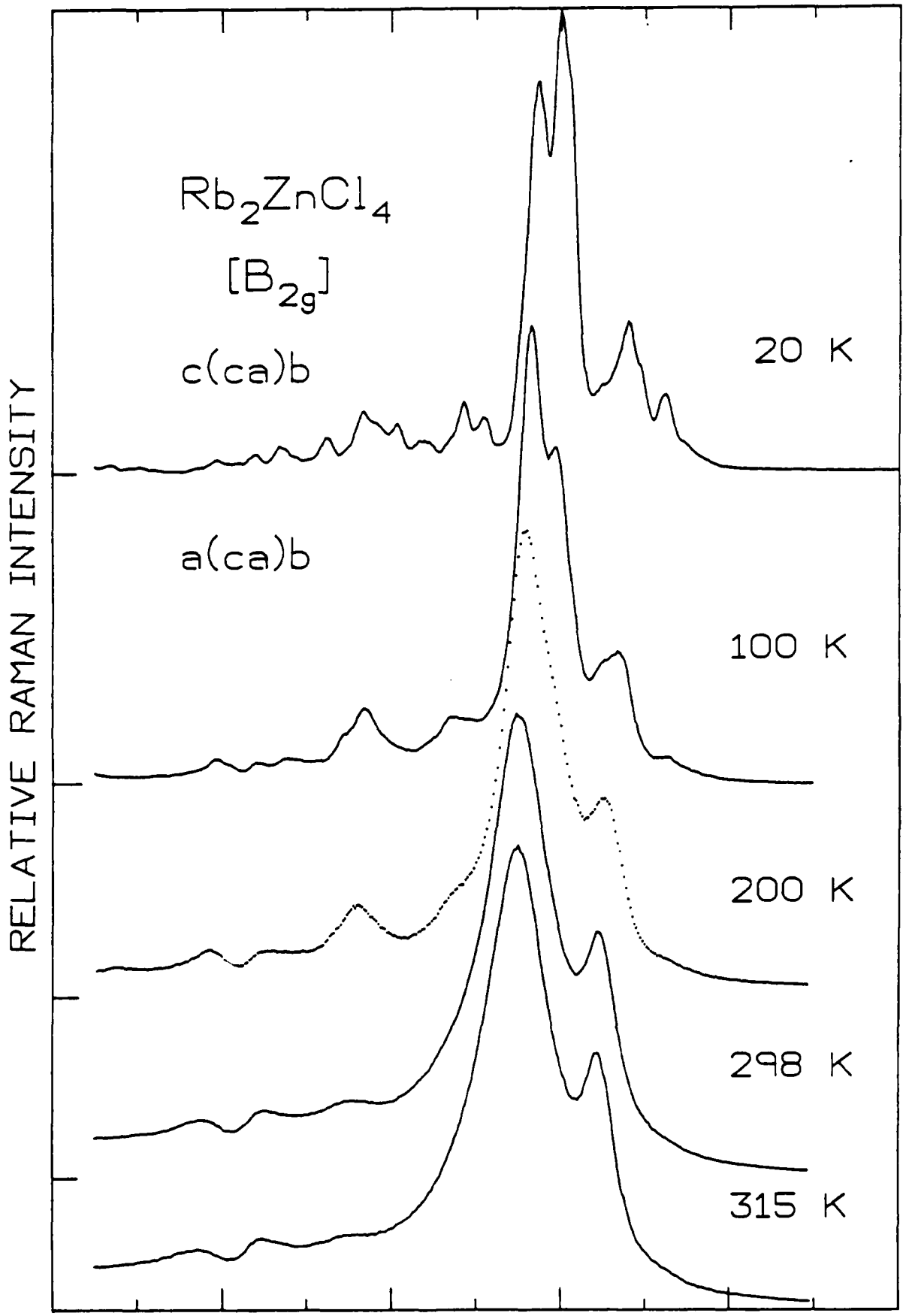
Rb_2ZnCl_4
$[B_{2g}]$
c(ca)b
a(ca)b
20 K
100 K
200 K
298 K
315 K
RELATIVE RAMAN INTENSITY
0
40
80
120
160
FREQUENCY SHIFT (cm^{-1})

3e

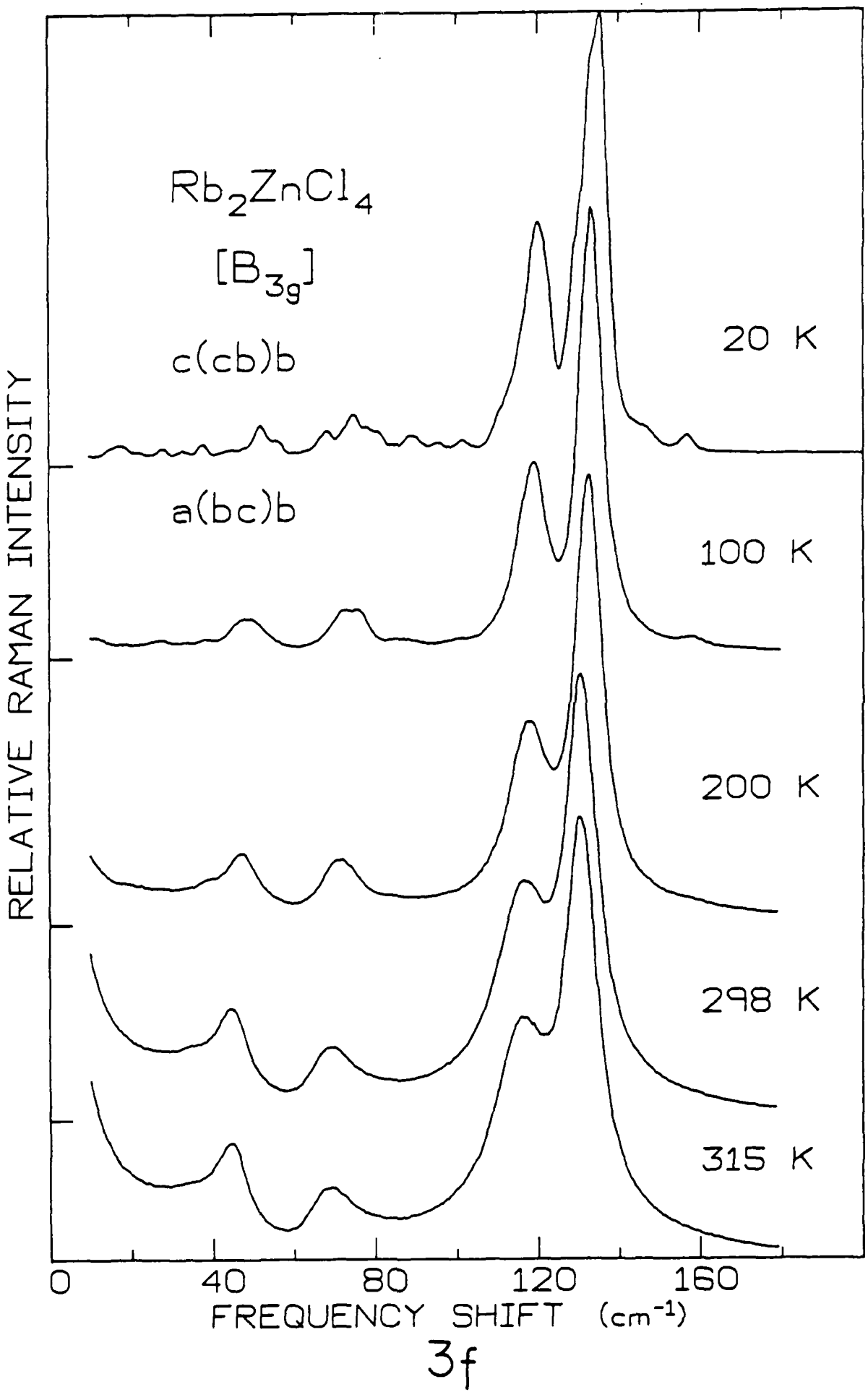
Rb_2ZnCl_4
$[B_{3g}]$
c(cb)b
a(bc)b
20 K
100 K
200 K
298 K
315 K
RELATIVE RAMAN INTENSITY
0
40
80
120
160
FREQUENCY SHIFT (cm^{-1})

3f

portion.

The internal-mode Raman spectra of Rb_2ZnCl_4 appear as a consequence of the internal vibrations of the sublattice of the chlorozincate ions, $ZnCl_4^{2-}$. The symmetry of these internal modes arises from the coupling between the free radical symmetry and the site symmetry. For Rb_2ZnCl_4 in phase II (paraelectric phase), the unit cell symmetry is Pnam (D_{2h}^{16}) and the site symmetry of the $ZnCl_4^{2-}$ ions is C_s. The free chlorozincate ion is tetrahedral and thus belongs to the T_d symmetry and has normal modes of $A_1(\nu_1)$, $E(\nu_2)$, and $2F(\nu_3, \nu_4)$. The frequencies of those normal modes are 275 cm^{-1}, 79 cm^{-1}, 306 cm^{-1}, and 104 cm^{-1} for ν_1, ν_2, ν_3, and ν_4, respectively (23), where ν_2 and ν_4 are the bending modes and ν_1 and ν_3 are the stretching modes.

The correlation diagram for the internal modes, derived from the group theoretical analysis of the assumed β-K_2SO_4 structure of Rb_2ZnCl_4, is shown in Table VI.

TABLE VI

Correlation Table for Internal Modes of Rb_2ZnCl_4 in Paraelectric Phase (II) --D^{16}_{2h}

Free Ion Frequency	Free Ion Symmetry T_d	Site Symmetry C_s	Crystal Symmetry D^{16}_{2h}		Frequency
$4\ \upsilon_1$ (275 cm^{-1})	A_1	A'	A_g	(aa bb cc)	
				(xx yy zz)	$\upsilon_1\upsilon'_2\upsilon'_3\upsilon''_3\upsilon'_4\upsilon''_4$
			B_{1g}	(xy ab)	$\upsilon_1\upsilon'_2\upsilon'_3\upsilon''_3\upsilon'_4\upsilon''_4$
			B_{2u}	(y)	$\upsilon_1\upsilon'_2\upsilon'_3\upsilon''_3\upsilon'_4\upsilon''_4$
$4\ \upsilon_2$ (79 cm^{-1})	E		B_{3u}	(x)	$\upsilon_1\upsilon'_2\upsilon''_3\upsilon''_3\upsilon'_4\upsilon''_4$
$4\upsilon_3\upsilon_4$ (306, 104 cm^{-1})	F_2	A''	A_u		$\upsilon_2\upsilon_3\upsilon_4$
			B_{1u}	(z)	$\upsilon_2\upsilon_3\upsilon_4$
			B_{2g}	(xz ac)	$\upsilon_2\upsilon_3\upsilon_4$
			B_{3g}	(yz bc)	$\upsilon_2\upsilon_3\upsilon_4$

This implies that Rb_2ZnCl_4 has 36 independent "internal modes" from the chlorozincate radicals $ZnCl_4^{2-}$. These optical phonon modes can be classified into the following irreducible representations:

$$6A_g + 6B_{1g} + 3B_{2g} + 3B_{3g} + 3A_u + 6B_{1u} + 6B_{2u} + 3B_{3u} \quad .....(1)$$

where the 18 modes belonging to the gerade representations (g) are all Raman-active, only, and the ungerade modes (u) modes are infrared-active or silent, only. These 18 Raman-active modes fall in two spectral regions. Lines derived from the bending modes, ν_2 and ν_4, lie in the 100-160 cm^{-1} range and lines derived from the stretching modes, ν_1 and ν_3, lie in the 260-330 cm^{-1} range. The absence of any Raman lines at frequencies higher than 310 cm^{-1} suggests that the ionic bonds in the $ZnCl_4^{2-}$ radicals are weak compared to those in the SeO_4^{2-} radicals in K_2SeO_4 whose spectrum extends to nearly 1000 cm^{-1}.

The following figures 4a)-4f) show the Raman spectra in the 240-340 cm^{-1} region for a temperature range from 20 K up to 315 K for all the scattering polarizations.

In the analysis of Raman spectra, the experimenter must be wary of "polarization leakage" effects. The term, polarization leakage, describes a situation in which a strong line from one polarization pair associated with a particular factor group appears in the spectrum of another polarization pair. In our case, the 295 cm^{-1} line in the A_g spectrum has the highest intensity of all of the measured lines. It also appears in the B_{1g}, B_{2g}, and B_{3g} spectra as we have postulated it should, but its intensity relative to the neighboring lines in the B_{2g} and B_{3g} spectra was observed to vary with the directions of the

Fig. 4 Raman spectra of the internal modes (240-340 cm^{-1}) of Rb_2ZnCl_4 at 20 K, 100 200 K, room, and 315 K for

a) A_g modes: b(aa)c

b) A_g modes: a(bb)c

c) A_g modes: a(cc)b

d) B_{1g} mode:

e) B_{2g} mode:

f) B_{3g} mode:

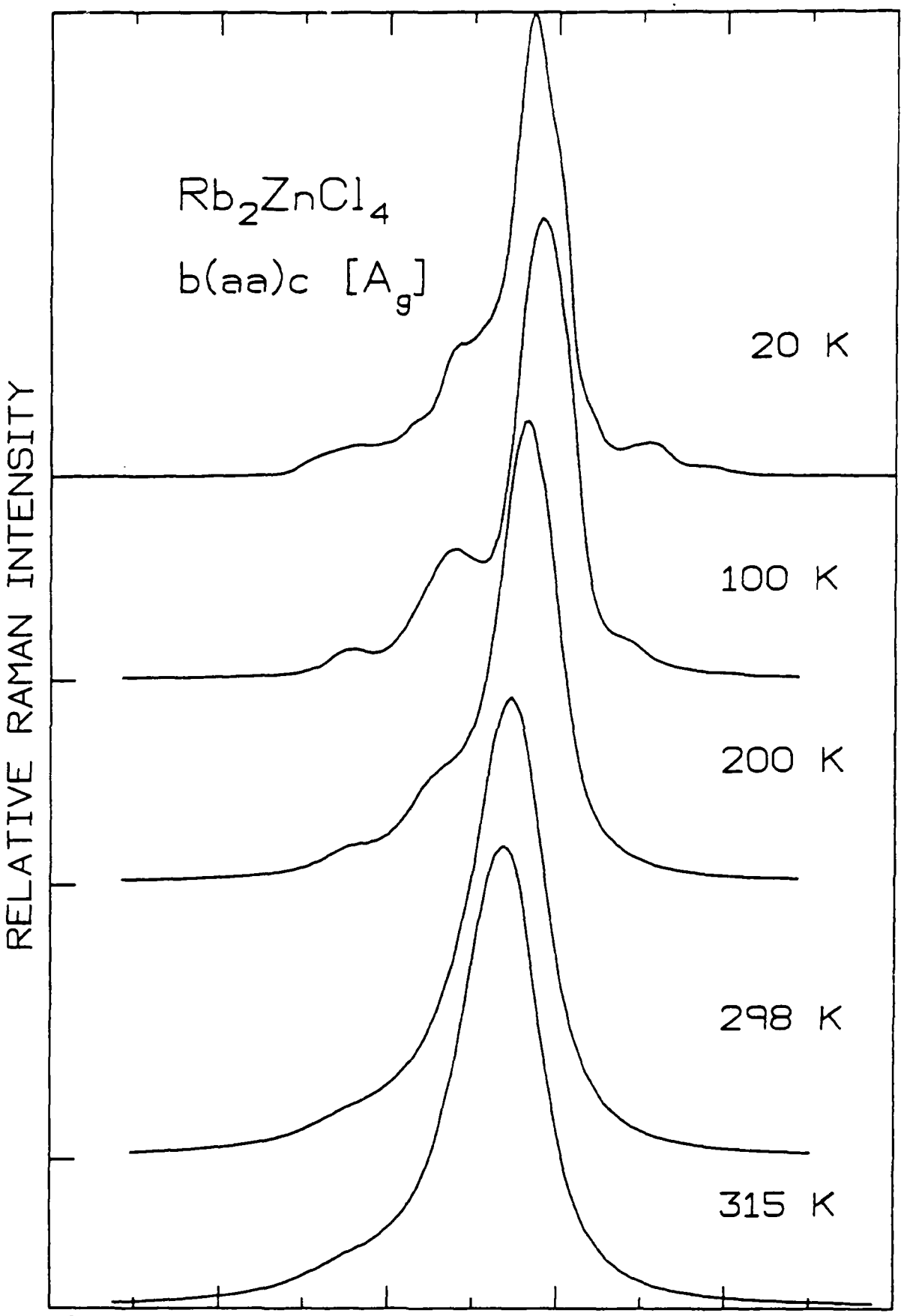
Rb_2ZnCl_4
b(aa)c [A_g]
20 K
100 K
200 K
298 K
315 K
RELATIVE RAMAN INTENSITY
240
260
280
300
320
FREQUENCY SHIFT (cm^{-1})

4a

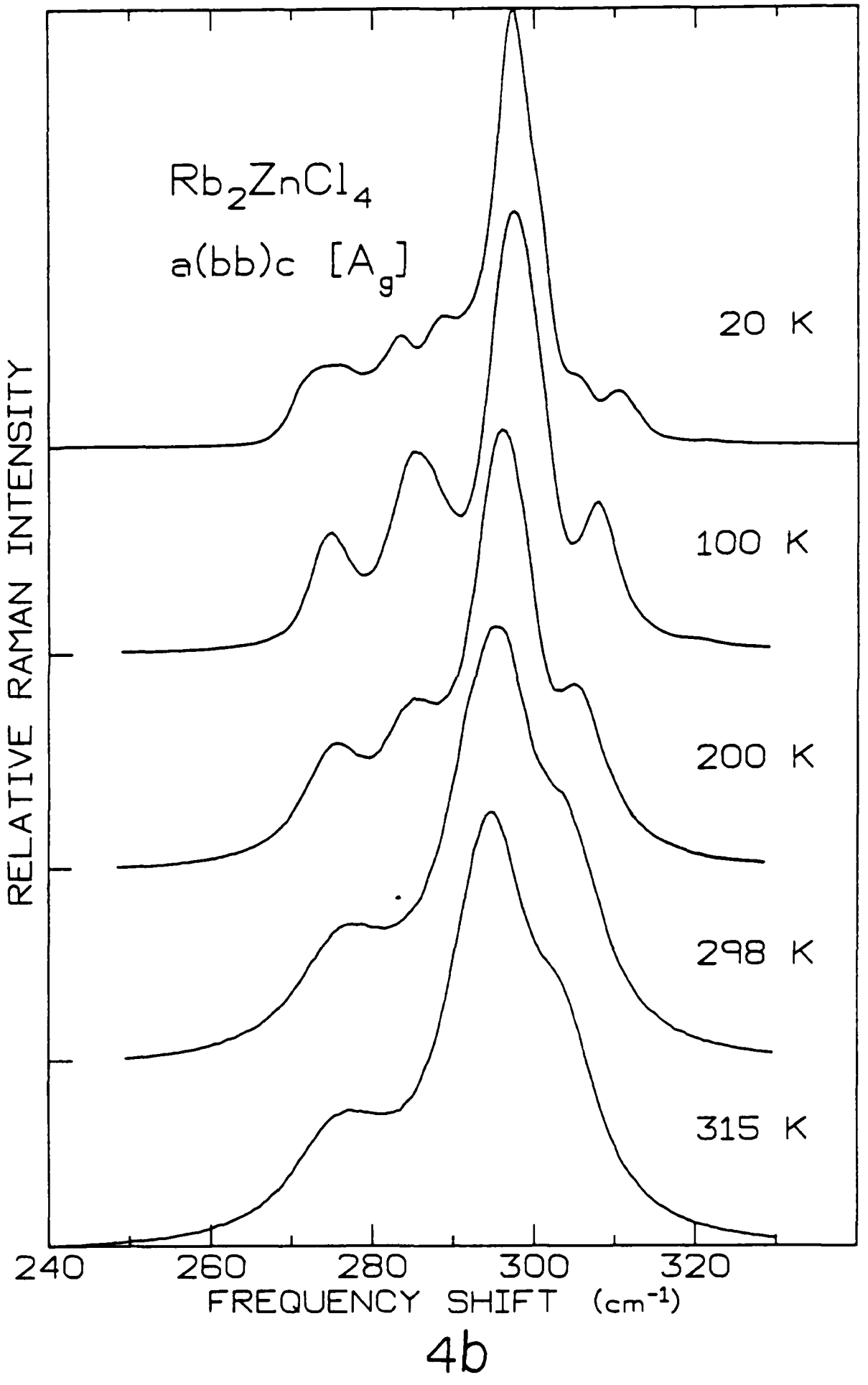
Rb_2ZnCl_4
a(bb)c [A_g]
20 K
100 K
200 K
298 K
315 K
RELATIVE RAMAN INTENSITY
240
260
280
300
320
FREQUENCY SHIFT (cm^{-1})

4b

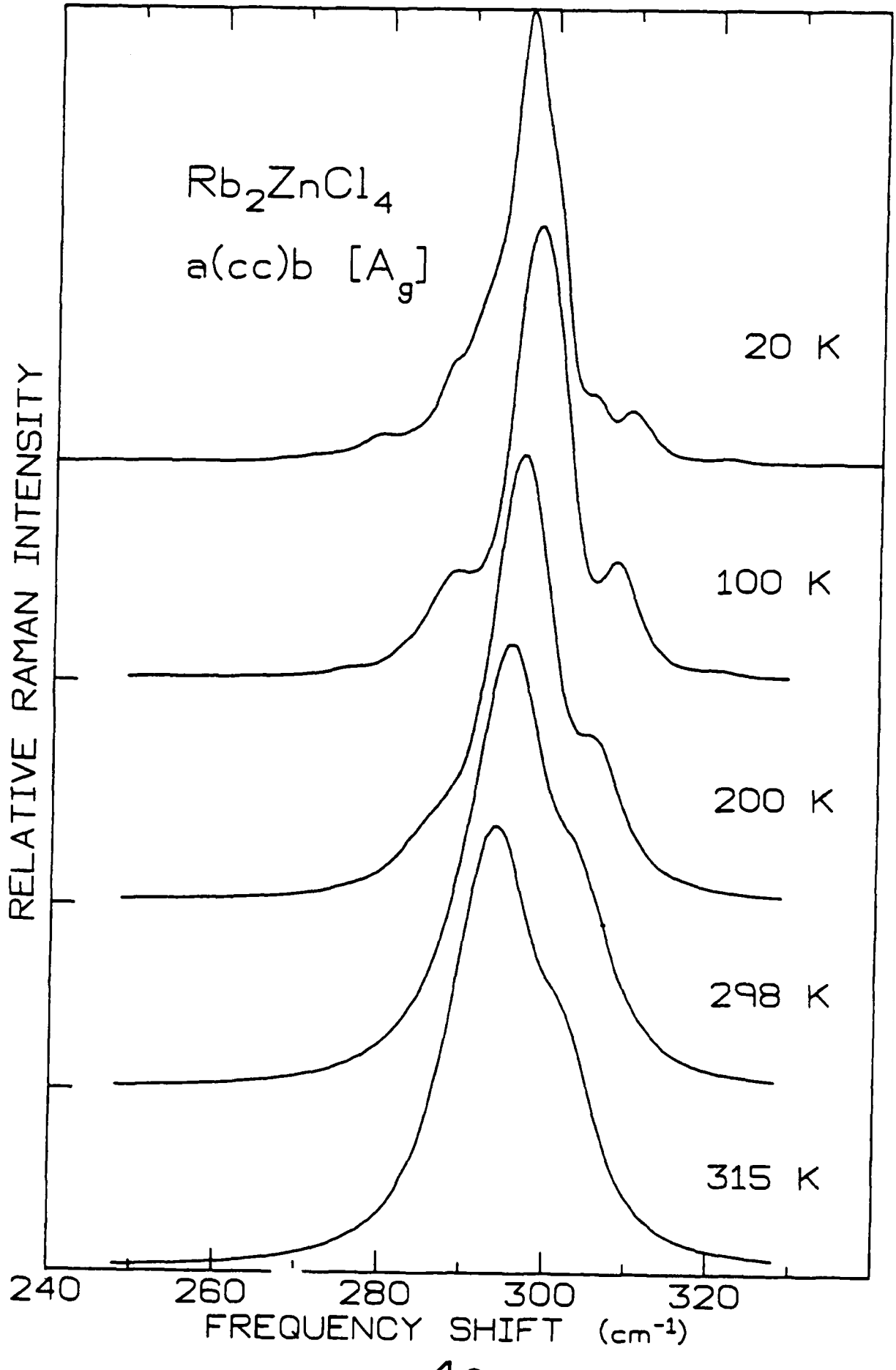
Rb_2ZnCl_4
a(cc)b [A_g]
20 K
100 K
200 K
298 K
315 K
RELATIVE RAMAN INTENSITY
240
260
280
300
320
FREQUENCY SHIFT (cm^{-1})

4c

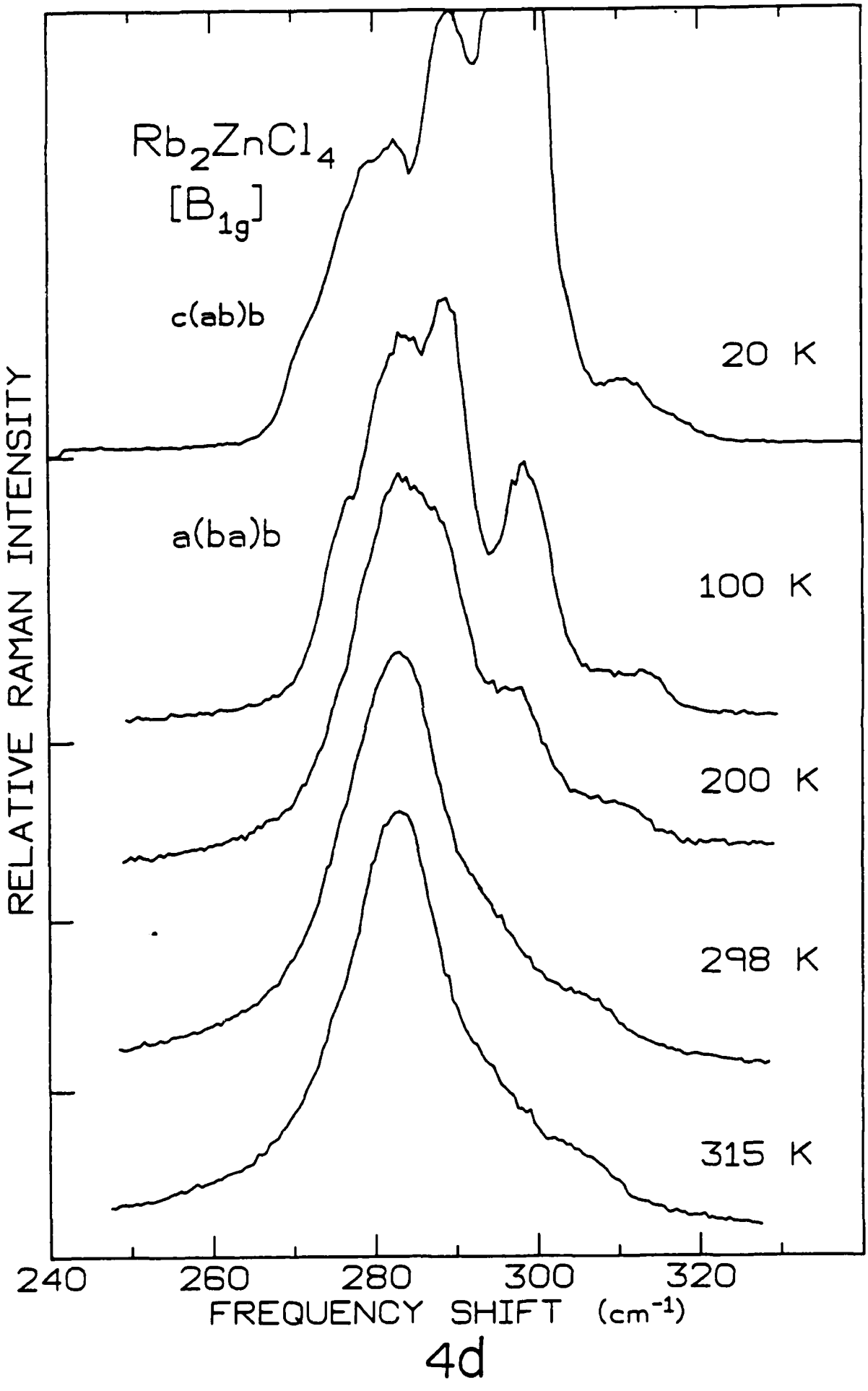
Rb_2ZnCl_4
$[B_{1g}]$
c(ab)b
a(ba)b
20 K
100 K
200 K
298 K
315 K
RELATIVE RAMAN INTENSITY
240
260
280
300
320
FREQUENCY SHIFT (cm^{-1})

4d

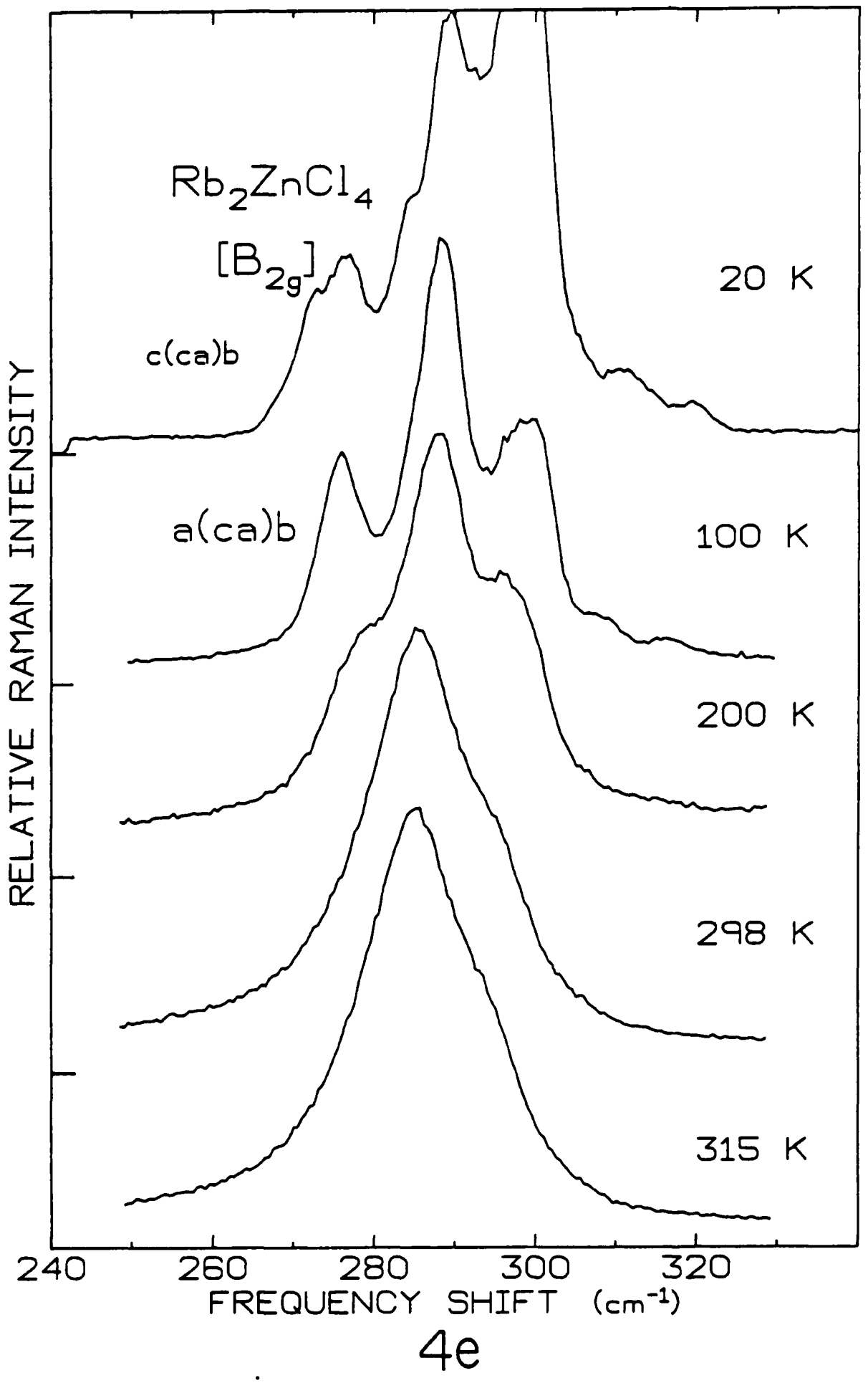
Rb_2ZnCl_4
$[B_{2g}]$
c(ca)b
a(ca)b
20 K
100 K
200 K
298 K
315 K
RELATIVE RAMAN INTENSITY
240
260
280
300
320
FREQUENCY SHIFT (cm^{-1})

4e

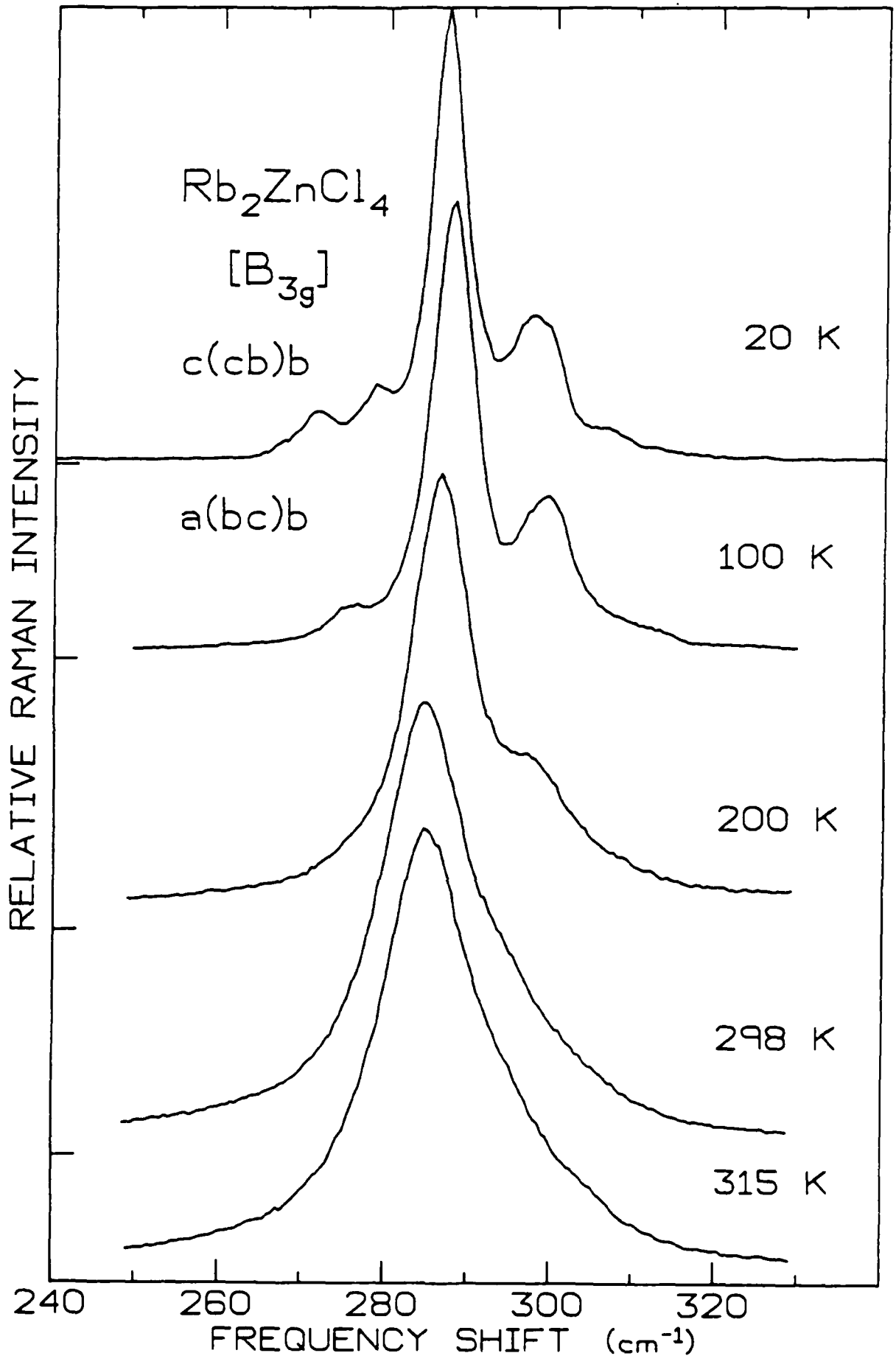
Rb_2ZnCl_4
$[B_{3g}]$
c(cb)b
a(bc)b
20 K
100 K
200 K
298 K
315 K
RELATIVE RAMAN INTENSITY
240
260
280
300
320
FREQUENCY SHIFT (cm^{-1})

4f

incident and scattered light which should not be the case. Since it would normally be forbidden in the B_{2g} and B_{3g} spectra by the Pnam selection rules, we expect it to be weak relative to the neighboring lines, yet in b(--)c spectra, it was the strongest, indicating a leakage contribution. We therefore chose the B_{2g} and B_{3g} configurations with the smallest contribution from the 295 cm-1 line to display in Fig. 4. At 20 K, however, the measurements were made in only the c(--)b configuration. Consequently, for the 20 K measurement we show the 295 cm^{-1} peak off-scale in Fig. 4 so the other features of the spectrum can be seen more clearly.

IV. DATA ANALYSIS

A. Correction of spectra for finite slit width

In the analysis of the band shapes of the Raman lines, it is necessary to take into account the distortion caused by the dispersion associated with the finite widths of the slits. This spectral distortion can introduce significant errors in the analysis of these Raman spectra because the line widths and the splitting of the lines often are of the same order as the slit width. In such cases, the observed line shape can be determined from the true line shape by a convolution with the dispersion function of the slits. If the lineshape function (a Lorentzian in this case) is $L(\nu)$ and the slit transmission function is $G(\nu' - \nu)$ with the monochromator set at ν', then the transmitted spectrum is given by a convolution of these two functions, i.e.,

$$S(\nu') = \int L(\nu)\, G(\nu' - \nu)\, d\nu. \qquad \ldots\ldots(2)$$

Thus, if the slit function and lineshape functions are known, the true lineshape can be found by fitting their convolution to the experimental Raman line. This is particularly important in this case because many of the lines in the Rb_2ZnCl_4 spectra overlap and thus distortions caused by the slit dispersion can easily lead to false conclusions. For example, the four highest frequencies in the Rb_2ZnCl_4 spectrum, whose study in detail form a separate section of this report, fall in only a 60 cm^{-1} range, 260-320 cm^{-1}, with full widths at half maximum (FWHM) of about 20 cm^{-1}, and thus overlap

significantly. In all of the Raman data that are reported here, the slit width correction, described below, was made.

For a modern monochromator, the slit function is close to a Gaussian, at least for small slit widths. On the other hand, the slit function will be more or less triangular for larger slit widths. The slit function used here is obtained by assuming uniform monochromatic illumination of the first slit which produces a rectangular intensity pattern scanning the second slit. Thus, the output from the second slit is a convolution of the two rectangle slit functions, which gives a triangle function incident on the third slit. The output of the third slit is then a second convolution of the triangle function with the slit rectangle function. [redacted] This slit function was suggested by Galliardt (24). It is given by $H_3(u_3,\Delta)$, in our notation, as described below:

$$H_3(u_3,\Delta) = \begin{cases} 0 & 3\Delta \leq u_3 \\ \dfrac{N(u_3 - 3\Delta)^2}{2} & \Delta < u_3 < 3\Delta \\ N(3\Delta^2 - u_3^2) & -\Delta \leq u_3 \leq \Delta \\ \dfrac{N(u_3 + 3\Delta)^2}{2} & -3\Delta < u_3 < -\Delta \\ 0 & u_3 \leq -3\Delta \ . \end{cases} \qquad \ldots\ldots(3)$$

where Δ is a slit width in frequency units obtained from fitting to the laser line, u_3 is the Raman frequency shift, $\omega_3-\omega$, and N is a normalization factor.

The true line-shapes of the Raman spectra can often be approximated by Lorentzians. Therefore, the observed profile will be the convolution of the slit function, $H_3(u_3,\Delta)$, with a Lorentzian. Consider an incoming Lorentzian, $L(\omega)$, of height, S, and width, γ, centered at the frequency, ω_o, which is given by

$$L(\omega) = \frac{S}{1 + \left(\dfrac{2(\omega - \omega_o)}{\gamma}\right)^2} \qquad \ldots\ldots(4)$$

From the convolution of this Lorentzian with the calculated slit function, we obtain the observed intensity distribution as

$$I(\omega_3) = \int_{-\infty}^{\infty} d\omega \; H_3(\omega_3-\omega,\Delta) \; L(\omega). \qquad \ldots\ldots(5)$$

This leads to the following calculated Raman line shape,

$$I(\omega_3) = B_1 + P_1 + P_2 + P_3 + \ldots \qquad \ldots\ldots(6)$$

where B_1 is a constant background, and P_1, P_2, P_3,... correspond to each observed peak in the Raman spectrum and is equal to

$$P_i = B_2(\omega - \omega_{oi}) + \frac{S_i}{16}\frac{\gamma_i^3}{3\Delta^2}\left[Q(Z_i + 3R_i] - Q(Z_i - 3R_i) - 3Q(Z_i + R_i] + 3Q(Z_i - R_i)\right] \qquad \ldots.(7)$$

where B_2 is a linear background, i = 1, 2, 3, ...,

$$Q(x) = (x^2 - 1)\tan^{-1}x - x \log (x^2 - 1), \qquad \ldots\ldots(8)$$

$$Z_i = \frac{2}{\gamma_i}(\omega - \omega_{oi}), \qquad \ldots\ldots(9)$$

and $$R_i = \frac{2\Delta}{\gamma_i}. \qquad \ldots\ldots(10)$$

S is the peak height of the convolved function, Δ is the slit width, ω_o is the undamped mode frquency, ω is the frequency shift from the laser line, and $\omega_3 = \omega - \omega_o$.

B. Method for Data Analysis

The procedure used for each spectrum was as follows: First, the spectrometer function given by Eq.(4), along with a least-square fitting routine (LMCHOL) (25), was used to obtain the best fit to the laser line. The frequency shift at the peak of the laser line should be zero, but due to monochromator misalignment from room temperature fluctuations, the calibration of the spectrometer may shift by 1 or

2 cm^{-1} on a day-to-day basis. Thus, it is necessary to "fit the laser line" to establish the "true" zero frequency shift, since our Raman frequency shifts are recorded as the monochromator dial reading and must be corrected for this error. Also, the value of the slit parameter (Δ) which gave the best-fit to the laser line was then used for further calculations. These results, along with the measured Raman data, were then fed to a second computer program which fitted the observed lines to the Lorentzian line shape convoluted with the spectrometer transfer function (Eq.(7)). The results of these calculations were the intensities, linewidths, and frequencies of the observed Raman peaks.

In our previous data analysis of the higher frequency internal modes (240-340 cm^{-1}) of Rb_2ZnCl_4 for the A_{1g}(bb) spectrum between phases III and II, several problems arose in trying to fit this function to the regular experimental Raman data. First, there can be a significant interfering background arising from the width of the unshifted laser line scattering (usually defect-induced) and possibly, also, from surface roughness and optical misalignment. A second problem arises from weak peaks which are nearly or completely unobservable from overlap with adjacent peaks which prevent accurate fitting to a single line. We have been able to resolve both of these problems by fitting to lineshape derivatives. It is well-known from the work of Yacoby and colleagues (26) that obscured Raman peaks can be visualized by temperature or wavelength modulation spectroscopy. However, lineshape-fitting to the derivative spectra has not been reported previously (to our knowledge) for Raman spectra. The advantages are two-fold: (1) the constant background terms are

eliminated, and (2) the observed weak features in the normal spectrum can often be visualized in the derivative spectrum and even when not visible, can influence the fit by inclusion in the spectrum. Our resulting fits are highly reliable in this higher frequency region. Nevertheless, this derivative process seems not to work as well for the fit to the external mode region, 10-180 cm^{-1}. This can be explained as arising from more significant background influence since this frequency range is closer to the tail of the "unshiftd" laser line scattering. If these background terms are ignored, good agreement between the calculated curve and the data cannot be obtained. Therefore, a linearly frequency-dependent background was introduced and the lineshape function itself rather than the derivative was used to fit to the measured Raman spectra. To ensure the accuracy of the former derivative fit to the higher internal mode frequencies, we recalculated the fit to those spectra with this lineshape function including the linear background terms. The results show no difference, so the frequency-dependent background term is not needed and only a small, constant background needs to be retained for these higher frequency lines.

The following figures 5a)-5h) show the quality of our fitting process for best and worst-case examples at low temperature (100 K) and at the higher temperatures. The vertical lines in the figures indicate the calculated peak frequencies and their heights represent their calculated integrated intensity. The examples of fitted spectra were chosen to be at these temperatures since at higher temperature, most of the peaks are broad and strongly overlapped to the extent that some peaks are completely buried. To fit to those high temperature

Fig. 5 Quality of the fitting process: best and worst-case examples.

a) best fit, 100 K: 0-200 cm^{-1},

b) 240-340 cm^{-1};

c) worst fit, 100 K: 0-200 cm^{-1},

d) 240-340 cm^{-1}

e) best fit, 298 K: 0-200 cm^{-1},

f) 240-340 cm^{-1};

g) worst fit, 395 K: 0-200 cm^{-1},

h) 240-320 cm^{-1}.

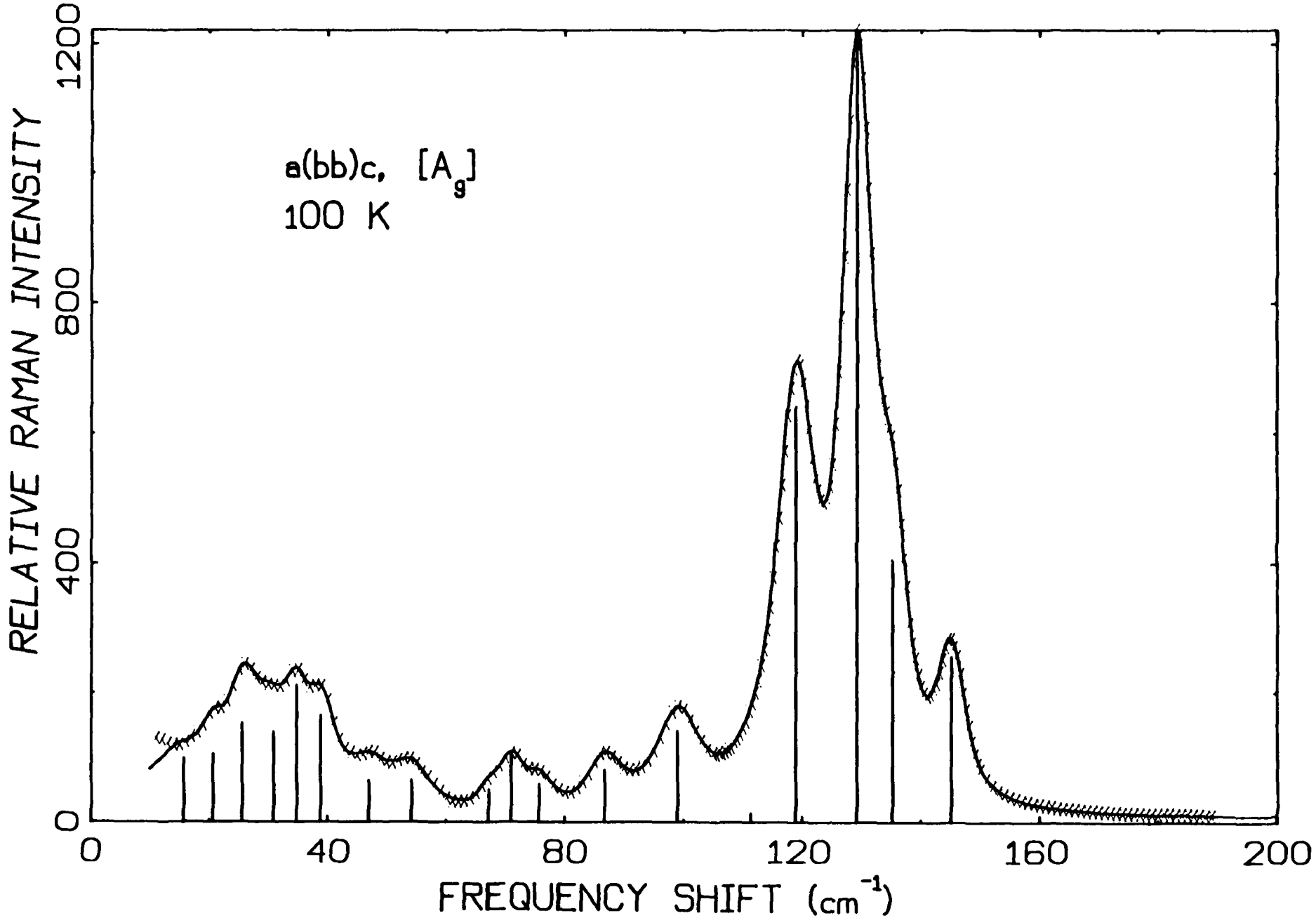
a(bb)c, [A$_g$]
100 K
RELATIVE RAMAN INTENSITY
0
400
800
1200
0
40
80
120
160
200
FREQUENCY SHIFT (cm^{-1})

5a

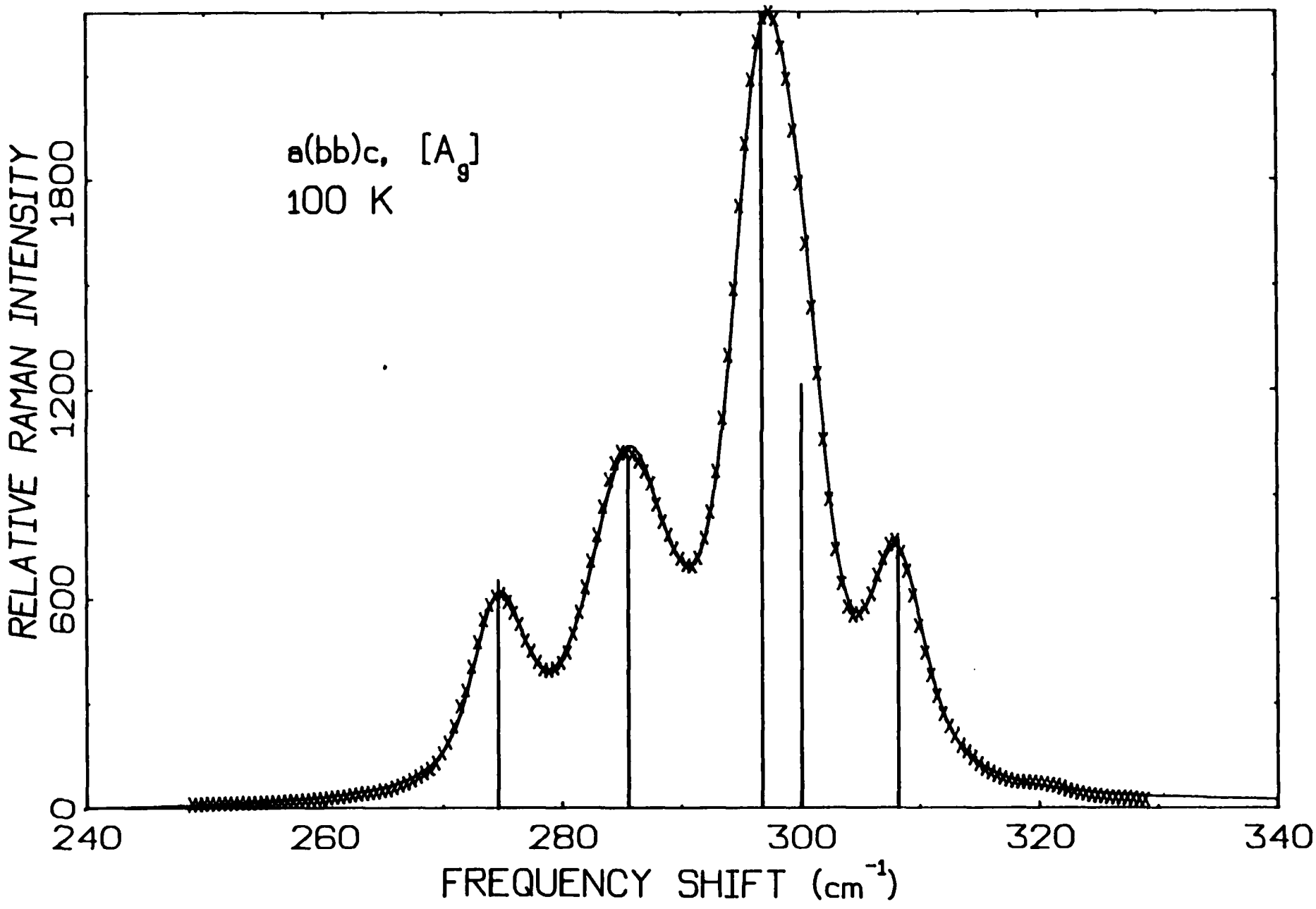
a(bb)c, [A$_g$]
100 K
RELATIVE RAMAN INTENSITY
0
600
1200
1800
240
260
280
300
320
340
FREQUENCY SHIFT (cm^{-1})

5b

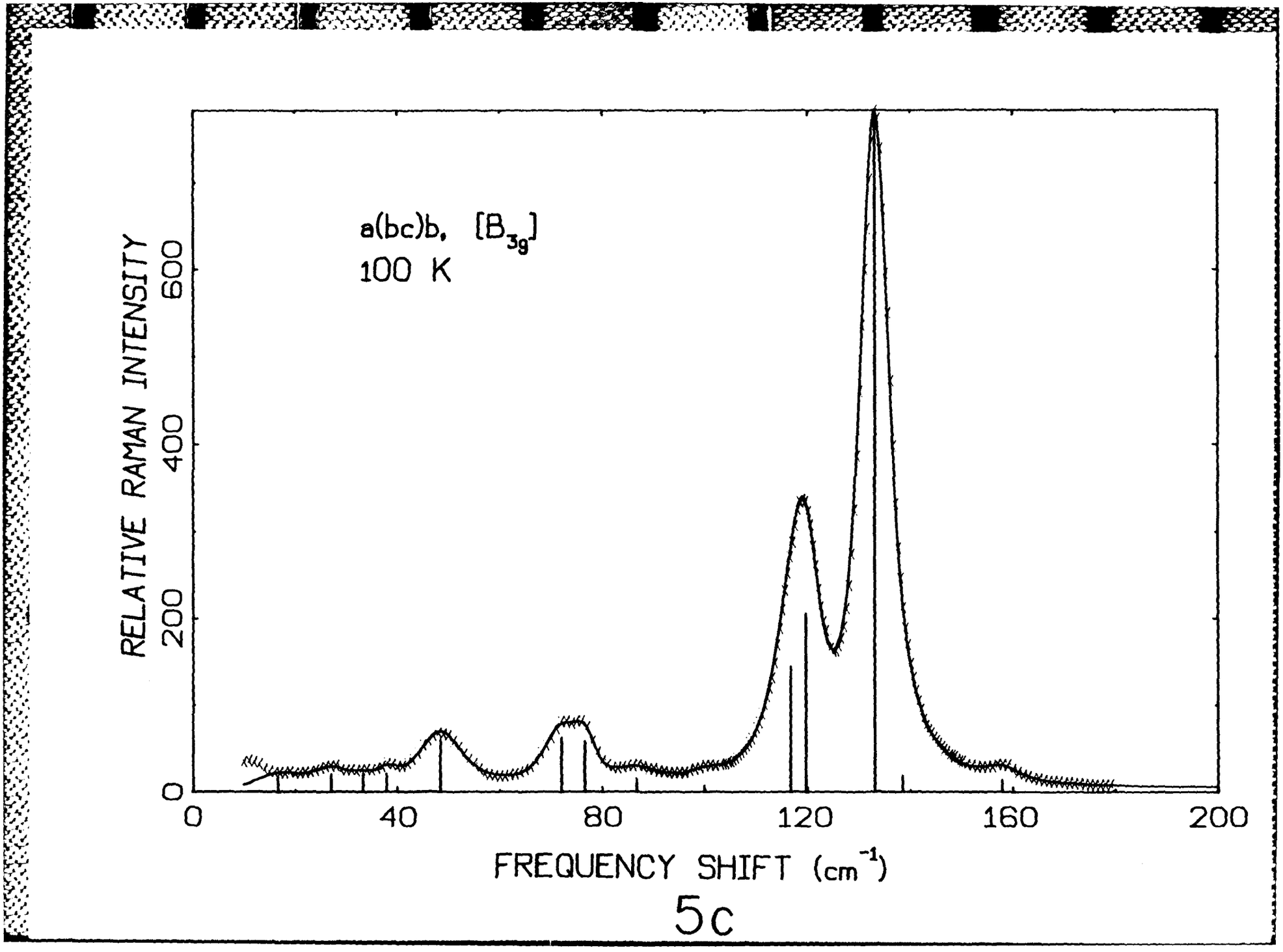
a(bc)b, [B3g]
100 K
RELATIVE RAMAN INTENSITY
0
200
400
600
0
40
80
120
160
200
FREQUENCY SHIFT (cm-1)

5c

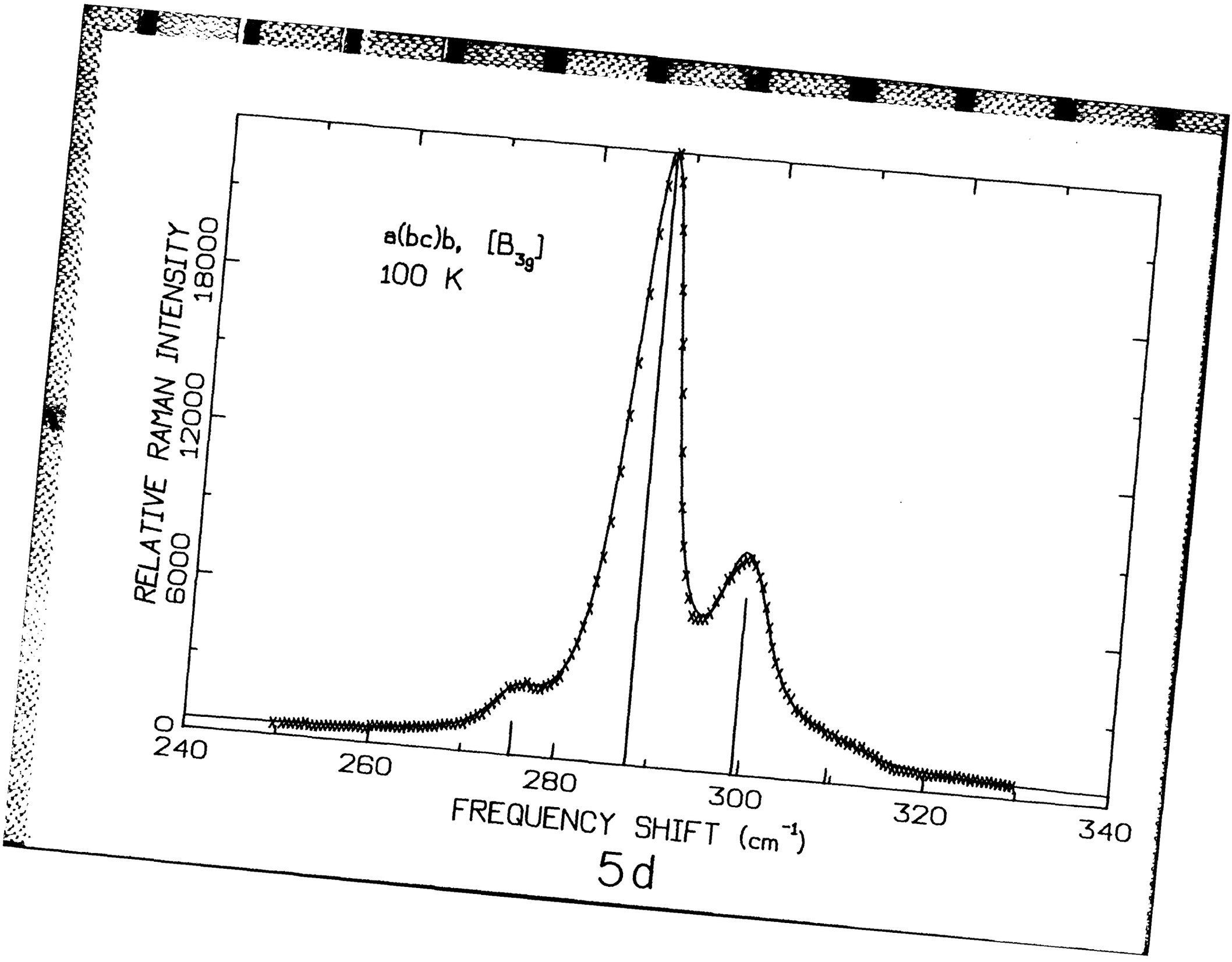
a(bc)b, [B3g]
100 K
RELATIVE RAMAN INTENSITY
0
6000
12000
18000
240
260
280
300
320
340
FREQUENCY SHIFT (cm-1)

5d

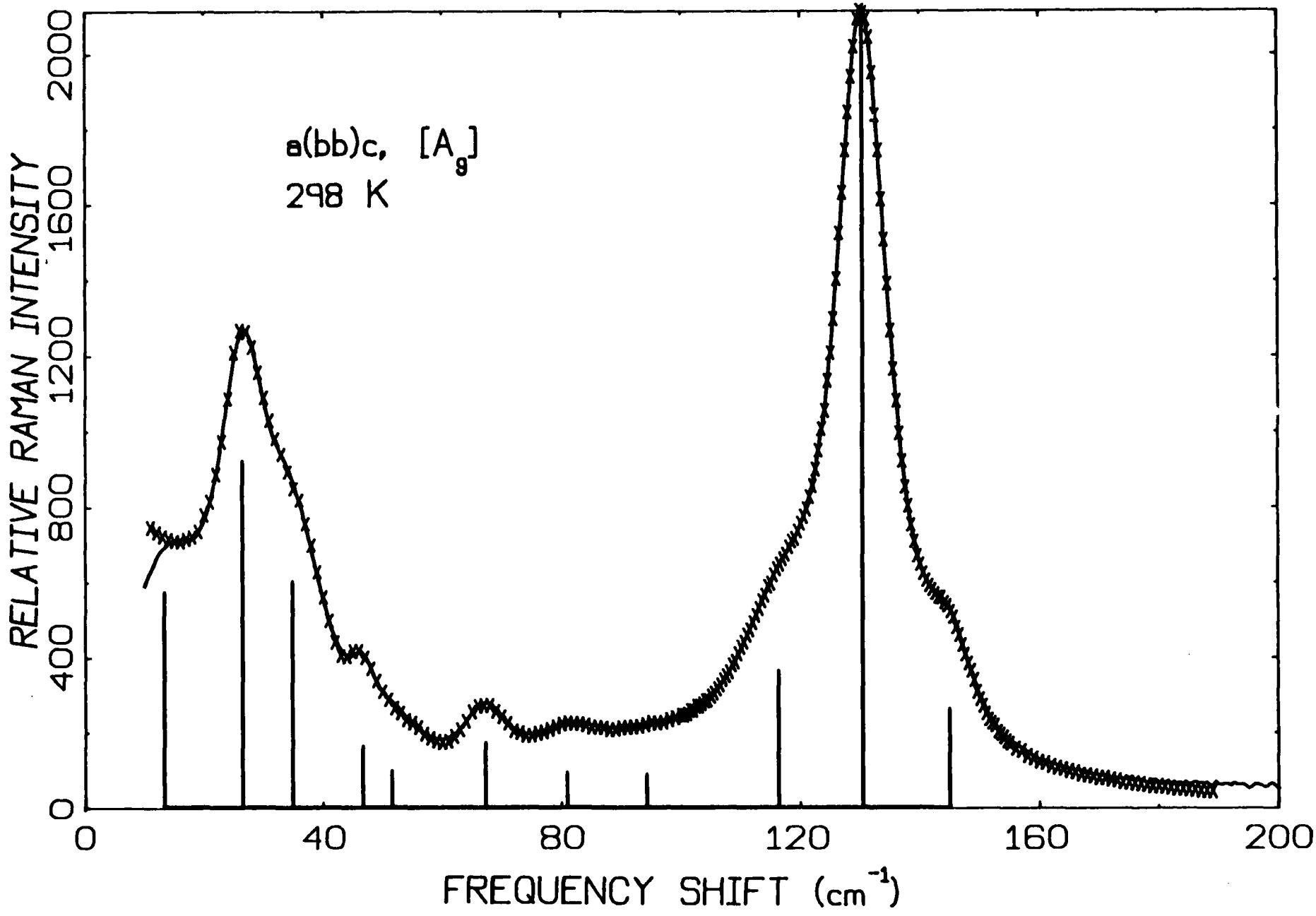
a(bb)c, [A$_g$]
298 K
RELATIVE RAMAN INTENSITY
0
400
800
1200
1600
2000
0
40
80
120
160
200
FREQUENCY SHIFT (cm^{-1})

5e

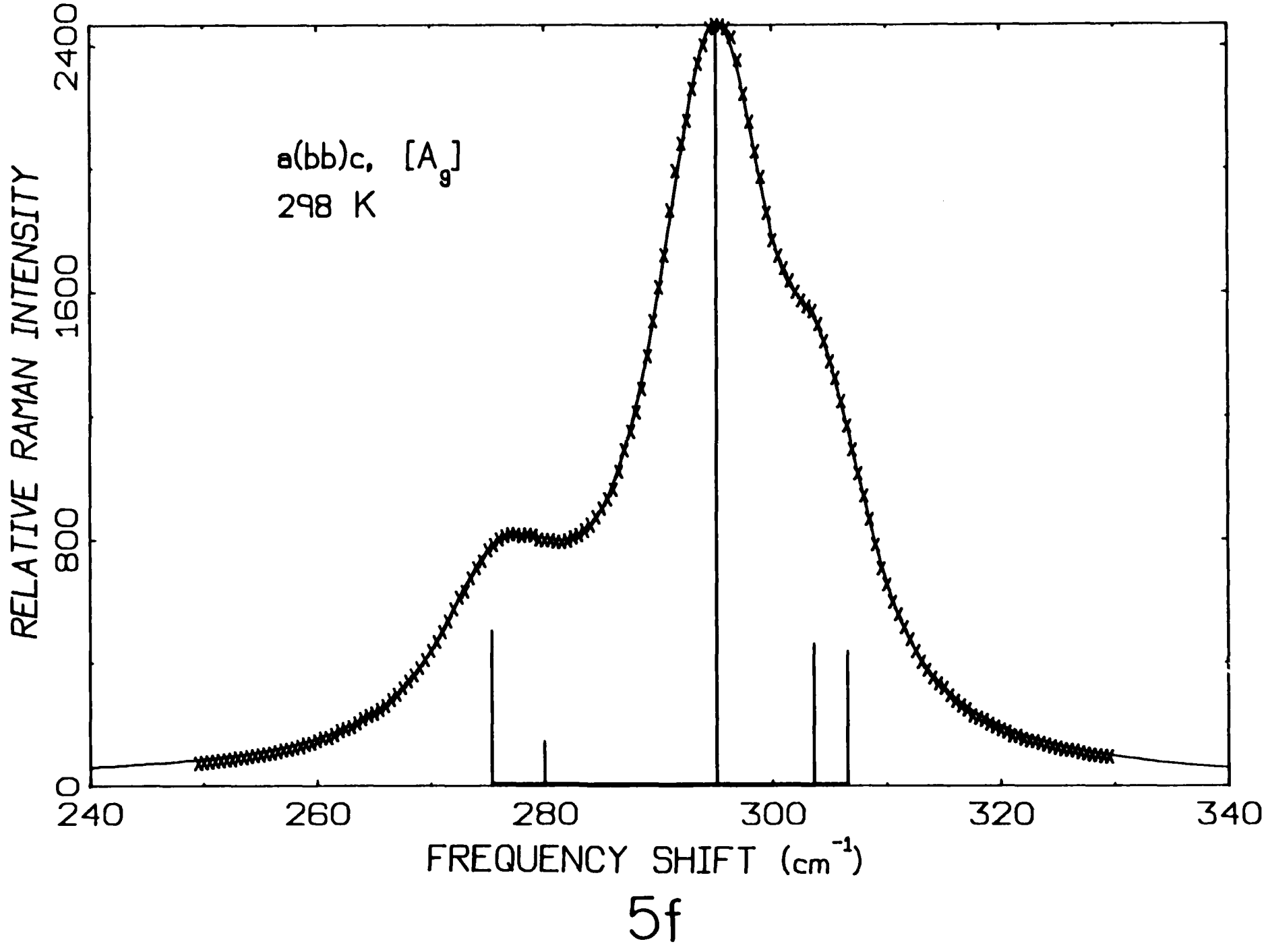
a(bb)c, [A$_g$]
298 K
RELATIVE RAMAN INTENSITY
0
800
1600
2400
240
260
280
300
320
340
FREQUENCY SHIFT (cm^{-1})

5f

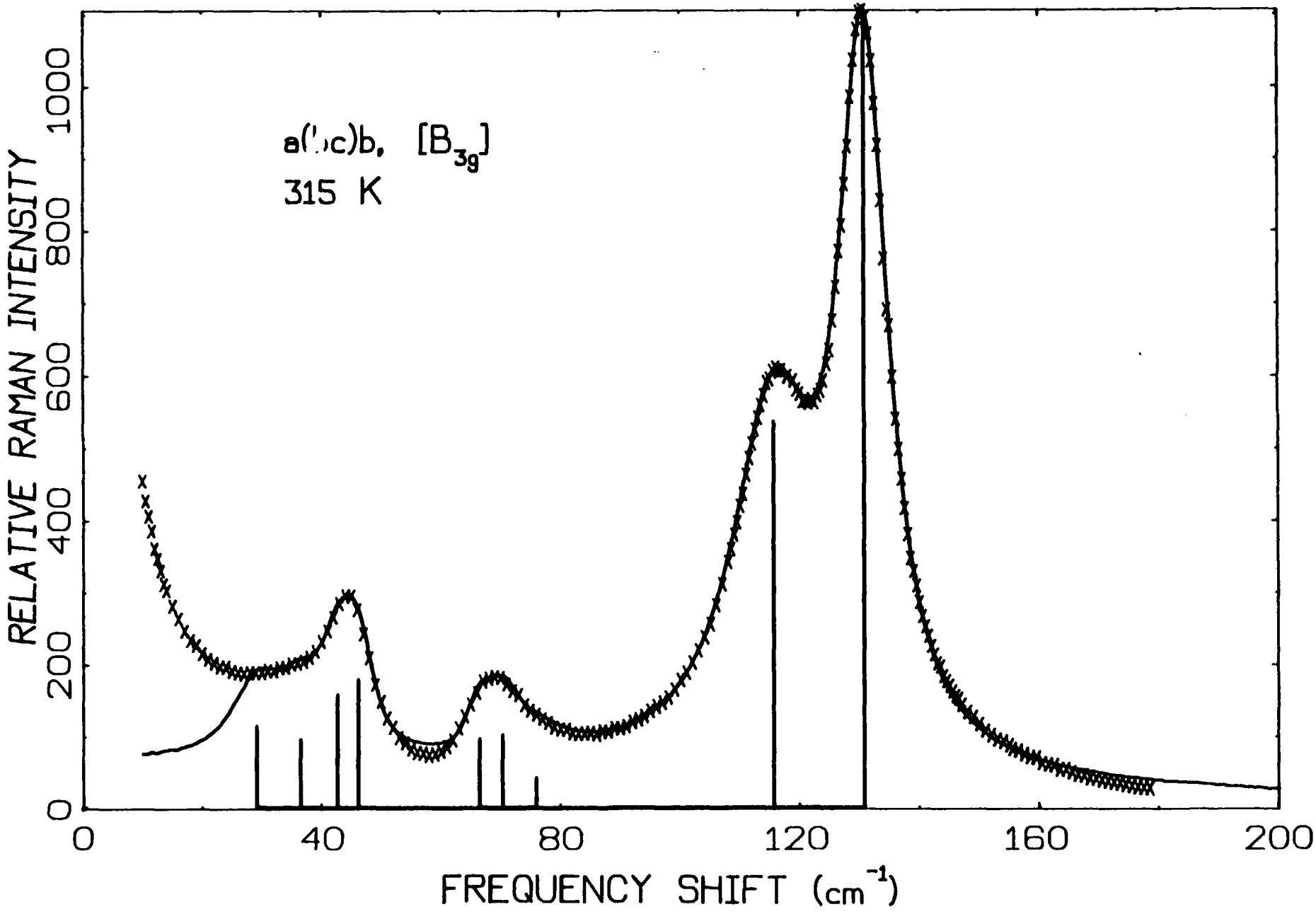
a(b,c)b, [B3g]
315 K
RELATIVE RAMAN INTENSITY
0
200
400
600
800
1000
0
40
80
120
160
200
FREQUENCY SHIFT (cm-1)

5a

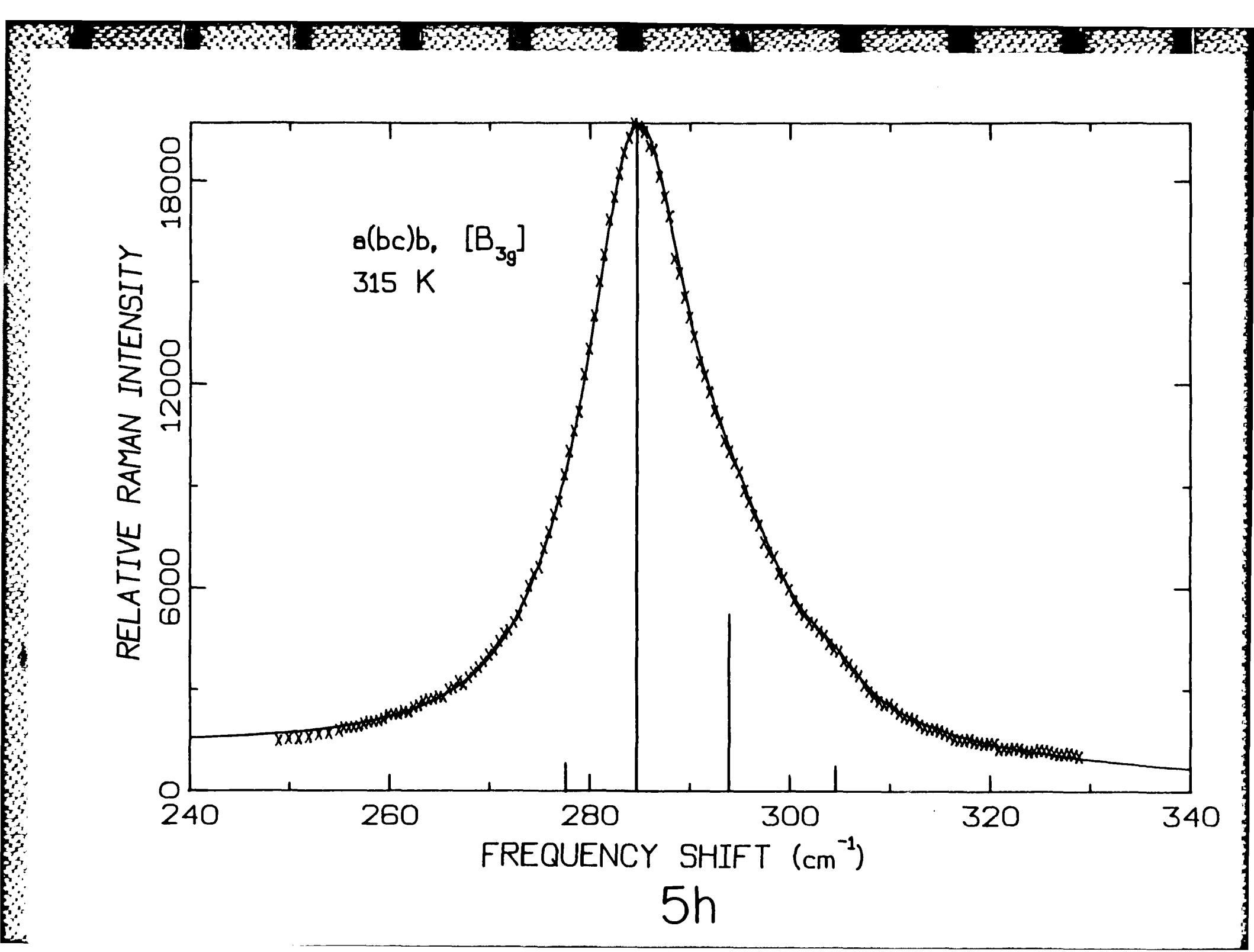
a(bc)b, [B3g]
315 K
RELATIVE RAMAN INTENSITY
0
6000
12000
18000
240
260
280
300
320
340
FREQUENCY SHIFT (cm-1)

5h

spectra, we first calculated the fit to the low temperature Raman spectrum in which most of the peaks are well separated and used these fit parameters as initial guesses for the high temperature spectrum. The fitting program will reject unnecessary peaks by giving zero or an insignificant value for the intensity or for the damping function (FWHM). For a further check, sometimes the fit was recalculated with very narrow peaks (~2-3 cm^{-1}) combined or eliminated to determine if they are really needed for the fit. The reliability of the fitted spectra could be estimated from the chi-squared value and visual comparisons of the calculated and experimental spectra. Finally, we should point out that we could not fit very weak peaks at the beginning and end of the spectrum, i. e., although seen in the experimental spectra, they were rejected by the fit.

V. Analysis and Comparison with Theory

In the previous analysis of potassium selenate (1), the model proposed that the selection rules that apply to the Pnam structure would still apply to the lattice modes. However, for the internal modes, the four allowed free-ion lines and their satellites, formed from the removal of their degeneracy by the crystal field, would give 9 lines, all of which would be seen in each of the spectra for the four applicable symmetry groups. Since the deviation from Pnam symmetry in the potassium selenate was believed small, the strong lines were taken to be the "allowed" lines given by the selection rules for Pnam, and the weak lines to be the "forbidden lines" brought in by the disorder. (The foregoing statement is to some extent an oversimplification as there were a few confusing intensity reversals that had to be explained.) In particular, examination of the (ac) and (bc) spectra is especially illuminating since only three of the nine lines are "allowed" in those two cases, i.e., line identification is enhanced by identifying systematic weaknesses in the (ac) and (bc) spectra.

In the present work, we have used the same procedure as much as possible and also have compared the Rb_2ZnCl_4 spectra with the K_2SeO_4 results as an additional analytical aid. However, in the case of Rb_2ZnCl_4 the distinction between "weak" and "strong" is either unclear or absent and there is greater line overlap because of the spectral range compression of about a factor of three relative to K_2SeO_4. Line overlap was also a problem in the case of K_2SeO_4 but satisfactory resolution was achieved by cooling to 140 K, still about ten degrees

above its 129 K incommensurate transition. For Rb_2ZnCl_4, however, the incommensurate transition is at 302 K, so to resolve the lines, the sample must be cooled into its incommensurate phase. Thus, the question arose of whether or not lines resolved below 302 K are allowed above that temperature. An answer to that question was sought by studying the temperature dependence of the reasonably well-isolated quartet of lines in the 260-320 cm^{-1} range. These results will be discussed separately in the next section.

In Table VII a)-f), we show the calculated (from the fit) line frequencies for the four temperatures, 110, 200, 300, and 315 K, for each of the six scattering configurations. The splitting of the various lines on cooling is apparent. Shown separately in Table VIII, is a correlation of the lines calculated from theory for the Pnam structure with the measured frequencies at 315 K, for each scattering configuration. For comparison of these two compounds, Rb_2ZnCl_4 and K_2SeO_4, the calculated frequencies from theory for the Pnam structure of K_2SeO_4 and the measured frequencies at 140 K are also given in Table IX. The calculated and experimental spectra are in good correspondence, typically within about five percent. (Some systematic deviations are discussed later.) The experimental lines are from recent, as-yet unpublished measurements that are greatly improved (lower noise and background, higher precision of frequency determination) over those reported previously in reference 1. They are described in Chapter II.

TABLE VII

RAMAN FREQUENCY, INTENSITY, AND DAMPING FUNCTION OF Rb_2ZnCl_4

AT 100, 200, ROOM, AND 315 K FOR

a) A_g MODE (aa)

b) A_g MODE (bb)

c) A_g MODE (cc)

d) B_{1g} MODE (ab)

e) B_{2g} MODE (ac)

f) B_{3g} MODE (bc)

TABLE VII a)

*** RAMAN Spectra of b(aa)c [A_g] ***

100K			200K			ROOM			315K		
17.93	11164.73	12.01	12.79	10926.97	18.16	0.00	0.00	0.00	26.77	3518.57	4.24
25.46	5964.56	2.42	21.47	4324.97	6.34	28.02	16359.66	10.81	28.43	31455.18	26.59
35.40	17852.35	3.60	32.23	15842.75	5.59	0.00	0.00	0.00	0.00	0.00	0.00
39.78	14826.93	0.85	39.21	15678.52	6.06	36.69	3788.37	8.19	0.00	0.00	0.00
45.29	47784.68	4.40	44.63	56694.12	7.05	44.15	51503.95	6.33	43.53	50961.07	5.64
53.01	28186.90	7.22	53.31	21561.83	13.33	54.05	20308.33	13.18	53.86	29795.98	11.87
64.42	17180.86	4.92	61.30	13875.17	8.65	56.60	4638.46	7.27	0.00	0.00	0.00
74.81	12334.21	11.95	71.46	9882.93	15.22	77.65	8423.95	32.29	78.91	15384.18	30.50
86.90	4674.02	6.01	83.64	7883.61	13.33	0.00	0.00	0.00	0.00	0.00	0.00
96.91	8097.14	10.75	93.73	8288.68	14.17	0.00	0.00	0.00	0.00	0.00	0.00
113.36	12481.87	6.16	111.60	19181.10	13.21	109.84	8692.61	11.96	109.08	10536.28	14.22
120.56	21103.40	8.77	119.84	9755.52	10.43	117.07	4150.50	10.00	119.30	12180.76	17.44
129.79	11896.56	5.29	128.22	9051.07	7.19	130.00	18164.49	12.57	129.70	12635.16	7.04
135.00	3276.72	3.00	132.48	6988.16	7.67	0.00	0.00	0.00	0.00	0.00	0.00
145.66	368408.78	4.16	144.44	398114.36	7.00	144.43	389178.23	9.50	143.95	467590.60	10.02
275.11	25162.76	2.61	275.24	41345.39	6.45	277.49	113022.45	15.03	276.74	144049.93	15.38
285.00	99657.29	5.32	285.45	190632.99	8.05	288.74	270982.24	10.27	288.14	317003.62	10.13
288.24	176072.01	5.57	291.36	96262.56	6.77	293.06	451296.91	6.04	291.80	546812.54	6.02
297.37	761421.06	4.39	295.54	656758.70	5.04	296.13	363060.39	5.39	294.95	284306.20	3.94
300.68	226713.57	2.15	298.59	341679.57	4.24	299.40	79369.32	6.92	297.65	279459.18	7.07
308.79	12923.99	1.20	0.00	0.00	0.00						

TABLE VII b)

*** RAMAN Spectra of a(bb)c [A_g] ***

100K			200K			ROOM			315K		
13.68	14420.21	16.28	13.35	9377.97	9.65	13.23	26471.11	17.71	14.61	16312.12	14.97
20.63	1445.26	1.02	0.00	0.00	0.00	0.00	0.00	0.00	0.00	0.00	0.00
25.54	10122.85	4.23	26.61	57732.80	12.73	26.40	48418.92	8.92	26.05	30276.85	8.49
30.81	19459.67	7.76	0.00	0.00	0.00	0.00	0.00	0.00	0.00	0.00	0.00
34.71	4142.76	0.96	36.46	29936.36	11.83	34.78	63313.55	13.96	34.04	43557.56	13.51
38.79	15110.08	4.17	0.00	0.00	0.00	0.00	0.00	0.00	0.00	0.00	0.00
46.94	12300.44	7.62	47.60	4398.86	2.98	46.62	4365.74	2.58	46.07	3880.87	3.52
54.14	11190.39	6.17	52.45	7984.43	6.51	51.52	10188.07	9.39	51.61	7664.47	10.70
67.19	3093.78	1.86	0.00	0.00	0.00	67.20	19540.83	8.00	67.50	15260.95	9.30
70.99	9189.75	2.61	69.10	20374.22	7.76	0.00	0.00	0.00	0.00	0.00	0.00
75.66	6496.06	3.17	0.00	0.00	0.00	80.82	21150.52	13.86	81.75	20345.38	16.60
86.70	16454.34	5.53	84.02	13141.31	7.87	0.00	0.00	0.00	0.00	0.00	0.00
98.94	41669.36	7.54	96.09	40919.28	16.78	94.15	46620.43	28.97	95.58	20289.34	23.05
111.41	2827.42	4.45	114.22	67437.25	9.33	0.00	0.00	0.00	0.00	0.00	0.00
118.87	184148.82	6.78	117.87	33373.49	5.01	116.26	136258.21	17.16	117.74	111918.33	20.01
129.15	245028.28	4.59	129.21	405635.86	9.51	130.35	513708.02	10.10	130.81	319809.64	9.41
135.15	76516.73	4.24	0.00	0.00	0.00	0.00	0.00	0.00	0.00	0.00	0.00
144.99	46690.07	4.01	143.91	35732.57	5.52	144.81	60552.23	8.91	144.75	44931.14	9.78
274.65	109023.24	3.53	275.08	154426.24	7.91	275.36	215629.11	11.14	275.23	167620.70	12.06
285.53	336345.67	7.08	284.71	158968.37	7.43	279.96	44482.73	8.15	280.06	22158.73	7.46
296.74	489255.33	4.53	296.19	705559.58	8.12	295.08	1247333.25	12.57	294.43	766418.58	11.86
300.04	163929.12	2.84	305.29	38903.17	2.06	303.62	80917.22	4.35	302.98	119008.97	7.07
308.14	134943.07	3.67	307.58	86589.17	6.34	306.57	119609.65	6.76	305.91	66005.44	7.59

TABLE VII c)

*** RAMAN Spectra of a(cc)b [A_g] ***

100K			200K			ROOM			315K		
16.36	10846.96	10.19	14.98	5468.20	6.82	0.00	0.00	0.00	0.00	0.00	0.00
24.98	14099.64	6.33	21.72	18021.81	11.78	27.94	57442.32	27.59	28.01	55483.53	27.76
30.19	10724.39	5.27	32.92	25930.93	12.91	0.00	0.00	0.00	0.00	0.00	0.00
34.34	8561.53	4.02	0.00	0.00	0.00	0.00	0.00	0.00	0.00	0.00	0.00
38.37	12176.50	3.18	40.39	7007.84	5.02	41.02	9763.90	7.74	41.21	9366.85	7.11
43.02	1357.47	0.57	52.42	4032.43	3.69	53.19	926.63	0.86	0.00	0.00	0.00
55.96	31871.67	6.35	55.96	10835.48	6.55	56.83	2351.71	3.71	55.59	2422.05	4.83
67.86	19874.40	5.91	68.78	62122.61	12.03	65.99	55677.13	10.82	65.50	54123.58	11.01
71.77	6461.30	1.40	0.00	0.00	0.00	0.00	0.00	0.00	0.00	0.00	0.00
76.05	24800.83	4.62	0.00	0.00	0.00	79.37	52031.85	14.83	78.23	48781.23	14.80
86.38	25220.00	5.74	83.26	26295.71	8.75	0.00	0.00	0.00	0.00	0.00	0.00
99.52	48116.91	7.80	96.66	41375.19	15.42	95.63	43074.67	24.80	95.44	56456.17	30.41
111.58	6211.05	5.73	0.00	0.00	0.00	0.00	0.00	0.00	0.00	0.00	0.00
118.94	176880.67	7.07	116.90	176247.73	12.43	115.78	198835.34	18.26	115.22	188030.88	18.85
129.41	120991.69	4.46	129.36	148765.16	6.63	129.51	190390.76	8.57	128.35	148656.39	8.55
135.01	30448.85	3.57	133.86	13975.18	3.01	132.91	21196.81	4.66	131.41	54234.48	6.16
145.62	152289.30	4.29	144.67	141158.90	7.02	145.08	161958.52	10.01	144.33	161901.06	10.74
284.20	13396.26	3.70	285.76	105949.19	7.54	284.25	15257.85	6.53	287.65	136726.56	9.63
288.18	177903.29	5.93	291.87	83218.46	6.86	291.25	220589.65	8.48	291.81	408567.69	7.51
297.28	705878.39	4.56	296.06	791368.16	6.16	295.58	1062927.29	9.05	295.04	664234.96	8.70
300.52	335234.61	3.42	299.13	165017.19	3.75	303.57	318398.89	7.89	302.43	429437.42	8.90
308.52	140090.71	3.41	306.02	264594.12	6.68	306.66	56522.30	7.10	306.02	264594.12	6.68

TABLE VII d)

*** RAMAN Spectra at T = 100K [B1g] ***

b(ab)c			a(ba)c			a(ba)b		
17.04	2504.00	5.82	16.86	2451.02	5.26	16.15	2307.86	5.79
24.83	960.31	5.05	24.69	1223.07	5.55	23.99	1056.26	5.99
33.67	559.45	3.27	34.10	1286.65	5.61	33.61	1049.68	5.42
40.62	4915.62	7.63	40.63	3682.86	5.46	40.32	3233.38	5.85
50.34	4253.03	7.23	50.19	4387.17	7.42	50.14	3650.22	6.87
59.31	2334.29	3.82	59.57	2942.52	4.64	59.65	3273.00	5.26
65.02	2976.48	5.18	65.58	2923.02	5.31	65.93	2888.76	5.03
71.38	5882.95	8.51	71.95	6291.08	9.39	71.59	3730.35	6.47
81.08	41904.88	6.37	81.86	47562.27	6.71	81.29	40122.78	6.16
0.00	0.00	0.00	0.00	0.00	0.00	95.42	837.98	3.94
98.16	1585.06	2.63	98.84	1961.35	2.54	99.14	1160.81	1.60
114.74	57422.04	6.52	115.10	58228.73	5.97	114.91	52568.31	6.28
122.88	319921.61	7.12	123.17	342789.15	7.04	122.91	312233.60	7.07
133.87	14978.99	4.56	133.30	14052.74	6.13	133.98	9419.93	4.73
146.22	3942.85	4.98	147.87	2076.34	4.63	151.16	756.88	1.66
275.10	7819.27	4.47	274.94	7255.01	3.61	275.76	7402.94	4.13
279.68	7141.80	3.04	279.61	10278.57	4.44	280.39	6952.02	3.21
283.37	16239.65	5.02	283.93	23699.74	5.90	284.03	16825.48	5.21
288.40	24233.27	5.01	289.16	20262.26	4.05	289.25	17527.53	4.09
298.17	25639.50	5.66	298.52	29490.71	5.95	298.77	15631.24	5.77
312.53	1645.63	3.68	311.10	4129.07	7.42	312.51	2680.41	6.50

TABLE VII d)

*** RAMAN Spectra at T = 200K [B1g] ***

b(ab)c			a(ba)c			a(ba)b		
14.67	4212.22	22.03	14.94	5273.78	23.01	15.24	4015.95	20.43
19.32	1304.30	3.59	18.79	993.55	3.11	19.40	1024.50	3.02
32.67	318.19	3.15	32.21	593.90	6.38	32.48	317.52	4.92
46.27	12439.32	19.12	46.00	11595.53	20.65	46.51	10300.02	21.04
59.82	4329.41	9.47	59.13	4995.41	10.86	59.19	4102.78	10.02
69.27	4725.29	11.07	68.04	3071.05	8.60	68.24	3749.56	10.73
78.24	26795.09	7.84	78.32	38179.18	9.68	78.58	33659.05	9.23
82.20	15087.05	15.85	87.66	4344.60	11.97	87.51	6237.25	14.51
96.79	3056.06	12.01	96.32	2476.82	8.46	98.32	3228.33	10.62
112.61	45338.55	10.34	112.50	51772.15	11.10	112.90	41324.17	11.13
120.90	389864.31	10.99	120.44	370030.14	10.92	121.00	344596.25	10.61
132.71	10074.09	4.58	131.90	9252.04	5.26	132.52	7129.19	4.66
145.96	3176.62	4.76	145.53	553.62	1.54	0.00	0.00	0.00
277.72	13875.51	7.92	276.52	11821.48	8.47	275.59	5083.62	8.29
280.90	7396.07	3.76	281.17	17840.88	6.40	279.05	5027.03	4.81
284.13	10106.84	4.18	285.20	11823.90	5.37	282.91	20292.28	7.18
288.11	21957.28	6.67	288.54	9500.24	4.99	288.45	17984.19	7.29
296.76	26669.14	7.53	296.33	26730.03	8.20	297.74	9437.16	7.50
310.36	1554.78	4.38	307.68	4836.67	8.68	309.57	3012.14	8.69

TABLE VII d)

*** RAMAN Spectra at T = ROOM (300K) [B1g] ***

b(ab)c			a(ba)c			a(ba)b		
20.29	9894.45	32.37	21.26	3015.51	13.03	20.65	17186.70	35.94
0.00	0.00	0.00	29.43	187.95	7.16	0.00	0.00	0.00
44.44	1776.66	8.11	0.00	0.00	0.00	42.82	998.97	12.20
54.12	2895.68	11.93	53.75	705.65	6.23	52.90	6028.22	16.20
67.39	5526.05	13.70	65.21	158.76	1.65	65.48	3167.17	9.64
75.27	19050.47	9.37	75.41	26357.01	11.09	74.59	26304.65	10.77
83.04	11070.60	15.07	0.00	0.00	0.00	82.02	17514.76	20.83
94.24	15834.72	18.33	93.36	46904.79	33.26	96.15	42301.30	28.93
108.16	16308.48	15.84	111.73	61109.55	16.58	115.07	159975.06	16.23
118.62	418627.72	15.27	118.00	277198.76	11.88	119.58	351766.69	13.60
0.00	0.00	0.00	122.55	127867.24	11.04	0.00	0.00	0.00
130.03	3425.58	3.20	130.66	12799.48	7.12	129.46	15958.90	8.25
277.94	3431.12	11.33	278.39	22597.18	12.47	277.06	14557.45	13.90
283.24	45258.67	13.68	283.78	33187.40	10.20	283.33	46041.50	11.94
294.64	17575.74	9.56	294.36	11585.54	13.56	295.05	17643.22	11.52
307.05	1078.02	5.16	306.39	3498.55	9.01	305.40	5823.48	8.93

TABLE VII d)

*** RAMAN Spectra at T = 315K [B1g] ***

b(ab)c			a(ba)c			a(ba)b		
24.20	3878.91	19.90	0.00	0.00	0.00	23.29	6842.63	25.08
44.48	262.02	2.65	0.00	0.00	0.00	51.86	333.40	2.45
52.97	401.00	4.10	0.00	0.00	0.00	55.32	204.36	2.40
67.01	992.35	5.79	0.00	0.00	0.00	65.06	243.94	3.12
75.08	18850.38	10.24	0.00	0.00	0.00	74.49	24053.45	12.03
83.02	2172.23	8.17	0.00	0.00	0.00	0.00	0.00	0.00
93.24	28240.16	27.46	0.00	0.00	0.00	93.25	57256.11	34.35
0.00	0.00	0.00	0.00	0.00	0.00	109.97	32147.87	16.32
117.06	186988.99	16.61	0.00	0.00	0.00	116.60	175327.96	11.63
120.13	224405.77	13.97	0.00	0.00	0.00	121.27	211472.37	12.86
130.24	6284.55	5.81	0.00	0.00	0.00	130.66	9060.43	6.79
278.71	8639.04	13.38	0.00	0.00	0.00	277.62	12130.90	15.04
283.90	41502.26	13.02	0.00	0.00	0.00	283.13	38547.71	11.86
294.95	21693.43	10.74	0.00	0.00	0.00	295.02	7659.79	12.76
307.83	1107.74	5.72	0.00	0.00	0.00	305.64	2772.63	8.45

TABLE VII e)

*** RAMAN Spectra at T = 100K [B2g] ***

b(ca)c			a(ca)c			a(ca)b		
38.46	4088.67	6.92	39.20	5164.87	7.36	38.77	3566.56	6.44
47.88	600.01	0.24	48.47	933.20	1.30	48.38	705.83	0.38
54.82	4296.41	7.41	55.58	4864.29	7.44	55.35	4690.02	7.57
62.83	591.59	5.34	62.47	2507.17	8.30	62.63	2534.28	8.93
67.99	1736.12	1.33	68.56	2302.53	1.27	68.35	2367.05	1.35
73.33	9521.79	4.52	73.83	18915.59	5.96	73.60	18946.65	5.67
74.53	21438.24	15.18	78.95	10127.93	13.02	79.56	3675.13	5.36
94.72	26769.57	10.58	95.16	30114.04	11.58	95.08	36958.78	14.39
112.35	159801.14	5.85	113.01	174454.70	5.96	112.75	158190.98	5.67
119.26	99041.92	5.91	119.97	101506.71	5.59	119.52	96485.42	5.64
128.67	7825.01	2.52	130.61	32801.76	5.86	131.02	45498.15	7.60
133.11	49096.17	6.41	134.86	25194.37	3.50	134.97	14595.19	2.44
145.21	6595.56	4.63	145.22	13958.88	4.47	146.11	4424.29	5.41
275.42	11661.66	4.65	275.76	12377.67	4.56	275.75	12139.47	4.75
287.77	41219.96	6.99	288.05	38283.94	6.87	288.21	36856.00	6.81
296.44	17657.87	3.57	296.80	6084.51	2.89	296.62	5137.17	2.25
300.00	13616.84	2.99	300.52	8137.37	2.95	300.34	9358.17	2.97
307.45	1494.24	1.53	308.13	3067.92	3.14	308.40	992.08	2.35
316.13	6781.83	25.53	316.52	1281.58	6.17	316.72	1247.84	6.52

TABLE VII e)

*** RAMAN Spectra at T = 200K [B2g] ***

b(ca)c			a(ca)c			a(ca)b		
14.20	6508.55	44.42	15.26	177.13	6.77	14.93	6609.44	43.98
37.06	6468.41	10.32	37.29	4567.02	9.26	36.62	5090.36	9.33
[illegible] 02	1805.54	4.11	49.74	1223.50	3.30	49.40	1936.60	4.15
54.68	7144.36	12.51	54.97	3732.12	9.94	55.20	6171.19	11.47
71.85	36476.09	13.45	72.34	27821.50	12.12	71.87	34244.96	13.91
94.80	32374.56	16.01	95.40	25029.76	14.61	95.07	34021.65	16.66
111.84	264757.63	11.52	111.47	210896.23	10.49	111.30	220155.78	10.84
119.16	53554.23	8.81	118.54	76036.44	10.31	118.69	67614.86	10.32
129.27	44178.46	8.72	129.74	46655.28	8.06	129.27	43020.63	8.45
132.36	33754.51	6.08	132.96	18795.32	4.88	132.36	23755.85	5.84
145.01	9837.58	6.25	144.99	9107.91	5.83	146.26	1939.65	5.82
277.15	9853.75	6.86	277.51	11549.30	8.07	277.78	12331.57	8.68
287.29	52275.52	9.98	287.67	38591.57	9.24	287.77	37099.87	8.88
297.14	56076.63	7.64	298.04	15825.19	8.84	297.48	15608.85	7.43
307.18	608.45	0.41	307.16	1650.21	4.64	288.21	36856.00	6.81

TABLE VII e)

*** RAMAN Spectra at T = ROOM (300K) [B2g] ***

b(ca)c			a(ca)c			a(ca)b		
0.00	0.00	0.00	0.00	0.00	0.00	15.24	9948.81	49.70
34.00	3555.37	13.90	34.59	5548.21	15.50	34.45	6081.45	13.17
54.77	2545.21	10.27	54.39	3556.13	10.24	48.88	3407.67	5.45
48.86	2151.64	5.18	49.14	2503.80	5.05	54.52	6665.85	12.26
69.23	13807.25	19.04	69.20	18926.94	18.37	69.03	30016.76	21.60
101.10	54883.59	28.00	98.21	47330.57	29.55	96.44	64754.59	29.06
109.77	203701.17	15.50	110.07	299051.01	16.39	109.93	341257.87	16.04
114.47	43882.24	12.39	115.95	53818.41	13.86	118.75	31108.74	15.17
123.37	7953.96	9.12	0.00	0.00	0.00	0.00	0.00	0.00
129.90	59501.50	7.12	128.06	24729.99	8.37	129.55	80230.23	7.77
0.00	0.00	0.00	131.26	57222.75	6.90	0.00	0.00	0.00
144.75	4436.43	5.39	145.60	5002.69	5.06	0.00	0.00	0.00
276.07	2220.48	9.23	278.46	11276.65	15.76	279.31	13200.12	14.78
285.72	49307.50	14.00	285.47	45709.29	11.98	285.62	47119.35	11.79
295.16	43622.25	9.83	295.05	9133.71	9.28	294.93	11339.26	8.32
304.64	1651.50	4.04	303.61	2545.20	7.90	0.00	0.00	0.00

TABLE VII e)

*** RAMAN Spectra at T = 315K [B2g] ***

b(ca)c			a(ca)c			a(ca)b		
33.32	4592.05	17.36	0.00	0.00	0.00	32.21	4745.98	17.30
53.48	2849.86	10.06	0.00	0.00	0.00	52.87	2767.46	7.18
48.64	1950.00	5.04	0.00	0.00	0.00	48.27	1387.79	2.62
68.05	13770.38	21.96	0.00	0.00	0.00	68.08	17618.78	24.30
93.43	14696.67	26.33	0.00	0.00	0.00	95.89	24283.92	24.12
109.79	321358.43	18.80	0.00	0.00	0.00	109.77	344377.03	18.36
128.56	32990.85	7.41	0.00	0.00	0.00	128.29	47973.48	6.34
130.90	30435.52	6.65	0.00	0.00	0.00	131.01	13478.33	4.38
145.21	2782.39	4.18	0.00	0.00	0.00	0.00	0.00	0.00
281.11	13123.77	14.53	0.00	0.00	0.00	278.88	14402.30	15.90
285.47	39966.70	13.08	0.00	0.00	0.00	284.95	35491.46	10.84
294.52	52704.63	10.99	0.00	0.00	0.00	291.31	4093.18	7.54
304.12	1414.52	3.82	0.00	0.00	0.00	295.06	7348.37	8.31

TABLE VII f)

*** RAMAN Spectra at T = 100K [B3g] ***

b(bc)c			a(cb)c			a(bc)b		
16.62	566.59	6.98	17.10	1229.78	6.89	16.59	1597.81	10.17
27.55	1852.37	8.97	26.68	3250.26	9.34	27.03	2694.67	8.52
0.00	0.00	0.00	33.36	628.25	3.22	33.24	325.78	0.82
38.61	1395.56	6.00	38.19	1267.38	3.34	37.82	872.41	1.94
47.37	5062.98	5.14	48.52	17333.94	10.00	48.37	13946.97	9.62
51.47	4118.72	4.57	0.00	0.00	0.00	0.00	0.00	0.00
71.92	9947.42	5.37	71.18	13945.48	6.27	71.99	13849.15	6.87
76.58	6124.37	3.20	75.96	8854.98	3.97	76.54	4117.62	2.11
86.44	3332.89	7.93	86.55	6031.90	8.93	86.67	5255.11	9.61
99.94	349.02	0.48	99.41	1827.31	5.53	99.84	1776.76	6.09
115.53	21780.86	6.84	114.21	21853.49	7.26	116.69	44579.94	7.61
119.50	63951.00	6.00	118.66	80558.58	6.25	119.64	36506.46	4.32
133.64	174348.11	5.51	132.76	221936.20	6.05	133.07	165346.64	4.95
0.00	0.00	0.00	0.00	0.00	0.00	138.44	9056.10	10.78
157.86	2922.32	6.10	157.95	3871.82	5.61	157.88	4361.41	6.90
275.39	2585.52	3.79	274.47	2909.23	3.14	275.30	3284.78	4.47
287.87	59183.60	4.90	286.99	66479.77	5.01	287.77	61772.84	4.69
299.50	19291.60	5.63	298.85	24170.53	6.22	299.30	22678.40	5.94
309.62	3782.03	10.30	309.44	2457.41	6.74	309.43	2889.12	8.75

TABLE VII f)

*** RAMAN Spectra at T = 200K [B3g] ***

b(bc)c			a(cb)c			a(bc)b		
16.84	2705.65	11.79	16.80	2962.16	12.36	16.57	3528.59	15.17
28.12	2951.32	13.33	28.60	2750.18	13.74	28.71	2652.11	14.84
38.28	4477.30	9.20	38.82	4419.45	9.18	39.31	4436.04	9.26
45.44	6047.54	5.24	45.71	6327.82	5.06	46.27	6298.57	5.09
48.60	2988.69	4.66	49.07	3385.46	4.42	49.50	3045.46	4.45
68.86	6014.28	4.46	69.38	6425.11	4.29	69.16	5402.95	4.16
73.22	9720.99	6.90	73.71	10501.41	6.61	73.25	9805.05	6.44
83.14	3009.38	11.96	83.17	2886.52	12.17	83.55	3480.31	15.00
116.42	91680.15	11.74	115.78	88339.26	11.16	117.35	104687.11	10.89
119.26	15262.82	6.02	118.79	24758.58	6.25	120.20	2620.83	4.41
131.73	181827.32	7.03	131.66	214285.55	7.22	132.53	195461.47	7.13
275.44	2065.43	5.09	275.75	740.72	3.52	275.40	779.19	3.84
286.24	60699.34	7.40	286.65	73031.13	7.50	286.44	68442.72	7.74
297.60	26636.70	11.15	298.29	24176.88	10.24	297.80	15816.49	8.75
307.78	1277.66	5.07	308.52	1639.53	7.17	304.66	6189.64	16.58

TABLE VII f)

*** RAMAN Spectra at T = ROOM (300K) [B3g] ***

b(bc)c			a(cb)c			a(bc)b		
31.42	6393.16	8.95	30.98	4780.59	9.07	31.49	5933.37	9.03
38.36	5197.12	6.84	38.15	4655.42	8.12	38.25	4699.12	6.84
43.51	7505.84	4.28	44.32	6327.12	4.86	43.49	6671.37	4.21
70.64	6823.18	4.80	72.57	5560.48	5.27	70.10	5907.83	4.11
46.93	5068.76	3.90	47.72	4230.26	4.05	46.86	5165.64	3.78
66.65	4052.19	3.13	68.42	3626.42	3.56	66.31	2879.28	2.36
76.08	6952.88	11.17	78.13	6663.04	12.34	75.23	7038.97	10.44
115.56	185397.21	16.00	117.65	140471.26	15.61	115.86	159983.40	15.39
130.53	235358.36	8.97	132.23	170885.87	8.58	130.77	213455.06	8.65
284.57	95897.42	11.83	285.42	65803.74	11.68	284.57	87791.73	11.92
294.65	11306.00	9.00	295.70	18989.46	12.19	294.38	9541.63	8.43
302.44	6494.23	11.44	305.00	2422.82	7.07	301.32	9590.09	14.58

TABLE VII f)

*** RAMAN Spectra at T = 315K [B3g] ***

b(bc)c			a(cb)c			a(bc)b		
30.83	4050.54	6.98	0.00	0.00	0.00	29.07	5532.33	9.22
36.86	3597.62	6.50	0.00	0.00	0.00	36.41	5088.69	8.04
42.18	5358.77	4.71	0.00	0.00	0.00	42.58	6199.75	5.04
45.43	4934.54	4.91	0.00	0.00	0.00	46.11	6845.34	4.56
65.34	2475.34	3.18	0.00	0.00	0.00	70.25	5786.62	4.65
69.47	5447.55	5.59	0.00	0.00	0.00	75.93	6515.29	11.89
75.83	5506.53	13.77	0.00	0.00	0.00	66.28	2918.91	2.60
114.64	131770.10	17.10	0.00	0.00	0.00	115.60	159363.73	16.47
129.41	144909.12	8.73	0.00	0.00	0.00	130.73	198781.53	8.87
282.53	52387.60	11.84	0.00	0.00	0.00	277.62	2843.38	11.03
291.70	18982.69	16.15	0.00	0.00	0.00	284.66	69473.22	11.37
302.36	1198.20	7.62	0.00	0.00	0.00	293.88	27069.57	16.44
0.00	0.00	0.00	0.00	0.00	0.00	304.56	1131.72	4.63

TABLE VIII

EXPERIMENTAL AND CALCULATED FREQUENCIES OF Rb_2ZnCl_4 for A_g, B_{1g}, B_{2g}, and B_{3g} modes at 315 K (Pnam Structure)

EXPERIMENT				THEORY			
A_g	B_{1g}	B_{2g}	B_{3g}	A_g	B_{1g}	B_{2g}	B_{3g}
26-28	23	32	30	36	40	-25	-32
34-36	--	48	36	39	--	8	24
41-46	46	53	42, 46	60	52	58	45
52-56	54	68	66, 70	63	71	75	78
65-67	66	--	--	89	84	--	--
---	75	94	76	--	98	97	99
78-82	83	--	--	119	117	--	--
94-96	--	--	--	126	--	--	--
---	93	--	--	--	135	--	--
109-110	109	--	--	135	--	--	--
115-119	117	110	115	--	139	108	125
128-131	120	128	--	155	--	--	--
132-133	130	131	130	--	186	169	170
144-145	146	145	--	181	190	--	--
275-277	278	278	278	276	--	--	--
285-288	283	285	284	--	276	274	267
294-295	295	295	293	291	304	--	--
302-306	306	304	303	320	333	--	--

TABLE IX

EXPERIMENTAL AND CALCULATED FREQUENCIES OF K_2SeO_4 for A_g, B_{1g}, B_{2g}, and B_{3g} modes at 140 K (Pnam Structure)

EXPERIMENT				THEORY			
A_g	B_{1g}	B_{2g}	B_{3g}	A_g	B_{1g}	B_{2g}	B_{3g}
36-38	43	50	45	39	57	52	51
73-75	--	74, 81	64	67	--	84	78
95-96	75	94	89	96	89	137	110
104-105	95	119	119	122	107	143	114
122-123	109	--	--	128	148	--	--
---	119	148	141	--	157	192	164
142	144	--	--	--	185	--	--
161	--	--	--	147	--	--	--
---	156	--	--	179	191	--	--
332	--	332	332	292	--	--	--
342-344	342	342	345	--	336	311	334
412-413	--	413	--	438	--	--	--
420	420	421	418	--	443	433	446
430-431	431, 444	431, 452	431, 445	458	482	--	--
813-814	814	812	814,				
822-823	823	823	822	Extra lines			
830-831	831	831	831				
843-844	844	843	843	840	844	--	--
866-867	vw	866	866	873	--	--	--
876-878	878	879	876	--	888	876	874
905-906	905	905	905	910	906	--	--

Note that vw stands for very weak.

We begin with the classification of the internal modes. For K_2SeO_4 and Rb_2ZnCl_4 as shown in Tables X and XI, these fell into three groups; a high frequency quartet, an intermediate frequency triplet, and a low frequency doublet.

TABLE X

CLASSIFICATION OF INTERNAL MODES OF K_2SeO_4 AT 140 K

(Pnam STRUCTURE)

Irreducible Representation and Polarization		Frequency (cm^{-1}) ν_2 (342)		ν_4 (416)			ν_1 (833)	ν_3 (875)		
		332	342	413	420	431	843	866	877	905
A_g	aa bb cc									
B_{1g}	ab	–								
B_{2g}	ac									
B_{3g}	bc			–						

TABLE XI

CLASSIFICATION OF INTERNAL MODES OF Rb_2ZnCl_4 AT 315 K

(Pnam STRUCTURE)

Irreducible Representation and Polarization		Frequency (cm^{-1}) ν_2 (79)		ν_4 (104)			ν_1 (275)	ν_3 (306)		
		109	117	128	132	145	278	285	294	305
A_g	aa bb cc									
B_{1g}	ab									
B_{2g}	ac	–								
B_{3g}	bc	–		–		–				

Of the observed lines, the solid lines in the Table are those that are assumed to be "allowed" by the supposed Pnam point symmetry and the "dashed" lines are those that are "forbidden". Note that for K_2SeO_4, except for two very weak (and hence, not included) lines, there is a total of 9 observed lines for each factor group (these two "missing" lines were observed in reference 1): the same nine for each group. For the Rb_2ZnCl_4, there are four such missing lines. (Small variations in peak frequency of the order of a few wavenumbers have been ignored in this Table.)

The origin of the rationale for the assignments in Table X and XI is presented in the following paragraphs.

We begin by examining the high frequency quartet. The strongest line by far in the selenate spectrum came from the breathing mode at 843 cm^{-1}, the lowest of these four frequencies. This line is "forbidden" in the cross-polarized (ac) and (bc) spectra and so we seek the corresponding line for Rb_2ZnCl_4 by searching for a strong line in diagonal [(aa), (bb), (cc)] spectra that is weaker in the cross-polarized spectra. However, for adequate resolution, the spectra in the incommensurate phase at 200 K are examined first. The strongest line in the diagonal spectra occurs at about 294 cm^{-1}. The remaining lines in this region number more than three; however, for comparison with the selenate, we fix on the three other higher intensity lines at about 278, 285, and 305 cm^{-1}. In the (ac) and (bc) spectra the strongest line is at 285 cm^{-1} so we identify the 294 cm^{-1} line as corresponding to the 843 cm^{-1} selenate line and the 285 cm^{-1} line as corresponding to the 877 cm^{-1} selenate line. <u>Note the reversal of order</u>-- for Rb_2ZnCl_4, if we assume the breathing mode has

the highest intensity in A_g, then it is not the lowest frequency line in the quartet. A possible explanation of this anomalous behavior is given later.

Using this approach of comparison with the theory and with the Raman spectrum of K_2SeO_4, a tentative identification of all of the lines in the Rb_2ZnCl_4 spectra can be made. A straightforward one-to-one correspondence of lines could not be made since there were more resolved lines in the Rb_2ZnCl_4 spectra than for the selenate, and more than predicted by selection rules. However, in the selenate, isotopic splitting is small because only one of the possible isotopes has significant relative abundance (excluding the selenium which does not contribute much to the possible isotopic splitting). In contrast, the two main chlorine isotopes both contribute to the Rb_2ZnCl_4 spectra, introducing a maximum line-splitting of about one percent. Consequently, we identify groups of lines as correlating with corresponding, single selenate lines. Our analysis of the lines calculated from the fit to the 315 K spectra is shown in Table VII. These correlations, at this stage, are still tentative. The compression of this spectrum relative to the selenate spectrum, particularly in the region of overlap of the lattice modes and internal modes, makes unique identifications difficult. Also, frequency shifts from inter-mode coupling are likely with such close inter-mode spacing, a possibility that has not been considered at all in this analysis. The theoretical calculations so far have been on only the ideal Pnam structure and have not shown any of th coupling effects that might be seen in the actual non-ideal structures.

If inter-mode coupling takes place, then the factor group analysis we have applied here will not be valid for the coupled modes. In particular, we note that the theoretical A_g line at 276 cm^{-1} is nearly degenerate (accidentally) with the 274 and 267 cm^{-1} B_{2g} and B_{3g} modes. Because of the disorder in the $ZnCl_4^{2-}$ sub-lattice such close-spaced lines can couple harmonically and the resulting coupled modes would have mixed symmetry. Hence, the line of highest intensity in A_g would no longer be correlated uniquely with the breathing mode, and the observed, apparent frequency interchange is reasonable in this context of a coupled-mode spectrum. This possibility is discussed in some detail below, in Section VII.

VI. Temperature Dependence of the Highest Frequency "Forbidden" Line in the Ag Spectrum

A. We include here for completeness a reprint of a brief report that has recently appeared in Supplement 2 of volume 24 of the Japanese Journal of Applied Physics 24, 790 (1985).

Proceedings of the Sixth International Meeting on Ferroelectricity, Kobe, 1985
Japanese Journal of Applied Physics, Vol. 24 (1985) Supplement 24-2, pp. 790–792

Analysis of the Raman Spectrum of the Higher Frequency Modes of Rb_2ZnCl_4

V. KATKANANT, F. G. ULLMAN* and J. R. HARDY

Behlen Laboratory of Physics, University of Nebraska, Lincoln, Nebraska 68588-0111
**Behlen Laboratory of Physics and Department of Electrical Engineering, University of Nebraska, Lincoln, Nebraska 68588-0511*

The stretching-region (250–330 cm^{-1}) internal modes of Rb_2ZnCl_4 were studied by Raman-scattering from 190 to 330 K. Four lines, peaking at about 275, 285, 295 and 304 cm^{-1} are clearly resolved below the normal-to-incommensurate phase transition (307 K in these measurements); above 307 K, the four merge into three and the 285 cm^{-1} peak is no longer detectable. The derivatives of these spectra were fitted to the derivative of an overlapped, spectrometer-corrected, four-Lorentzian lineshape. The resulting temperature dependence of the integrated intensity of the 285 cm^{-1} peak decreases by at most a factor of 3 up to 305 K whereas the square of the order parameter in this range decreases by a factor of about 50. Thus, its disappearance above 307 K is as yet unexplained.

§1. Introduction

As part of a study of the full Raman spectrum of rubidium tetrachlorozincate, Rb_2ZnCl_4, we have made a detailed analysis of the internal modes in the 250–320 cm^{-1} range for several temperatures from 190 K to 330 K. The other internal modes are not unequivocally identified but appear to lie in the 80–140 cm^{-1} range which overlaps the lattice-mode portion of the spectrum. The impetus for this work came from an earlier study of K_2SeO_4[1] in which the number of observed internal modes were consistently greater than predicted by symmetry group theory for its X-ray-determined, beta potassium-sulfate structure. This was explained as arising from a loss of inversion symmetry in the selenate sublattice, presumably from small deviations of the selenates from their X-ray-predicted positions. This symmetry-lowering would make all of the infrared lines Raman-active also, which, however, was not observed. Therefore, it was suggested that the selenates are only weakly coupled to one another and orientationally disordered so that they behave approximately like free ions with the normal-mode degeneracies removed by the crystal field generated primarily by the cation sublattice.

We have initiated Raman-scattering studies on isomorphous compounds with similar phase transition behavior. The results of this first part of our investigation of Rb_2ZnCl_4 and its relation to the earlier work on K_2SeO_4 are the subject of this article.

§2. Phase Transitions in Rb_2ZnCl_4

The various phases and corresponding relevant properties of Rb_2ZnCl_4 are summarized below in Table I.

The measurements described here were made in the incommensurate phase III and in the normal-commensurate phase II.

A correlation table for the internal modes in phase II is given in Table II. As can be seen from Table II, a loss of inversion symmetry gives 36 allowed Raman-active internal modes.

§3. Raman Scattering Measurements on Rb_2ZnCl_4

The K_2SeO_4 spectrum extends to nearly 1000 cm^{-1} and so the two groups of internal modes, bending and stretching, are well-separated from the lattice modes, and from each other, although some cooling below room temperature is necessary to identify all of the lines, unequivocally. In Rb_2ZnCl_4, the entire spectrum lies below about 330 cm^{-1} and the bending modes and lattice region overlap. The stretching region, however is isolated and lies between 250 and 330 cm^{-1}. At 300 K, the stretching region consists of a broad line that can be seen in A_g spectra to consist of three overlapped lines with peaks at about 275, 295, and 304 cm^{-1}. At lower temperatures, the lines narrow and a fourth peak is resolved at about

Table I. Solid Phases of Rb_2ZnCl_4

Transition Temperature	$T=74.6$ K	$T=189$ K	$T=302$ K	
Phase	V Antiferro-distortive	IV Ferroelectric	III Paraelectric	II I* Paraelectric
Space Group	$A1a1$	$Pna2_1(C_{2v}^9)$	Modulated	$Pnam(D_{2h}^{16})$
Molecules/ Cell	24	12	12	4
Lattice Constants		3a b c	3a b c	a= 9.25[illegible] Å b=12.726 Å c= 7.282 Å

*Phase I should be hexagonal in analogy with K_2SeO_4 but has not been observed for this compound.[2]

Table II. Correlation table for internal modes of β-potassium sulfate structure, D_{2h}^{16}.

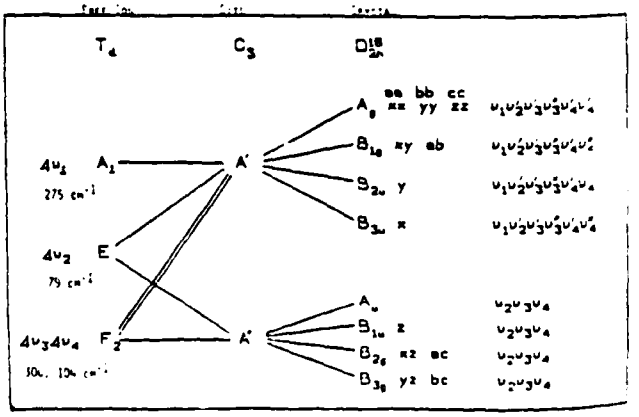

285 cm^{-1}. In B_{2g} and B_{1g} spectra, two weaker lines at 285 and 295 cm^{-1} can be seen, the 285 cm^{-1} line being the stronger. We, therefore, identify the 295 cm^{-1} line as the symmetric breathing mode which should be the strongest line in the internal mode spectrum and should be forbidden in B_{2g} and B_{1g} if the $ZnCl_4$ ions are in the positions prescribed by the β-potassium sulfate structure. It is known,[3] however, that the $ZnCl_4^{2-}$ ions are rotated significantly from those positions and disordered in phase II. So, in this case, we have the situation that was postulated for K_2SeO_4. If we assume that model to pertain to Rb_2ZnCl_4 also, there should be four Raman-active stretching modes in the A_g spectrum for phase II. From the measured spectrum however, we see only three until the sample is cooled below 300 K into phase III. It is therefore not possible from these data alone to state that either the 285 cm^{-1} peak that appears below 300 K is present in phase II and obscured by stronger neighboring lines, or that it actually vanishes at or below the III-II phase transition at about 307 K (in our measurement).

To determine which of these possibilities is actually the case, we undertook a detailed analysis of both the c(bb)a and a(bb)c spectra, which do not differ significantly, in the 190–330 K temperature range. A theoretical lineshape, consisting of four overlapped Lorentzian functions, convolved with the slit function of the Raman spectrometer[4] was assumed. The derivative of the experimental spectrum was then fitted to the derivative of this lineshape function. Derivative fitting eliminates any frequency-independent background. To reconstruct the data from the calculated values, a constant background can then be calculated from the least-squares fit to bring all spectra to the same zero. No evidence for any other background was found for this region. The reconstructed and experimental spectra are shown in Fig. 1 for several temperatures. Above 305 K, the four-peak lineshape is rejected by the fit (the 285 cm^{-1} peak has zero weight) giving a three peak function. Birefringence measurements under identical conditions of laser power, spot size, sample chamber, etc. show the phase transition to occur close to a measured temperature, at the sample holder, of 307 K within about ± 1 K. Consequently, even with the improved resolution obtained from this fitting procedure, the presence of the 285 cm^{-1} peak above the III-II phase transition is not established.

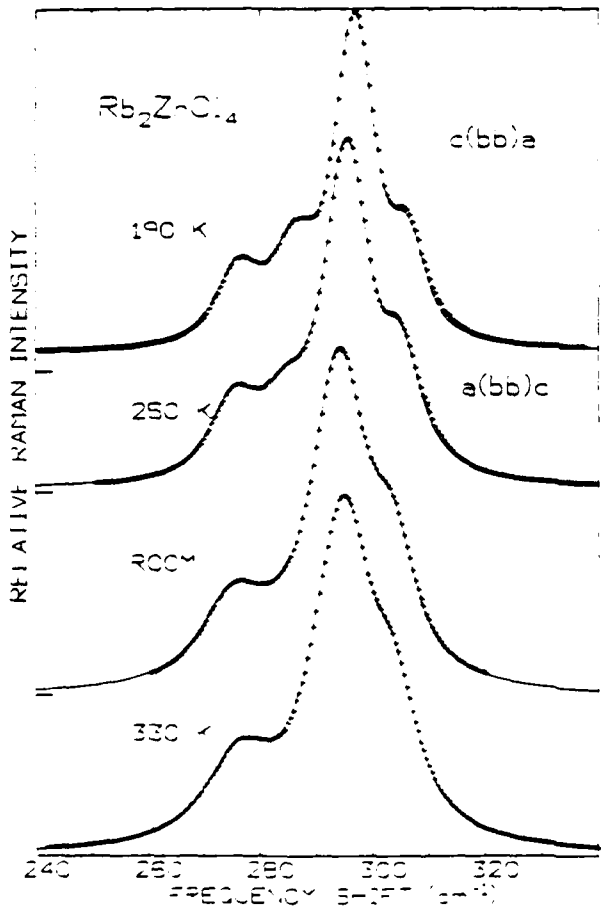

Fig. 1. Calculated (solid line) and experimental (points) spectra at 190 K, 250 K, 300 K and 330 K.

We can, however, examine the temperature dependence of the integrated intensities. If the 285 cm^{-1} peak does, in fact, disappear above the III-II transition because of the transition, its integrated intensity in phase III should decrease as the square of the order parameter whose temperature dependence is known from X-ray diffraction measurements[5] on satellite lines in phase III. The integrated intensities, normalized to the 295 cm^{-1} peak, for the three other peaks are plotted in Fig. 2(a)–(c). Over this temperature range, the satellite intensity decreases by a factor of about 50.[5] The Raman intensities of the 275, 295 and 305 cm^{-1} lines increase superlinearly as the temperature increases while the 285 cm^{-1} line intensity decreases slightly by a factor of three at most. Above 295 K, all intensities decrease. At 305 K, the data are represented equally well by a three or four peak fit whereas, as stated before, the four peak fit is rejected at 310 K and above.

§4. Conclusions

From these integrated intensity results, we conclude

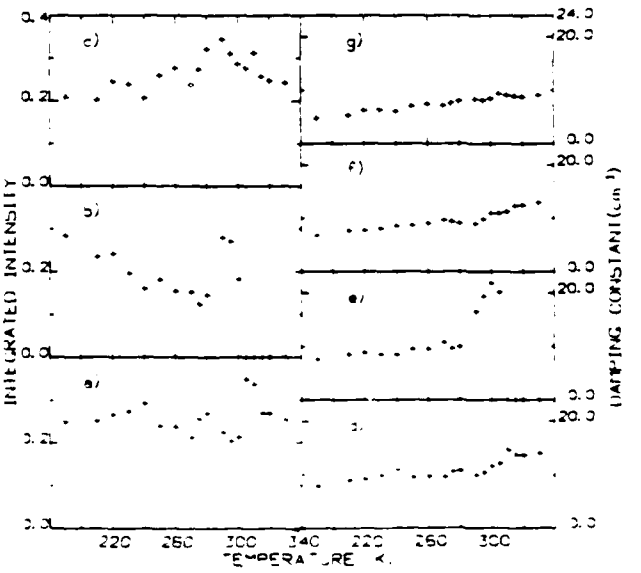

Fig. 2. Integrated intensities normalized to the 295 cm^{-1} intensity: a) 275 cm^{-1}, b) 285 cm^{-1}. Calculated linewidths (FWHM) of the four A_g modes vs. temperature: d) 275 cm^{-1}, e) 285 cm^{-1}, f) 295 cm^{-1} and g) 305 cm^{-1}.

that none of these peaks vary with temperature in the same way as the square of the order parameter and so their temperature dependence cannot be associated with the III–II phase transition. They do, however, appear to behave anomalously near the transition and further, the behavior of the 285 cm^{-1} peak differs from the other three as can be seen clearly from Fig. 2(d)–(g) which shows the temperature dependence of the linewidths (FWHM). Finally, neither the presence nor the absence of the 285 cm^{-1} peak in the A_g spectrum in phase II is established by these results.

Acknowledgements

The authors are grateful to Professor R. D. Kirby for advice and numerous helpful discussions and to D[illegible]. Arend for the crystal from which these samples were cut.

References

1) N. E. Massa, F. G. Ullman and J. R. Hardy: Phys. Rev. B27 (1983) 1523.
2) M. Quilichini, J. P. Mathieu, M. Lepostollec and N. Toupry: J. Physique 43 (1982) 787.
3) K. Itoh, A. Hinasada, H. Natsunaga and E. Nakamura: J. Phys. Soc. Jpn. 52 (1983) 664.
4) D. Galliardt: private communication.
5) S. R. Andrews and H. Mashiyama: J. Phys. C16 (1983) 4985.

B. Addendum to Preprint

Space limitations prevented the inclusion of some results in the foregoing preprint that should be mentioned in this report. Specifically, in the following figures we illustrate how the derivative-fitting method identified the presence of an almost completely overlapped peak in the spectrum. Figure 6a) shows the spectrum and its derivative at 250 K where four major peaks can clearly be seen. At 298 K, the spectrum can be fitted with three or four peaks but the four-peak fit, shown in Fig. 6b) can be seen to be better than the three-peak fit in the region shown by the arrow in Figure 6c). At higher temperature, there is no difference between the three- and four-peak fits. A three-peak fit for 315 K is shown in Figure 6d). (We are grateful to Professor Y. Yacoby for helpful discussions of the derivative fitting method.)

Fig. 6

a) 250 K, spectrum and derivative 240-340 cm^{-1}

b) 298 K, fit to four major peaks

c) 298 K, fit to three major peaks

d) 315 K, fit to three major peaks

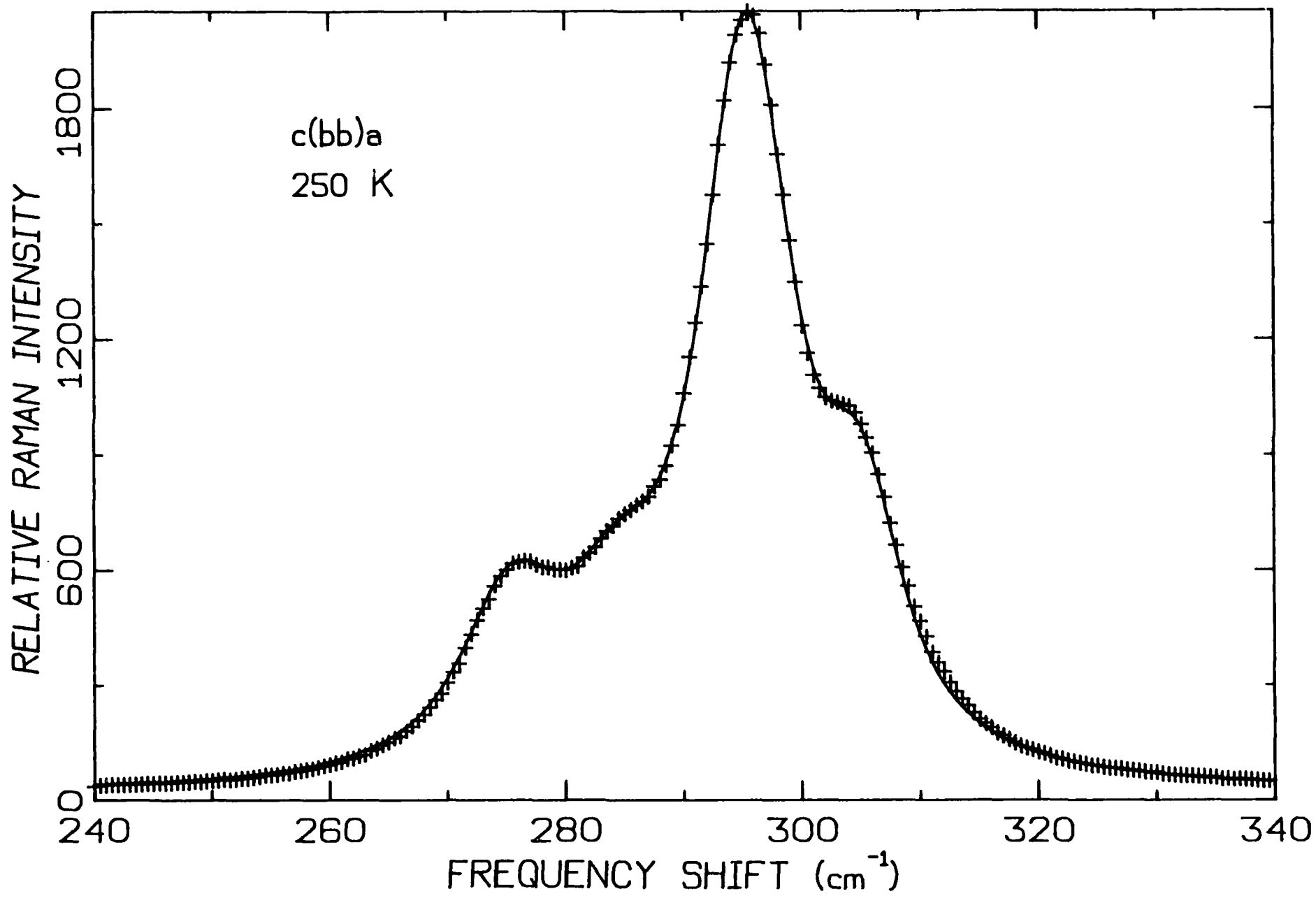
c(bb)a
250 K
RELATIVE RAMAN INTENSITY
0
600
1200
1800
240
260
280
300
320
340
FREQUENCY SHIFT (cm^{-1})

6a

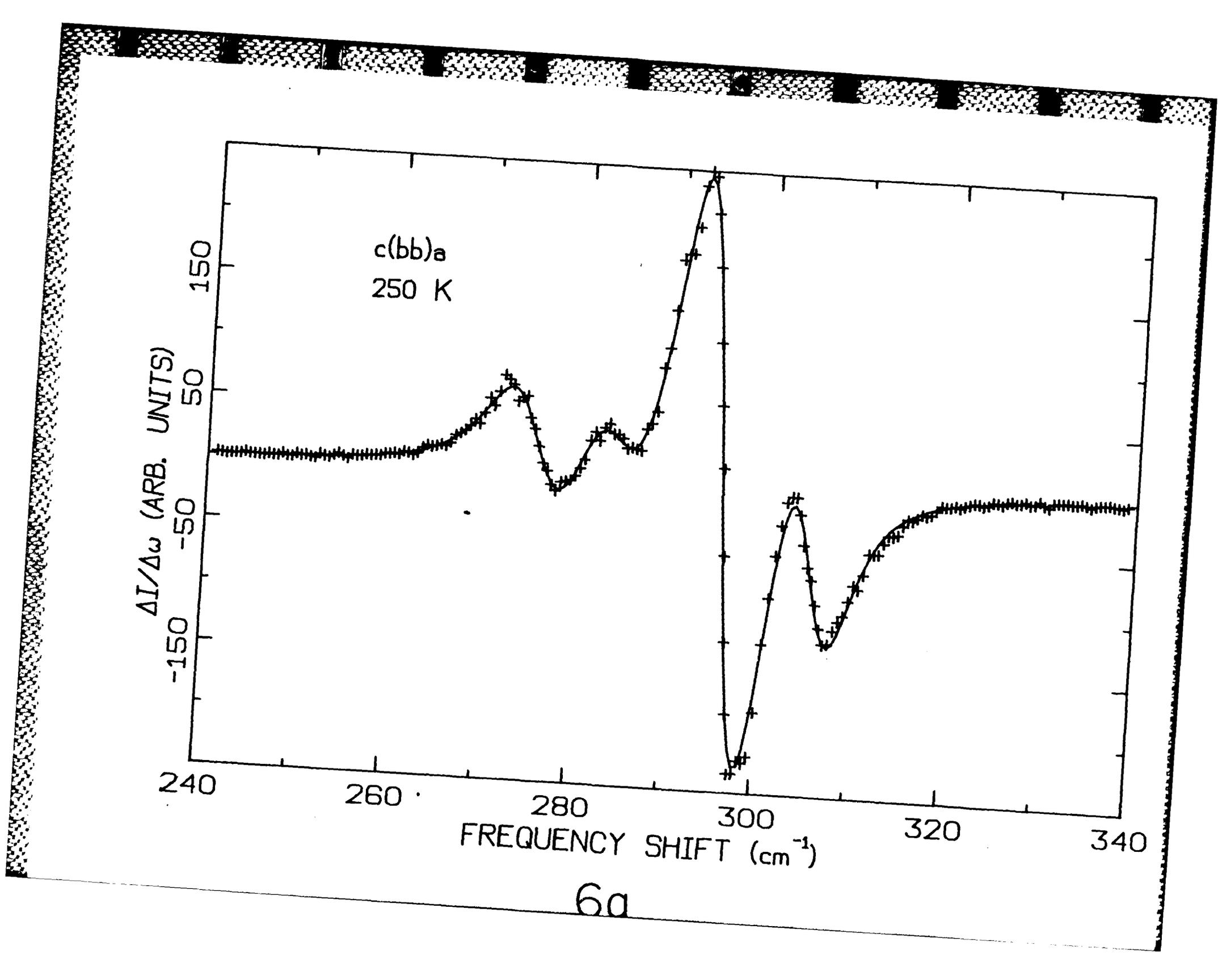
c(bb)a
250 K
ΔI/Δω (ARB. UNITS)
150
50
-50
-150
240
260
280
300
320
340
FREQUENCY SHIFT (cm⁻¹)

6a

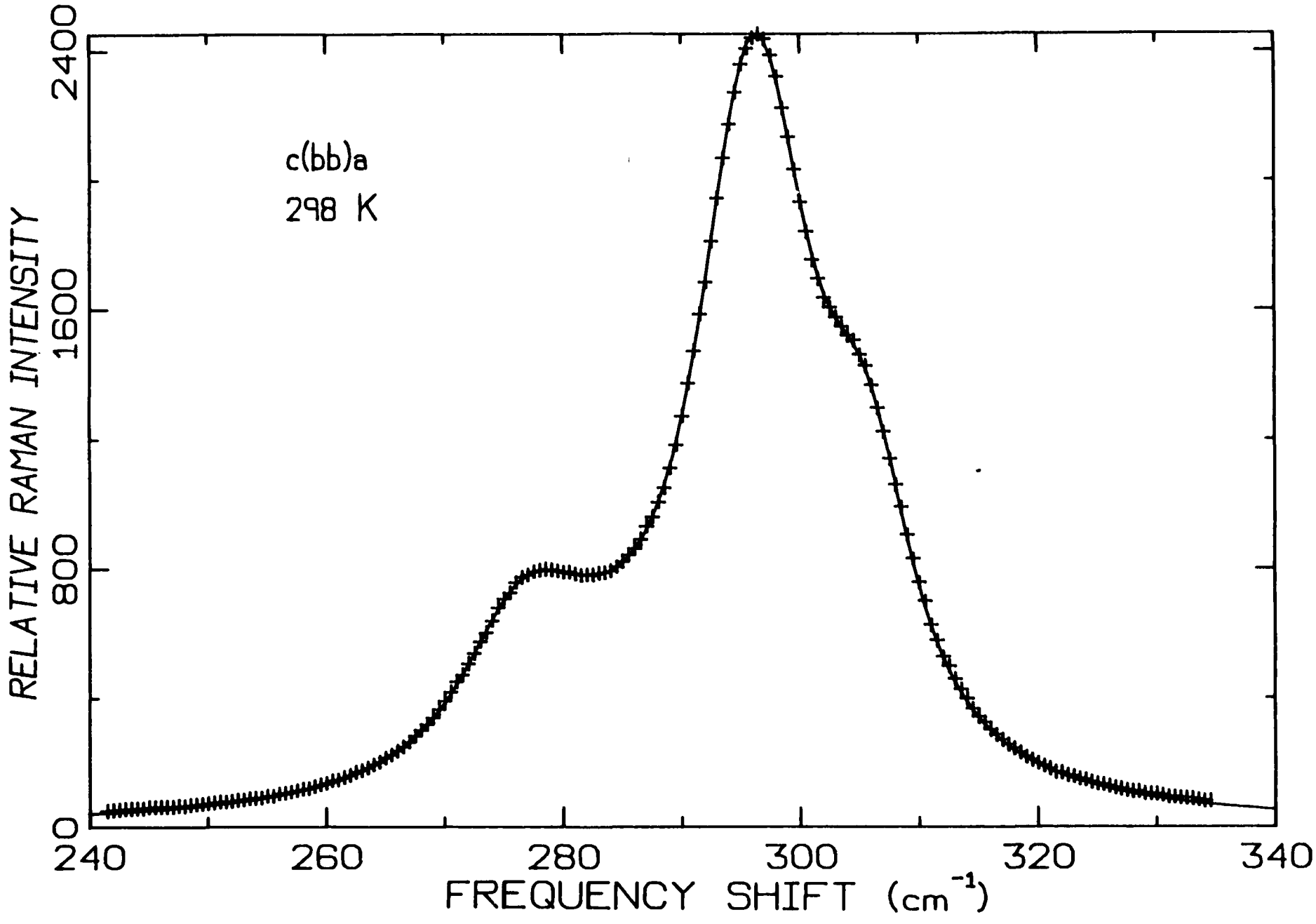
c(bb)a
298 K
RELATIVE RAMAN INTENSITY
0
800
1600
2400
240
260
280
300
320
340
FREQUENCY SHIFT (cm^{-1})

6b

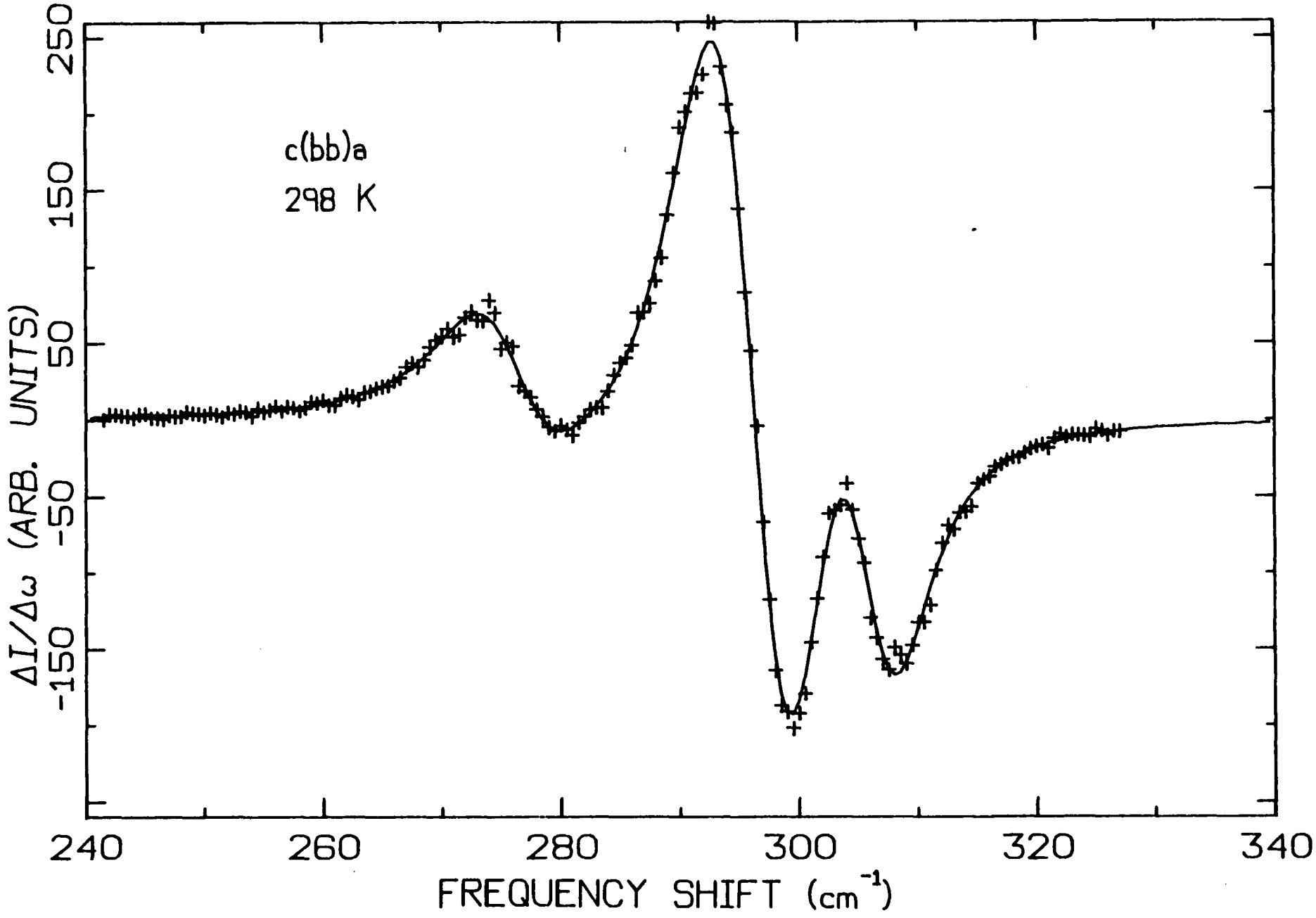
c(bb)a
298 K
250
150
50
-50
-150
ΔI/Δω (ARB. UNITS)
240
260
280
300
320
340
FREQUENCY SHIFT (cm⁻¹)

6b

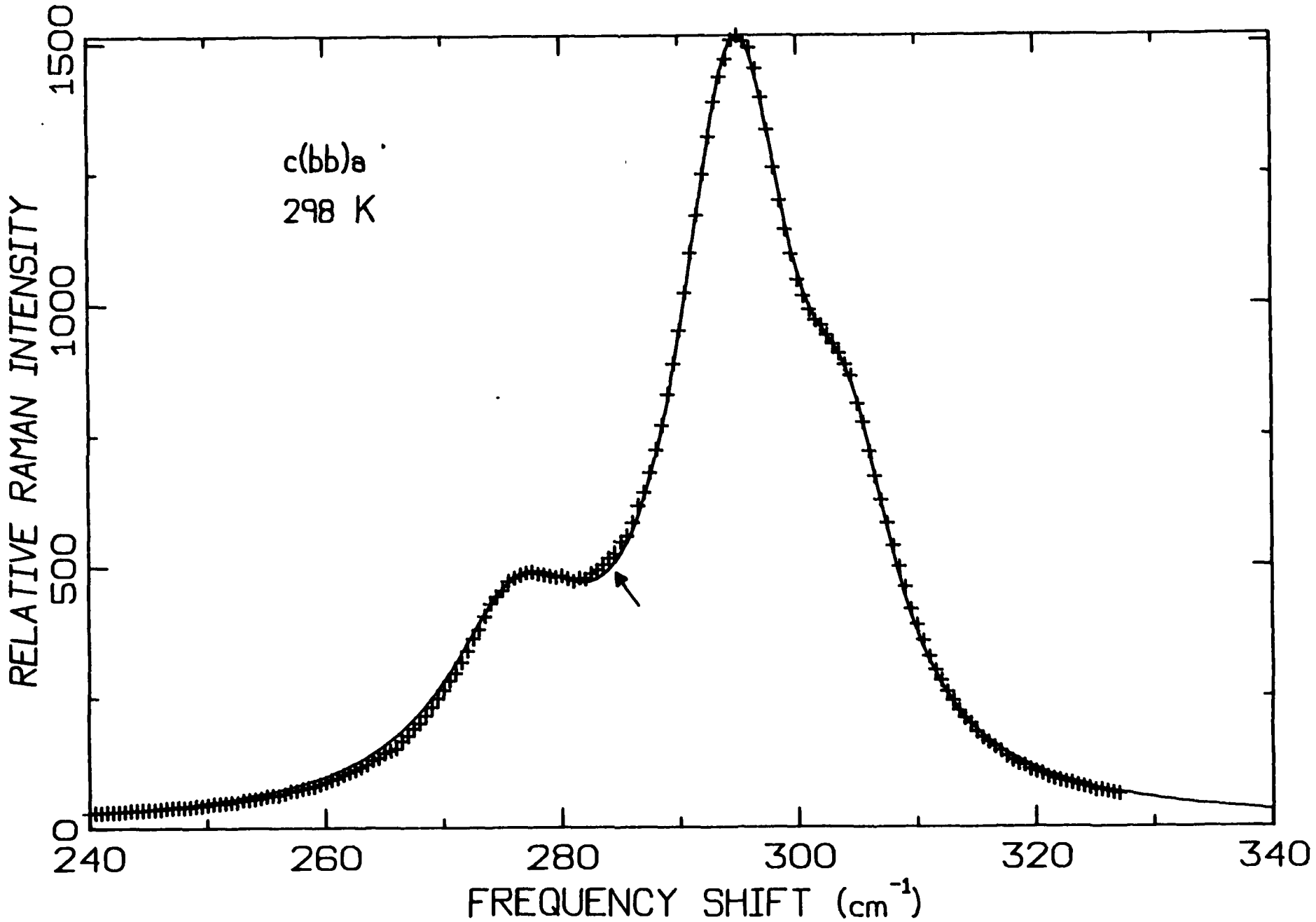
c(bb)a
298 K
RELATIVE RAMAN INTENSITY
0
500
1000
1500
240
260
280
300
320
340
FREQUENCY SHIFT (cm^{-1})

6c

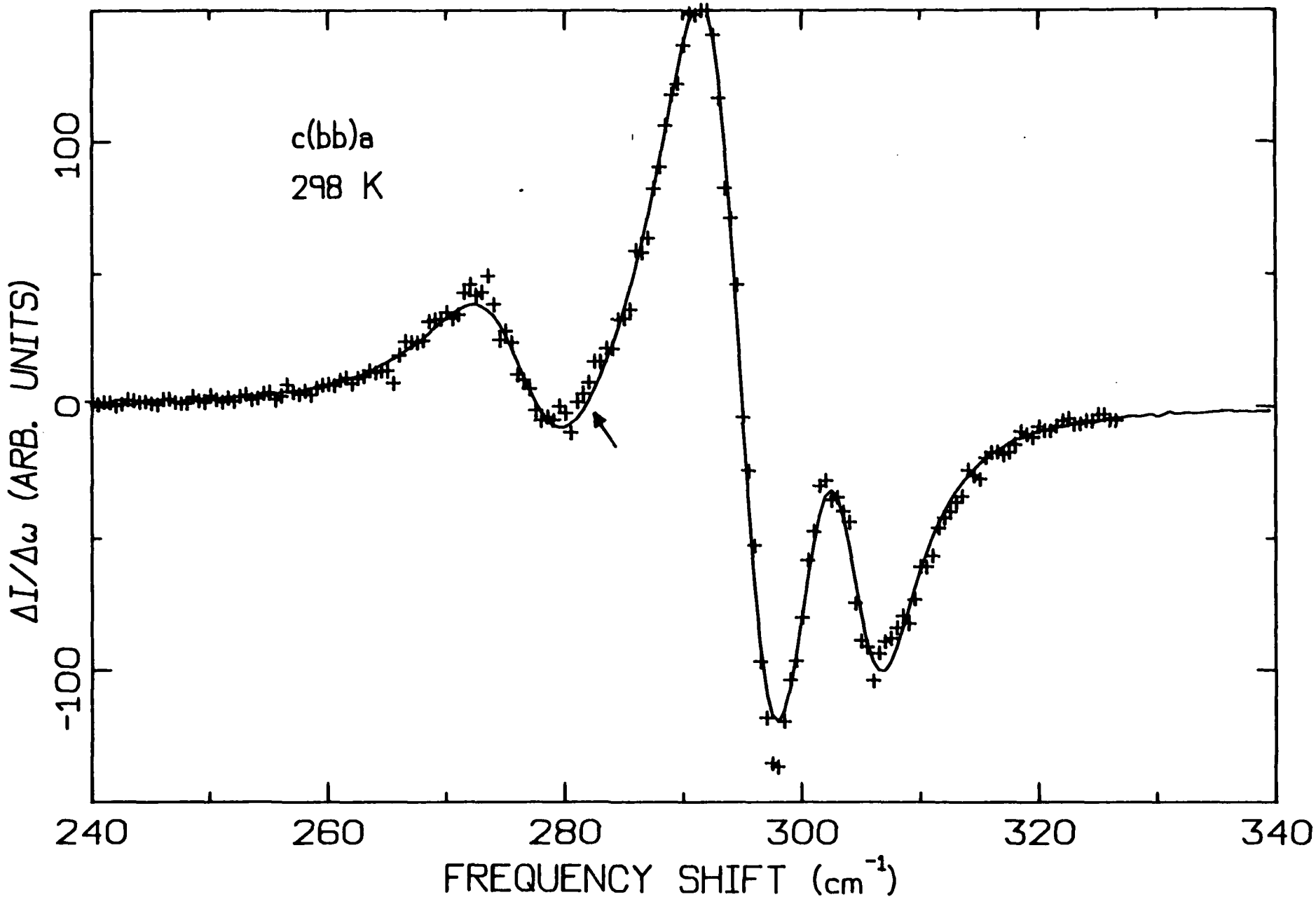
c(bb)a
298 K
100
0
-100
ΔI/Δω (ARB. UNITS)
240
260
280
300
320
340
FREQUENCY SHIFT (cm⁻¹)

6c

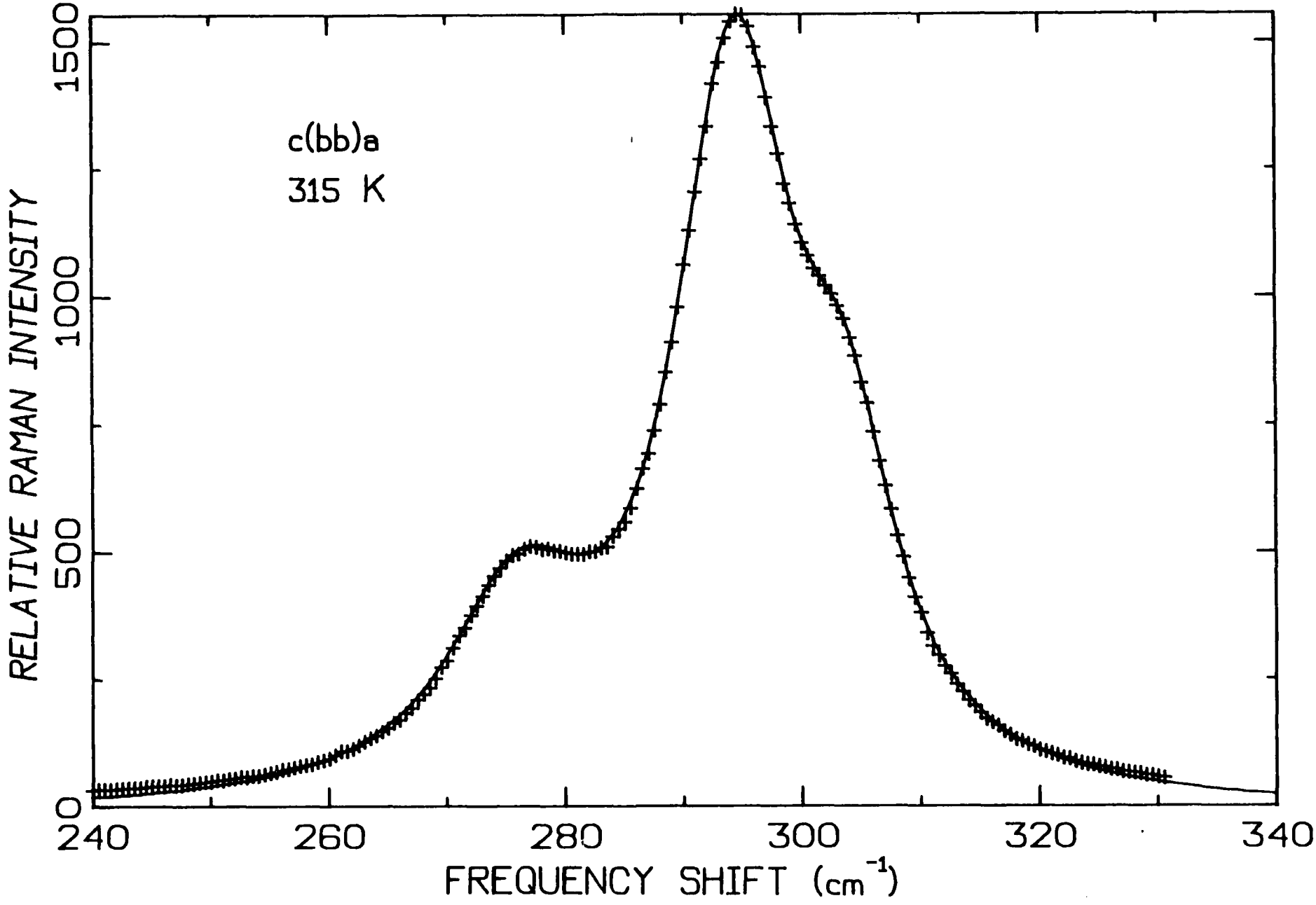
c(bb)a
315 K
RELATIVE RAMAN INTENSITY
0
500
1000
1500
240
260
280
300
320
340
FREQUENCY SHIFT (cm^{-1})

6d

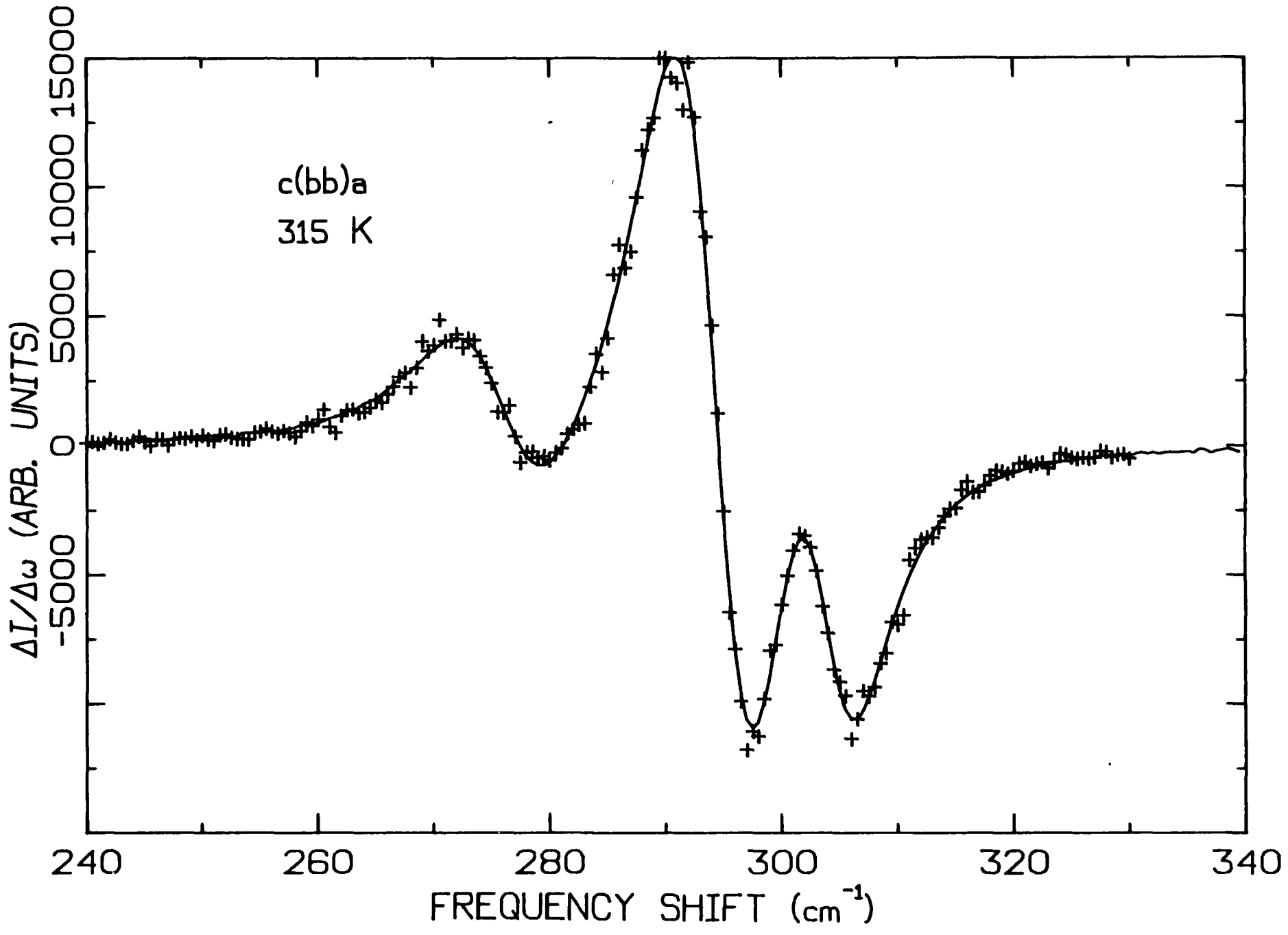
c(bb)a
315 K
ΔI/Δω (ARB. UNITS)
-5000
0
5000
10000
15000
240
260
280
300
320
340
FREQUENCY SHIFT (cm⁻¹)

6d

VII. Summary of Results and Conclusions

1. We have obtained complete, low background, Raman spectra for all of the scattering configurations corresponding to the factor groups of the D_{2h}^{16}, and C_{2v}^{9} point groups, for crystals of Rb_2ZnCl_4 at temperatures of 315, room, 200, 100, and 20 K.

2. We have developed a multi-Lorentzian fitting procedure that has made the identification of even strongly-overlapped Raman lines possible with reasonable precision and have correlated these spectra with recent theoretical calculations of the lattice dynamics of the ideal Pnam and $Pna2_1$ structure.

3. We have shown that these results are in agreement with an earlier qualitative model for K_2SeO_4 that was invoked to explain "anomalies" in its Raman spectrum (1). The basic assumption of that model, that some members of this family of materials are disordered from the ideal (X-ray observed) Pnam structure through weakly-coupled, small rotations of the ionic-molecular groups, is even more strongly evidenced in Rb_2ZnCl_4 than in K_2SeO_4. However, some differences of behavior of the Rb_2ZnCl_4 versus K_2SeO_4 remain unexplained; in particular, the explanation of the apparent disappearance of the 285 cm^{-1} mode above the incommensurate-paraelectric transition (302 K) was studied in detail but no conclusive interpretation was forthcoming from those experiments.

Another interpretation, however, now appears possible. Examination of the Raman lines calculated from theory, shown in Table VIII, reveals a degeneracy between the A_g line at 276 cm^{-1} and the

B_{1g}, B_{2g}, and possibly B_{3g} lines at 276, 274, and 267 cm^{-1}, respectively. The disorder in the chlorozincate sublattice will allow coupling between these degenerate lines so the interpretation in terms of specific factor groups, as we have presented above, could be invalid and may need to be replaced with a coupled-mode analysis.

In order to understand the chlorozincate internal mode spectra, some further development of our ideas for K_2SeO_4 is necessary. In that case, we (1) argued for relatively mild disorder, sufficient to destroy inversion symmetry and decouple the selenate motions. The data are not inconsistent with these ideas. Certainly, the number of frequencies observed, which differs from the number predicted by the selection rules for the perfect crystal, can be explained by this decoupling, and the intensities of the "forbidden" lines are of the order that would be produced by slight misorientations of the selenate ions.

However, within any model developed for the chlorozincate, this is not the case. The decoupling is still required but there are two new features with disturbing implications: the "forbidden" lines are far too strong to be explained by this simple model, and as compared with the theoretical values, the widths of the internal mode regions are of the order of a factor of two less.

In Fig. 7, we show stills from a molecular dynamics simulation of the ionic motions using Gordon-Kim potentials as we have done in earlier work (27). It can clearly be seen that, while the Rb^+ and Zn^{2+} sublattices manintain their integrity, the $ZnCl_4^{2-}$ tetrahedra are highly disordered rotationally.

Fig. 7 Results of molecular dynamics calculations on the Pnam structure. The dashed lines show the evolution of the chlorine atom positions.

a) three-cell projection

b) enlargement of section shown in (a).

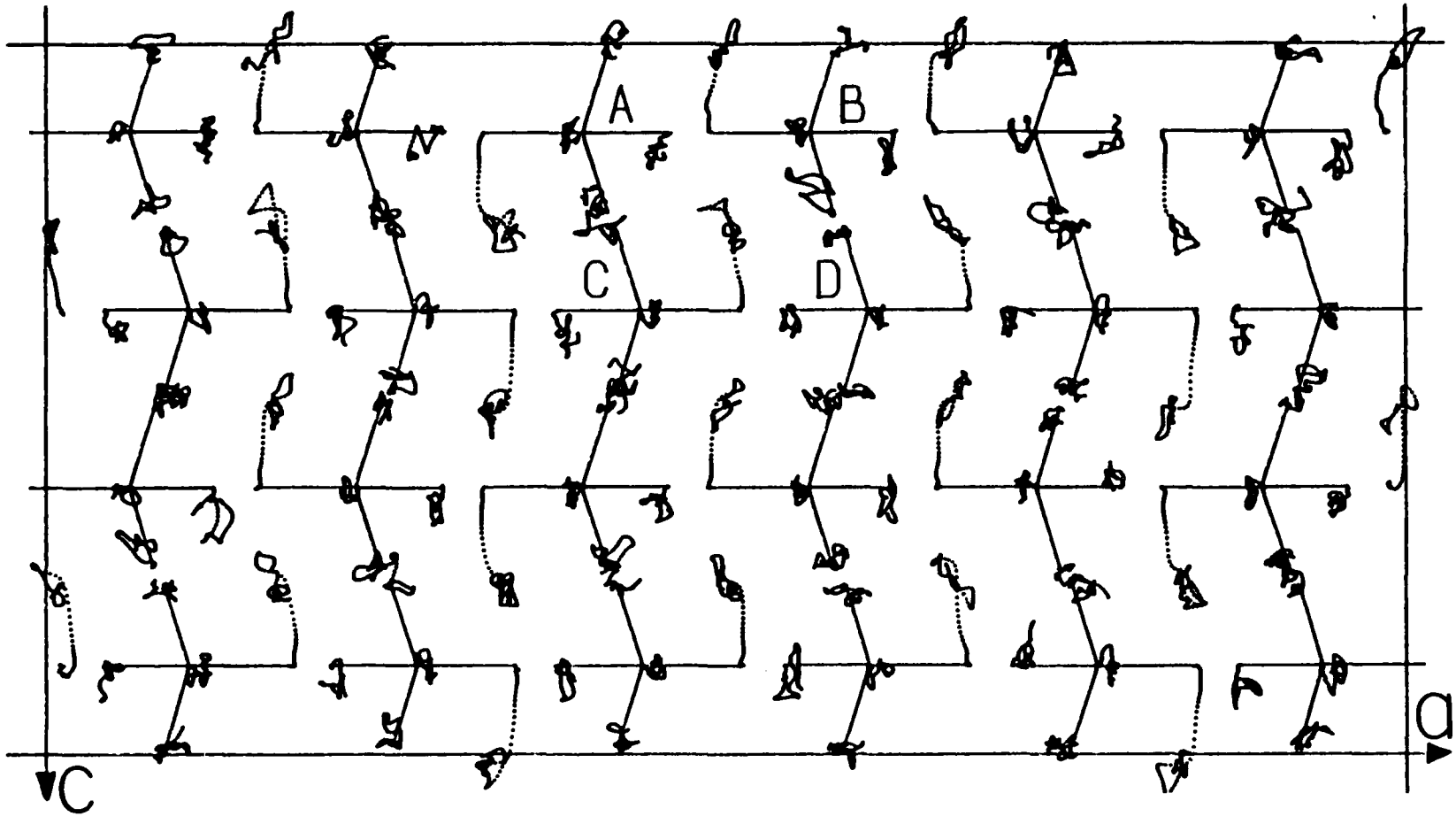

7a

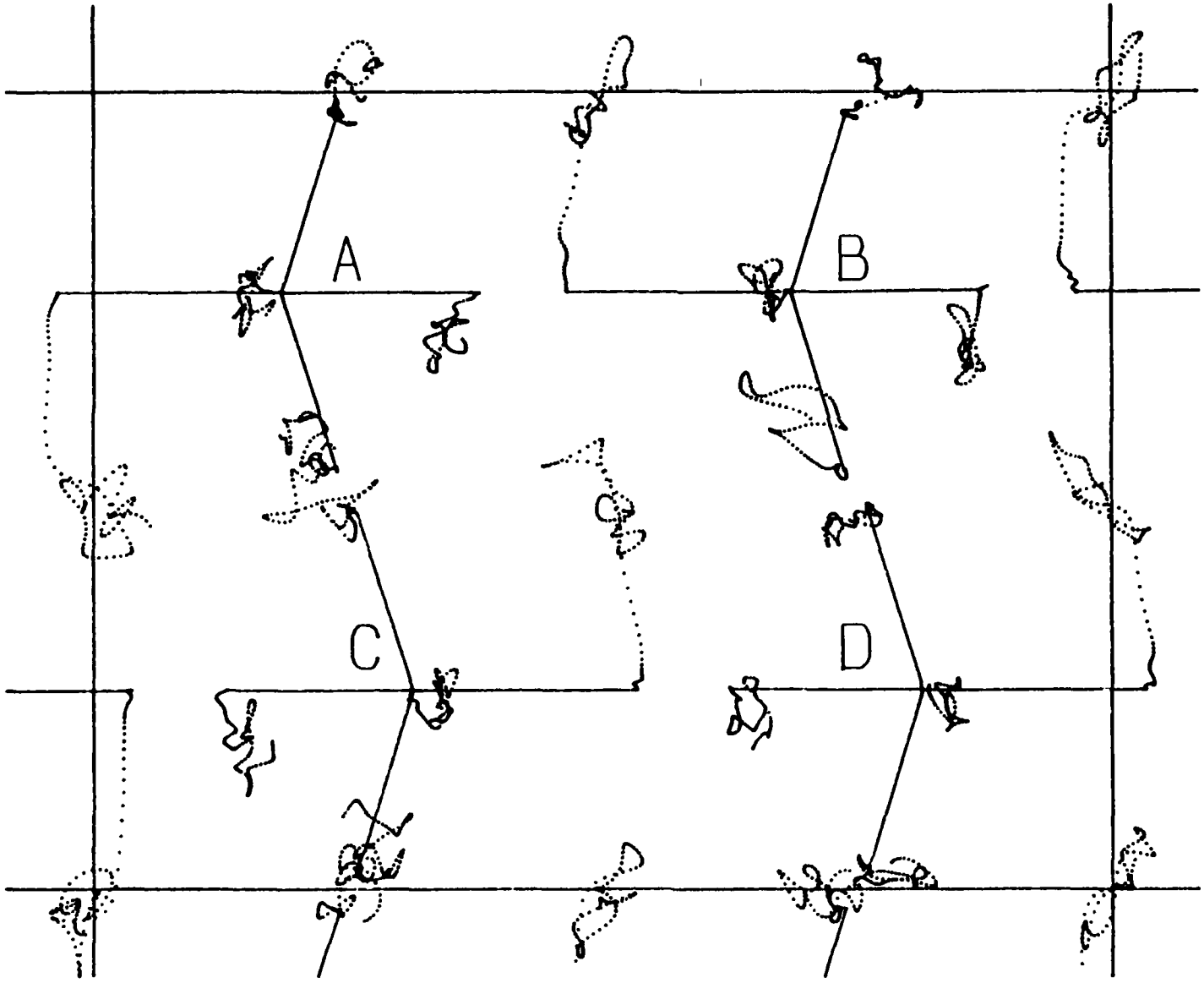

7b

AD-A172 712 ANALYSES OF THE RAMAN SPECTRA OF THE INCOMMENSURATE FERROELECTRICS RB(2)ZNCL(4) AND K(2)SEO(4)(U) NEBRASKA UNI LINCOLN V KATKANANT ET AL 30 JUN 86 2/2

UNCLASSIFIED ARO-19393.4-PH DAAG29-83-K-0080 F/G 7/4 NL

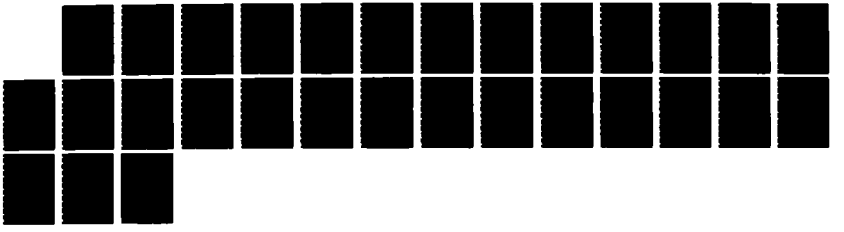

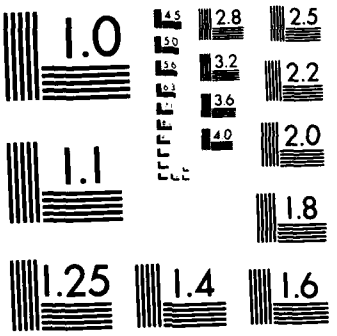

This provides an immediate explanation of the reduced splittings since, given their large freedom of movement, the tetrahedra will naturally tend to spend, on the average, a large part of their time in regions where their internal stresses and the associated splittings of the free ion degeneracies, are least. (Their almost complete decoupling, one from another, is also self evident). Thus it automatically follows that the observed crystal-field-induced splittings are going to be much less than those calculated for the ideal Pnam structure, both because the ions are less distorted, and because they are decoupled.

However, this $ZnCl_4^{2-}$ disorder also provides a ready explanation for the intensities of the "forbidden" lines which even these large misorientations cannot explain. Two factors are at work: the first affects both the bending and stretching regions while the second is peculiar to the stretching region in the chlorozincates.

The first factor is due to both relaxation and misorientation. The relaxation tends to restore the degeneracy of "allowed" and "forbidden" modes (e.g., the ν_4 doublet of the free ion splits into two singlets, one of which is "allowed" in (ac) and (bc) and the other is "forbidden" but "allowed" for other geometries). This partial restoration of degeneracy, having been produced by relaxation, then strongly enhances the tendency of the misorientation to produce mode mixing --the closer the frequencies of a set of uncoupled modes, the more the mode-coupling tends to produce a new set, each of which contains an equal mixture of the original set.

Clearly, this type of effect is in operation in the bending region --however, with different effects in different geometries since, in this region the effect of the ordered "backbone" of metal ions will be strong and will discriminate between them.

In the stretching region in the rubidium-chlorozincate, we have, in addition to the foregoing effects of relaxation and disorder, a unique effect arising from the near-degeneracy of one of the antisymmetric stretch modes (in B_{2g} and B_{3g}) with the symmetric A_g "breathing" mode.

Given this situation, the disorder and relaxation mode-mixing is complete and, as is clear from the data, the diagonal spectra are very similar and contain all four lines with comparable inte sity, at least below T_i. In fact, naively, one would expect all four lines to have approximately equal intensities --and this is indeed observed in Cs_2ZnCl_4 (28) which, however, does not show an incommensurate phase.

The fact that in Rb_2ZnCl_4 the 295 cm^{-1} line is the strongest (~50% of the total integrated intensity) rather than the lowest frequency of the quartet, as in K_2SeO_4, suggests that some other factor must be operative. Tentatively, we would argue that this could be due to correlations of the motions along "a" associated with the phase transition. These would affect motion, particularly antisymmetric stretch motion, parallel to "a" in a unique fashion which would be far more likely to enhance the associated scattering, since correlation, unless very specially selected, rarely reduces an effect already present.

Finally, these considerations can also provide a plausible explanation of the apparent rapid disappearance of the 289 cm^{-1} line in the A_g spectrum as T_i is approached from below. Evidently, this line is "pulled out" of the strong 295 cm^{-1} peak and its splitting is probably a strong function of the $ZnCl_4^{2-}$ misorientation: thus the loss of the ordered component, of these rotations, which probably occurs over this temperature range, could well reduce this splitting to the point where the line merges into the 295 cm^{-1} peak. A similar, but smaller effect may also be present for the 306 cm^{-1} peak.

This argument might also explain some of the systematic deviations of theory from experiment in the case of K_2SeO_4, referred to earlier, since their pattern is similar. However, the transfer of intensity from the ν_1 breathing mode to the other lines will not occur for K_2SeO_4 since there is not a similar accidental degernacy; again, this is in accord with the observed spectra.

Chapter 2

New Measurements on K_2SeO_4

In our previous work (1), we reported that the internal mode spectra, for Raman-scattering configurations representing the four factor groups of the D_{2h}^{16} point group symmetry of K_2SeO_4 and measured in its orthorhombic, paraelectric phase, consisted of the same nine frequencies within our precision of about plus or minus 2 cm^{-1}. We also observed no change on cooling except for line narrowing and a small downshifting in frequency of the whole spectrum. Since then, Unruh (29) has reported small frequency shifts between corresponding lines in the $B_{1g}(ab)$, $B_{2g}(ac)$, and $B_{3g}(bc)$ spectra. Also, in infrared spectra from the Laboratory of F. Gervais, reported by P. Echegut (30), additional lines are observed on cooling into the incommensurate phase. Consequently, we have repeated some of our measurements of the K_2SeO_4 spectra, with more careful frequency calibration, using appropriate known lines of the neon spectrum, and we have made these measurements at 140 K and 110 K to compare with the aforementioned infrared results.

I. INTRODUCTION

The high temperature (normal orthorhombic) phase II of K_2SeO_4 has a structure of the β-K_2SO_4 type and belongs to the space group D_{2h}^{16}-Pnam (Z=4). It transforms to an incommensurate phase III at 129 K and then undergoes a lock-in transition to a commensurate phase IV with space group C_{2v}^{9}-$Pna2_1$ at the ferroelectric Curie point at 93 K (31). In phase III, this crystal has the incommensurate superstructure whose lattice parameter is almost, but not exactly, tripled along the paraelectric orthorhombic "a"-axis. In the commensurate phase IV, it is an improper ferroelectric with spontaneous polarization along the c-axis and its cell side is exactly tripled along the paraelectric "a"-axis. This crystal has been extensively investigated, both experimentally (1) and theoretically (20,32-34) because of the considerable interest in revealing the mechanisms responsible for the successive phase transitions, including the appearance of the incommensurate structure and the lock-in transition. Infrared and Raman spectroscopy are important tools for studying the soft modes responsible for these structural phase transitions. Recently, Echegut et. al. (30) reported that additional lines may be seen on cooling to just below 129 K in the infrared B_{1u} and B_{3u} spectra. There are three additional external modes and one additional internal ν_3 mode whose intensities increase with decreasing temperature in both the incommensurate and ferroelectric phases without any significant discontinuity at T_c = 129 K. Also, as mentioned previously, Unruh (29) has reported small frequency shifts of the corresponding lines in different polarizations in the internal modes.

Since these effects were not observed in our former Raman measurements, we have undertaken more careful measurements using the laser line, and two neon lines at the beginnings of the external and internal mode regions for frequency calibration. In addition, we have carried out a more careful data analysis to determine the actual peak frequency.

II. EXPERIMENT AND EXPERIMENTAL RESULTS

Single crystals of K_2SeO_4 were grown by slow evaporation of an aqueous solution. The samples were cut in untwinned regions having good optical quality and suitable for polishing into right-angle prisms with sides parallel to the orthorhombic axes. The measurements were made by using a single frequency, Ar-ion laser line at 488.0 nm as a light source and at 100 mW. Raman spectra were measured at 140 K in all appropriate polarization configurations, and with all three pairs of incident and scattering axes (parallel to crystal axes) for each polarization configuration. For example, measurements of a(bc)b, c(bc)b, and c(bc)a were made. These were then compared and any differences observed indicated the importance of polarization leakage. Moreover, Raman spectra of a(bb)c, a(ba)c, a(cb)c, and a(ca)c were made at 110 K and additional measurements of a(ca)c were made at 85 K. As mentioned above, all these measurements have three reference lines included for frequency calibration: the laser line and two neon lines at 318.85 and 784.65 cm^{-1}, respectively. To maximize the precision of peak frequency determination, a linear least square fit to the frequencies of these reference lines was carried out for each measured scan. The neon lines for all the measurements are in agreement within ± 0.2 cm^{-1}. To determine the peak frequencies, a computer program was used that searches for successive data points near a change in intensity magnitude of the second-derivative of the measured Raman spectrum. It then selects the largest number from this group and uses

several points on each side to find the center frequency X as:

$$X = \frac{\sum x_i y_i}{\sum y_i} \qquad \ldots\ldots(1)$$

where x is the wavenumber of the data point and y is the Raman intensity in arbitrary units. The X in the formula is the corrected center frequency, according to the centroid quadratic formula given above. The calculation of X weights each point according to its magnitude. For some weak and narrow peaks, there are relatively few data points for the calculation since the data is recorded in 0.5 cm^{-1} steps. To have sufficient data to ensure that the calculated peak frequency is actually centered among these data points, a second-order polynomial function was used as an interpolation function to fit between data points with a 0.1 cm^{-1} coarse step. Thus, it was possible to achieve a precision in the value of the peak frequency of ± 0.1 cm^{-1} which is greater than the experimental precision of ± 0.5 cm^{-1}.

Comparison of these results for different incident and scattering directions for the same polarizations are in excellent agreement. These frequency measurements were already discussed and shown in Table VIII in the last chapter. Representative spectra are shown in Fig. 8a) and b).

Fig. 8 Raman spectra of K_2SeO_4 at 140 K for

a) 0-200 cm^{-1}, 300-460 cm^{-1} and 780-940 cm^{-1} of A_g modes(aa bb cc).

b) 0-200 cm^{-1}, 300-160 cm^{-1}, and 780-940 cm^{-1} of B_{1g}(ab), B_{2g}(ac), and B_{3g}(bc) modes.

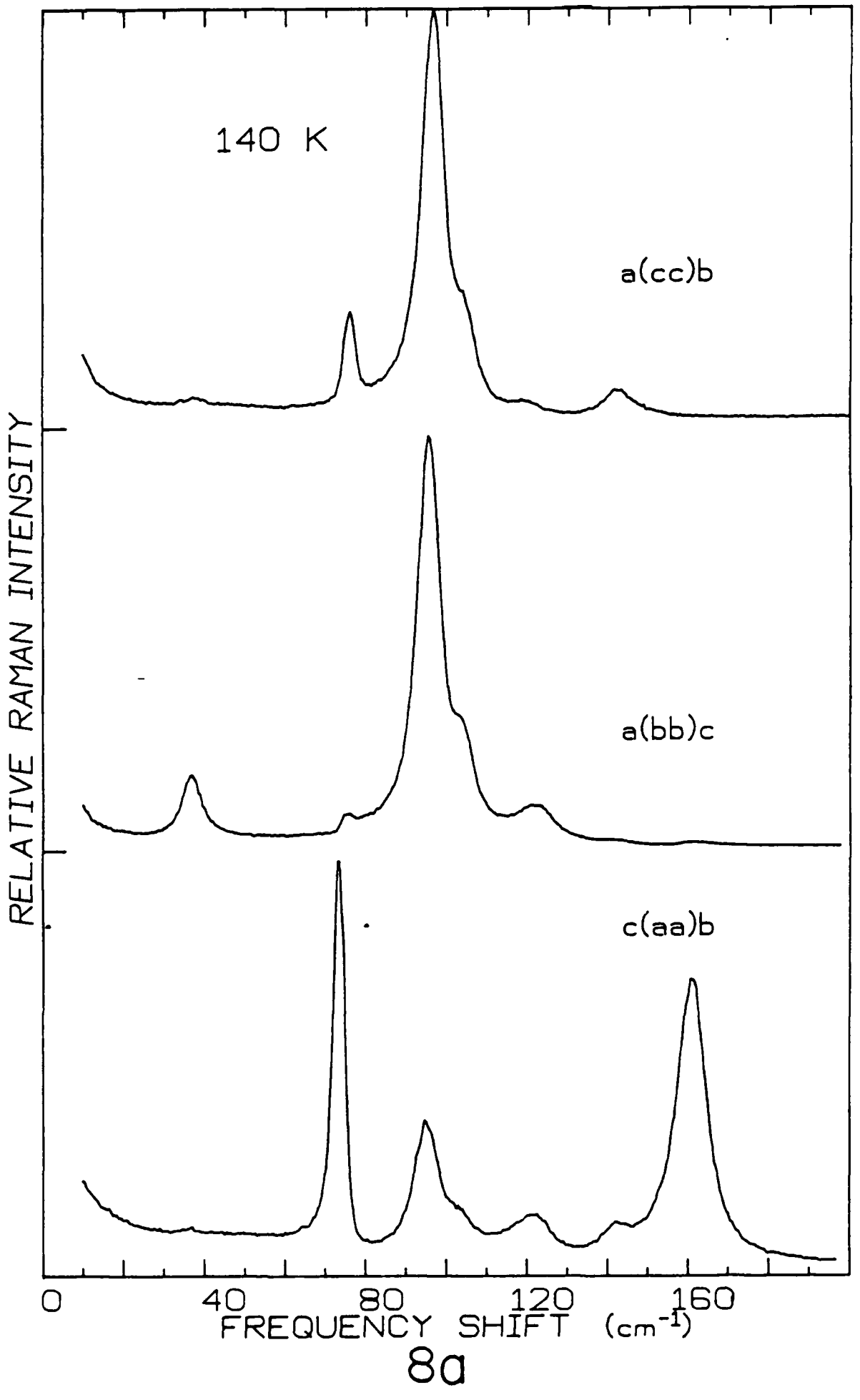
140 K
a(cc)b
a(bb)c
c(aa)b
RELATIVE RAMAN INTENSITY
0
40
80
120
160
FREQUENCY SHIFT (cm-1)

8a

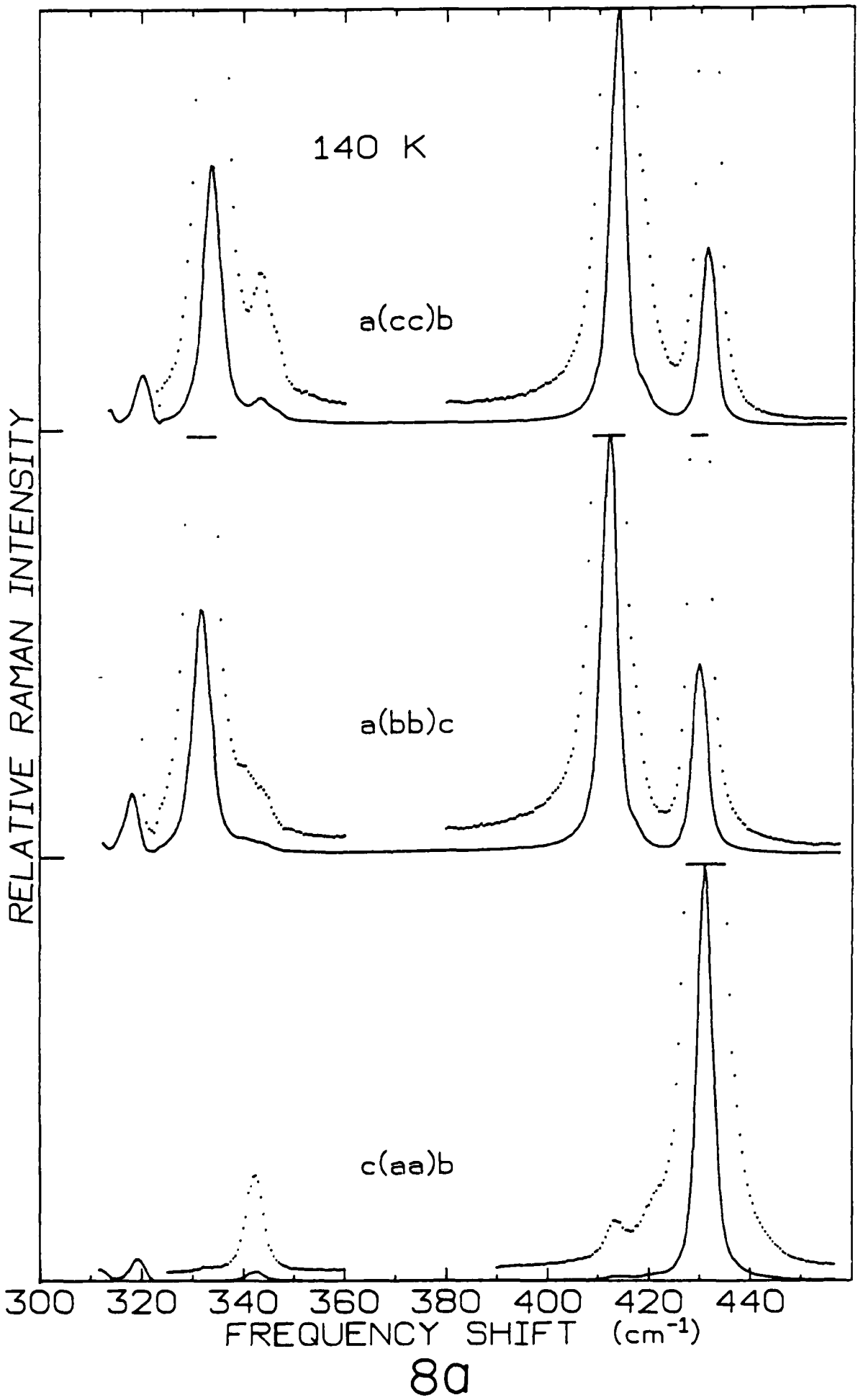
140 K
a(cc)b
a(bb)c
c(aa)b
RELATIVE RAMAN INTENSITY
300 320 340 360 380 400 420 440
FREQUENCY SHIFT (cm^{-1})

8a

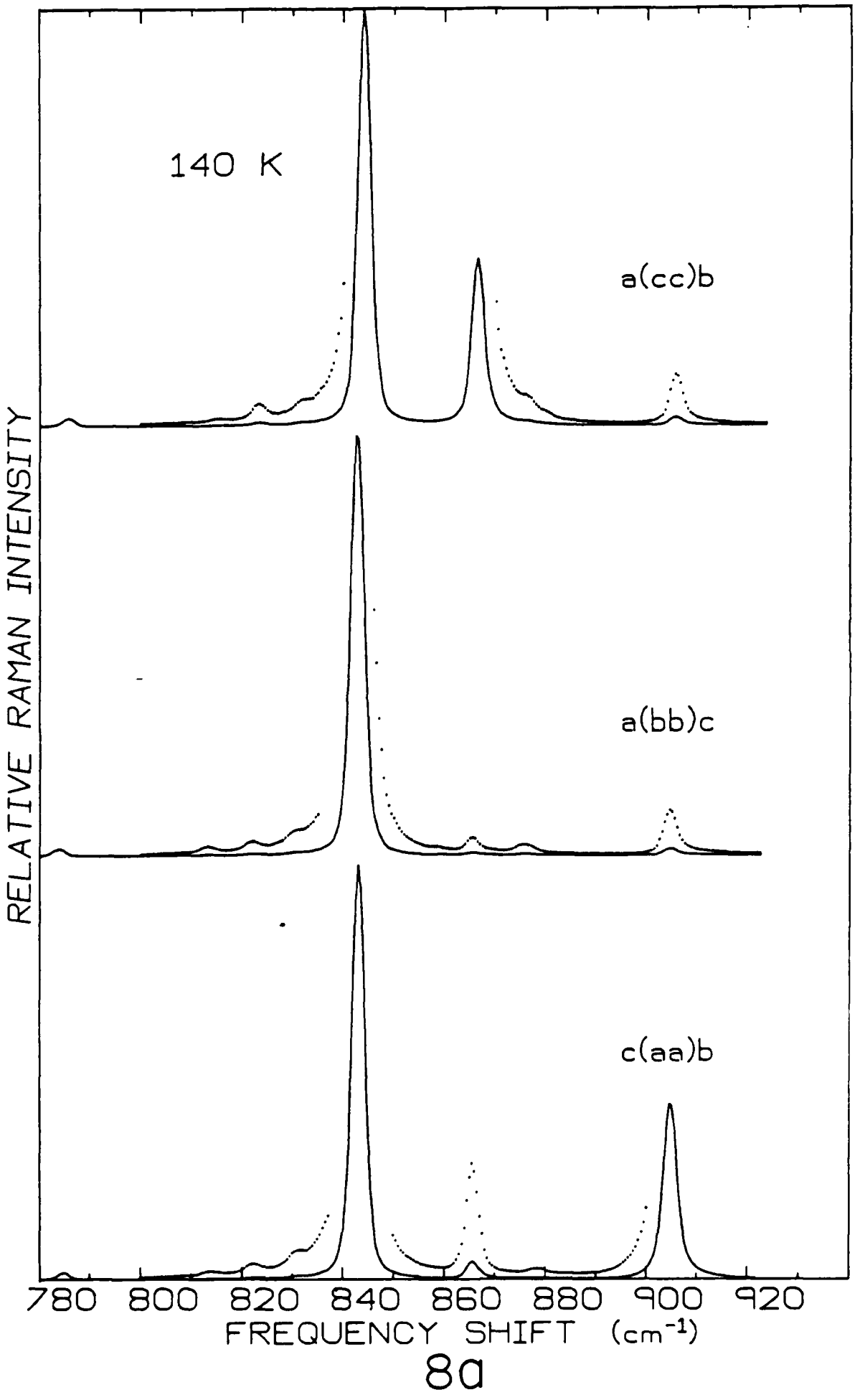
140 K
a(cc)b
a(bb)c
c(aa)b
RELATIVE RAMAN INTENSITY
780 800 820 840 860 880 900 920
FREQUENCY SHIFT (cm^{-1})

8a

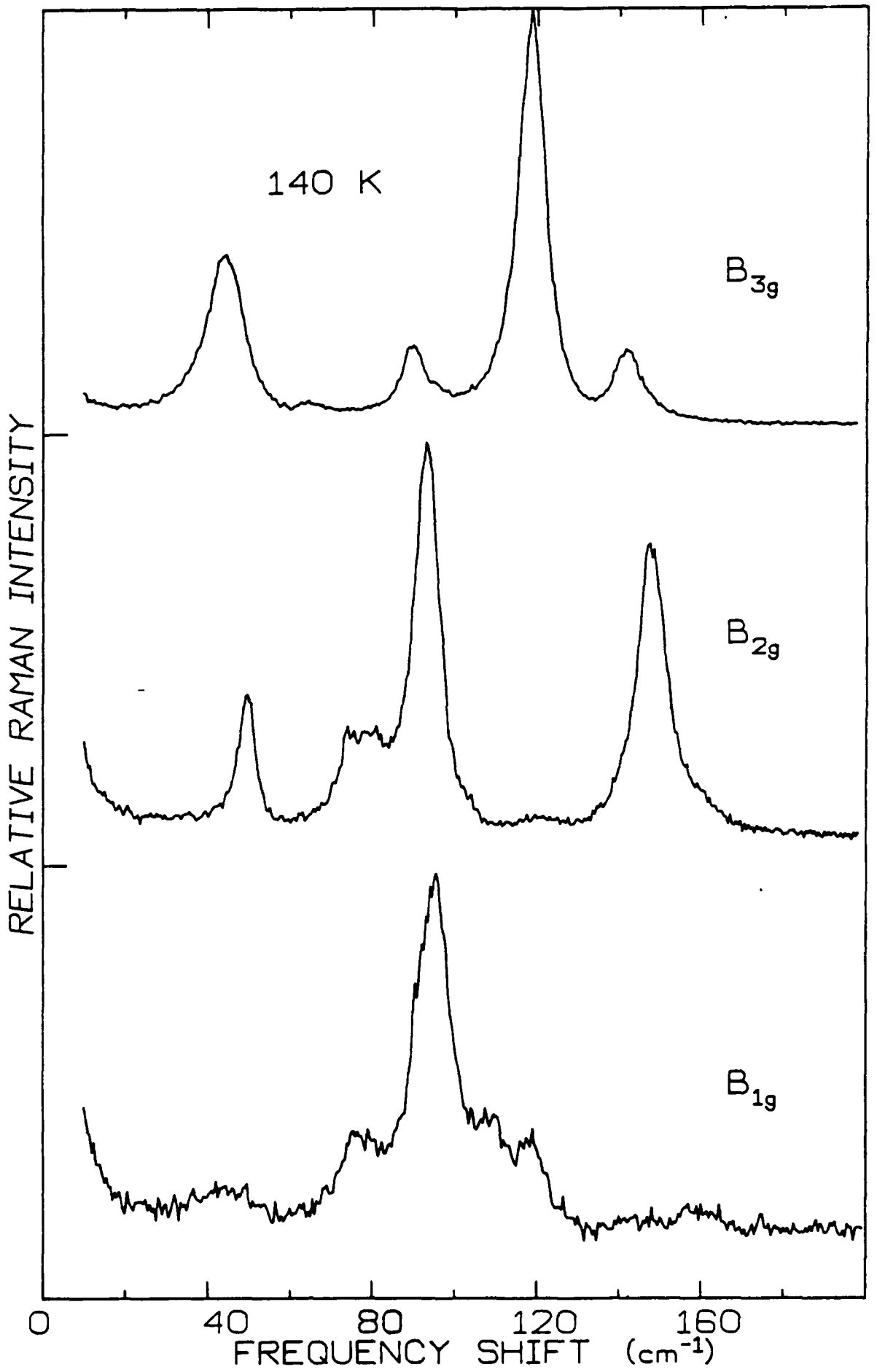
140 K
B_{3g}
B_{2g}
B_{1g}
RELATIVE RAMAN INTENSITY
0
40
80
120
160
FREQUENCY SHIFT (cm^{-1})

8b

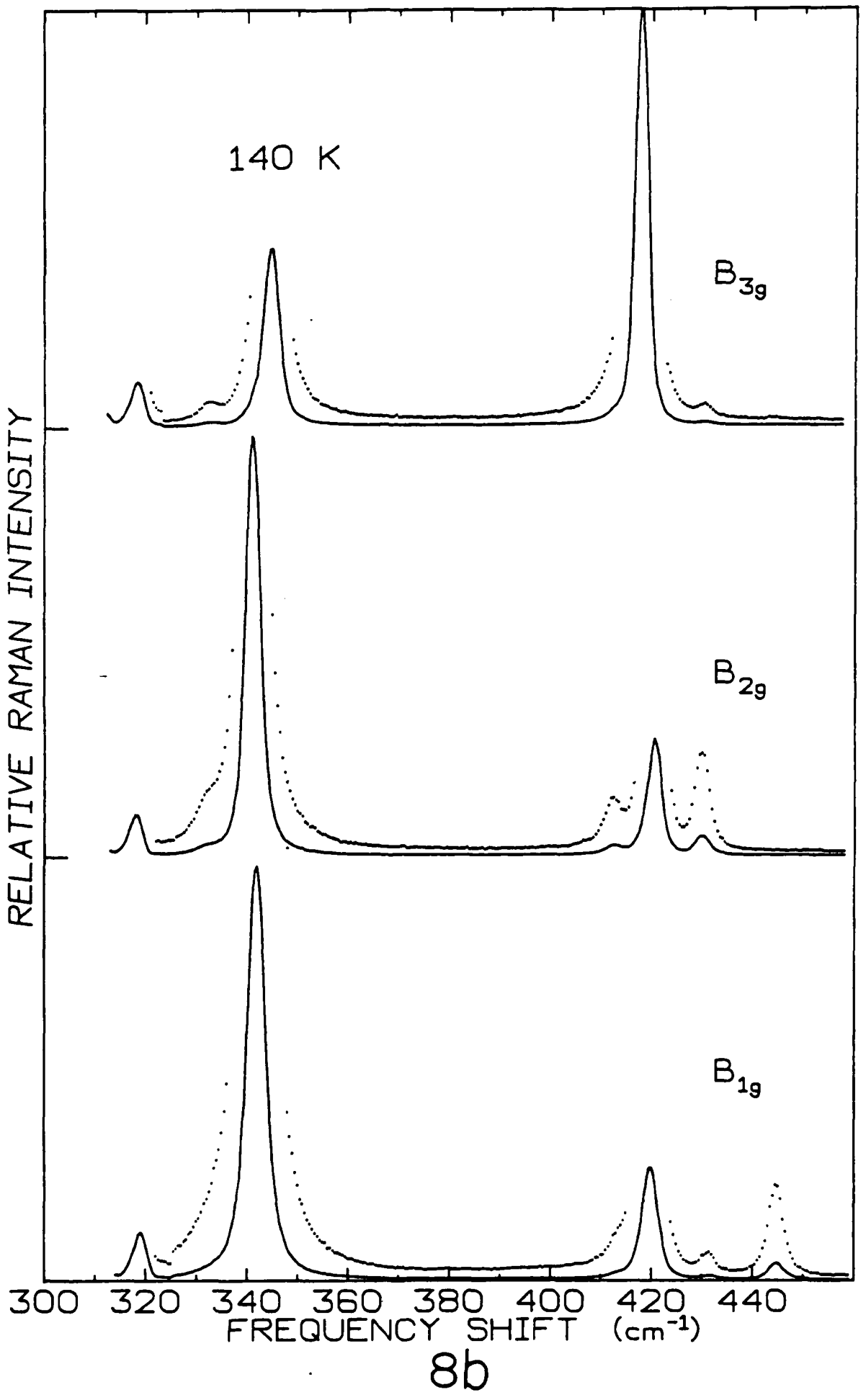
140 K
B_{3g}
B_{2g}
B_{1g}
RELATIVE RAMAN INTENSITY
300 320 340 360 380 400 420 440
FREQUENCY SHIFT (cm^{-1})

8b

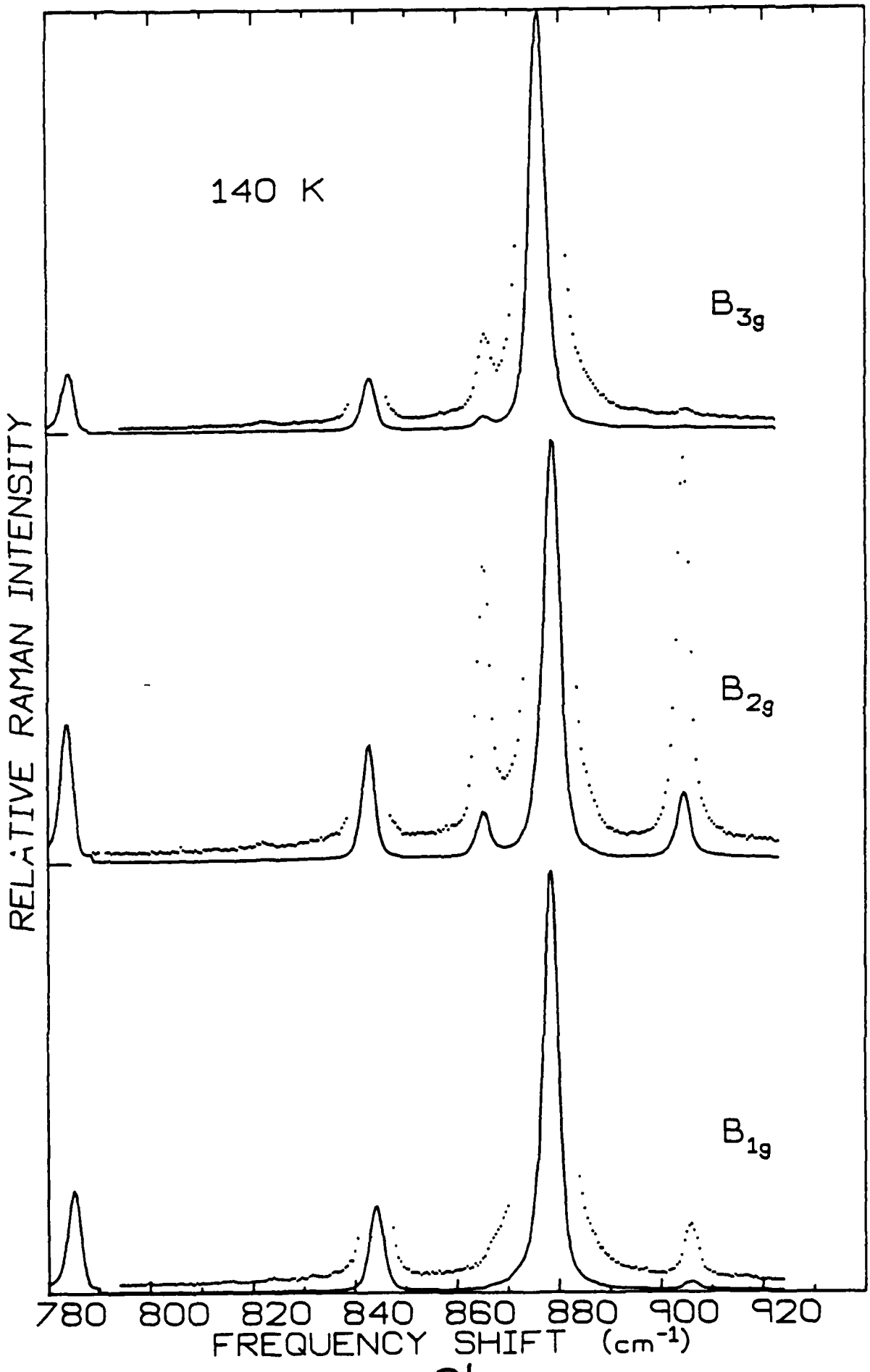
140 K
B_{3g}
B_{2g}
B_{1g}
RELATIVE RAMAN INTENSITY
780 800 820 840 860 880 900 920
FREQUENCY SHIFT (cm^{-1})

8b

Fig. 9 Comparison of Raman spectra of K_2SeO_4 at 140 and 110 K for the internal modes

a) 300 - 450 cm^{-1}, 780 - 940 cm^{-1} bb (A_g)

b) 300 - 450 cm^{-1}, 780 - 940 cm^{-1} ab (B_{1g})

c) 300 - 450 cm^{-1}, 780 - 940 cm^{-1}; 85 K spectra measured only for this mode also shown (B_{2g})

d) 300 - 450 cm^{-1}, 780 - 940 cm^{-1} (B_{3g})

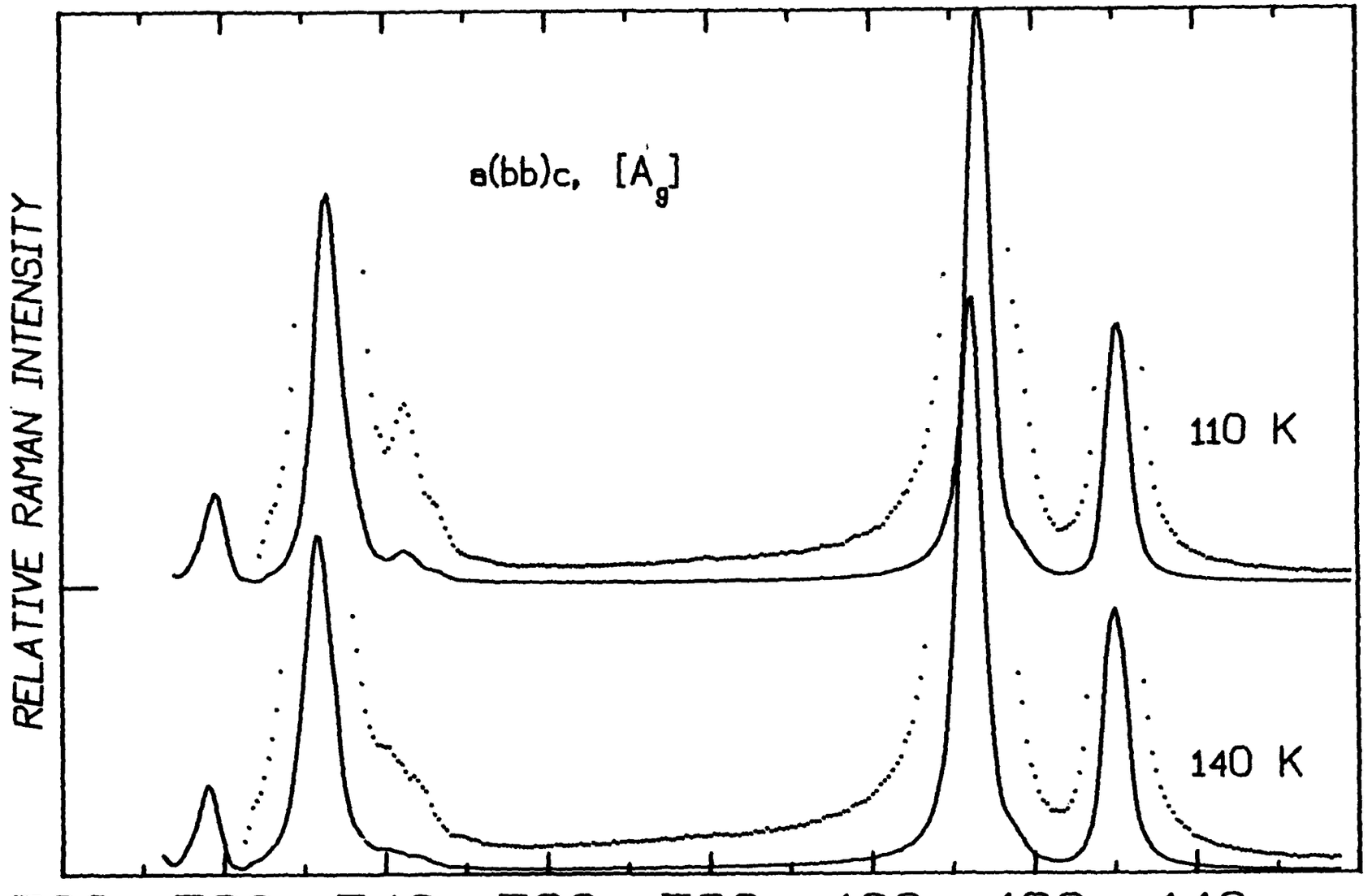
a(bb)c, [A$_g$]
110 K
140 K
RELATIVE RAMAN INTENSITY
300
320
340
360
380
400
420
440
FREQUENCY SHIFT (cm^{-1})

9a

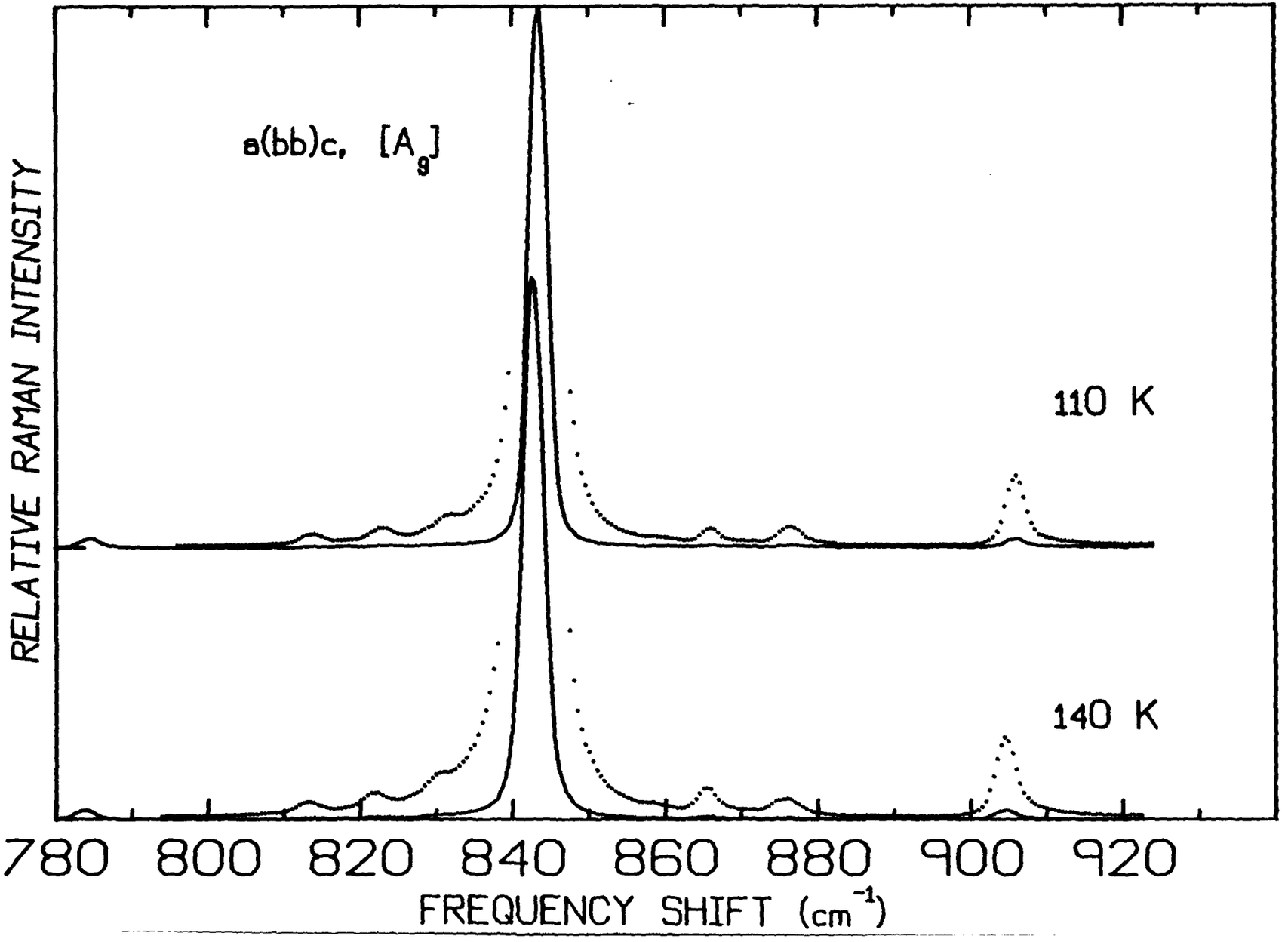
a(bb)c, [A$_g$]
110 K
140 K
RELATIVE RAMAN INTENSITY
780 800 820 840 860 880 900 920
FREQUENCY SHIFT (cm^{-1})

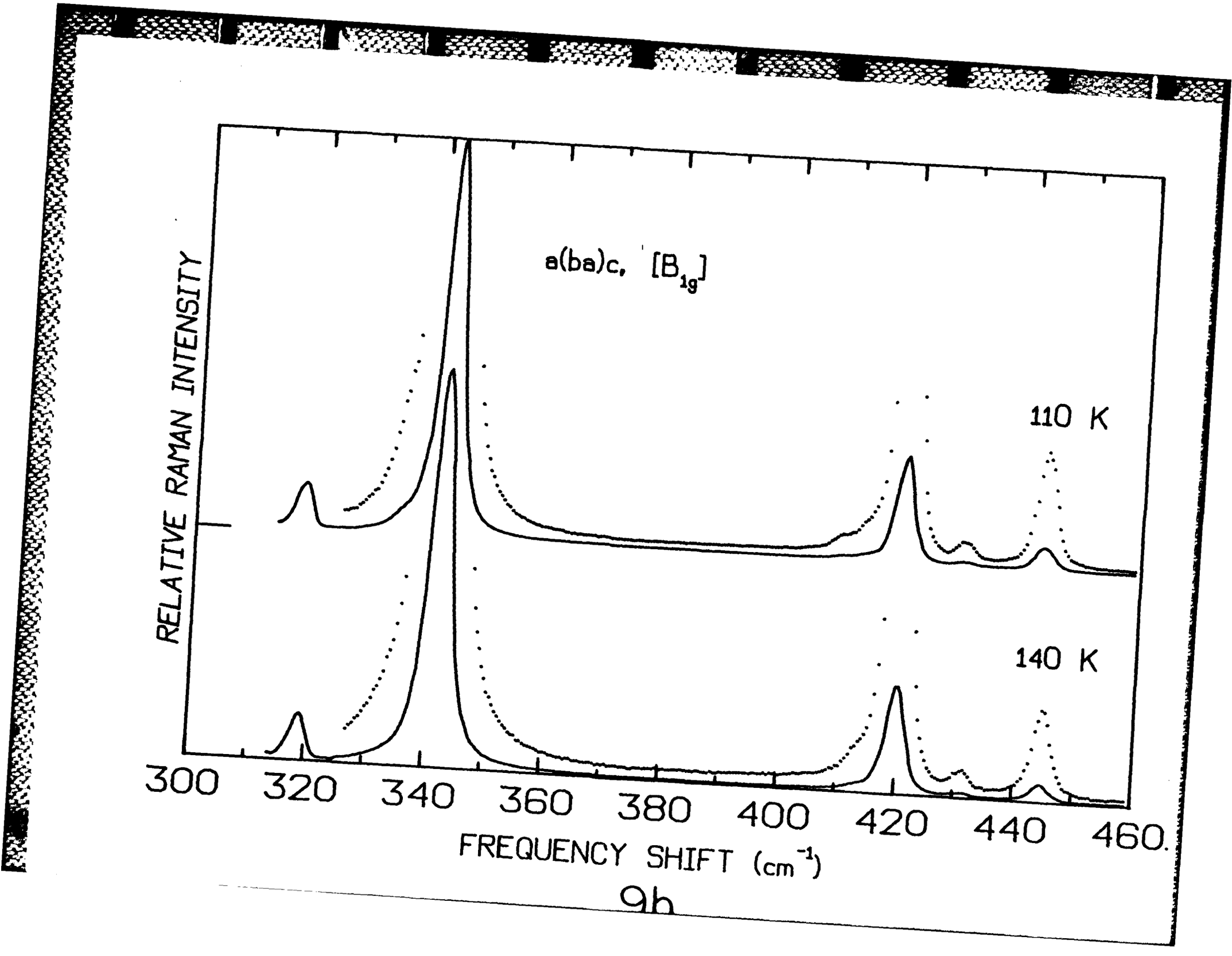
a(ba)c, [B1g]
110 K
140 K
RELATIVE RAMAN INTENSITY
300
320
340
360
380
400
420
440
460
FREQUENCY SHIFT (cm-1)

9h

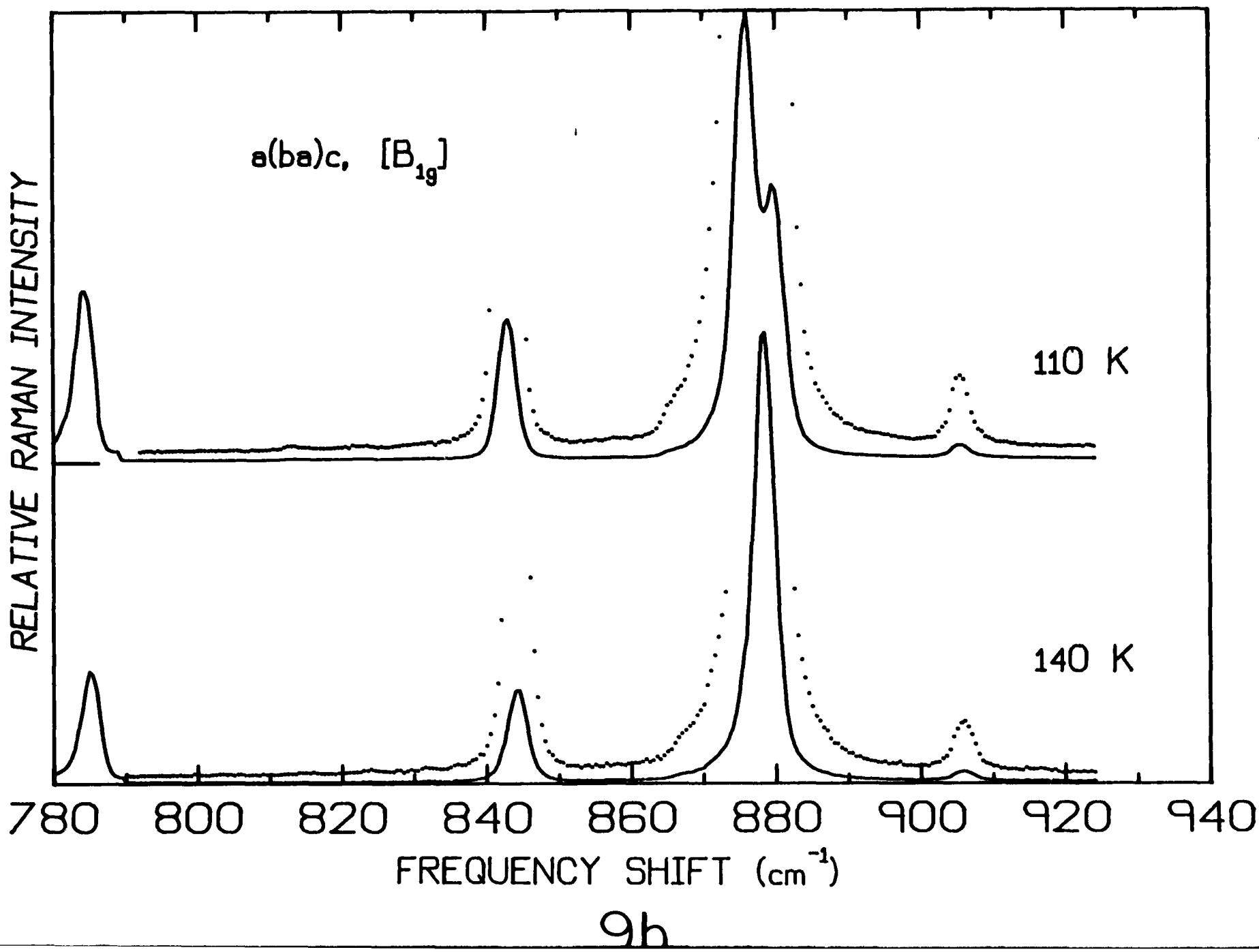
a(ba)c, [B1g]
110 K
140 K
RELATIVE RAMAN INTENSITY
780
800
820
840
860
880
900
920
940
FREQUENCY SHIFT (cm-1)

9b

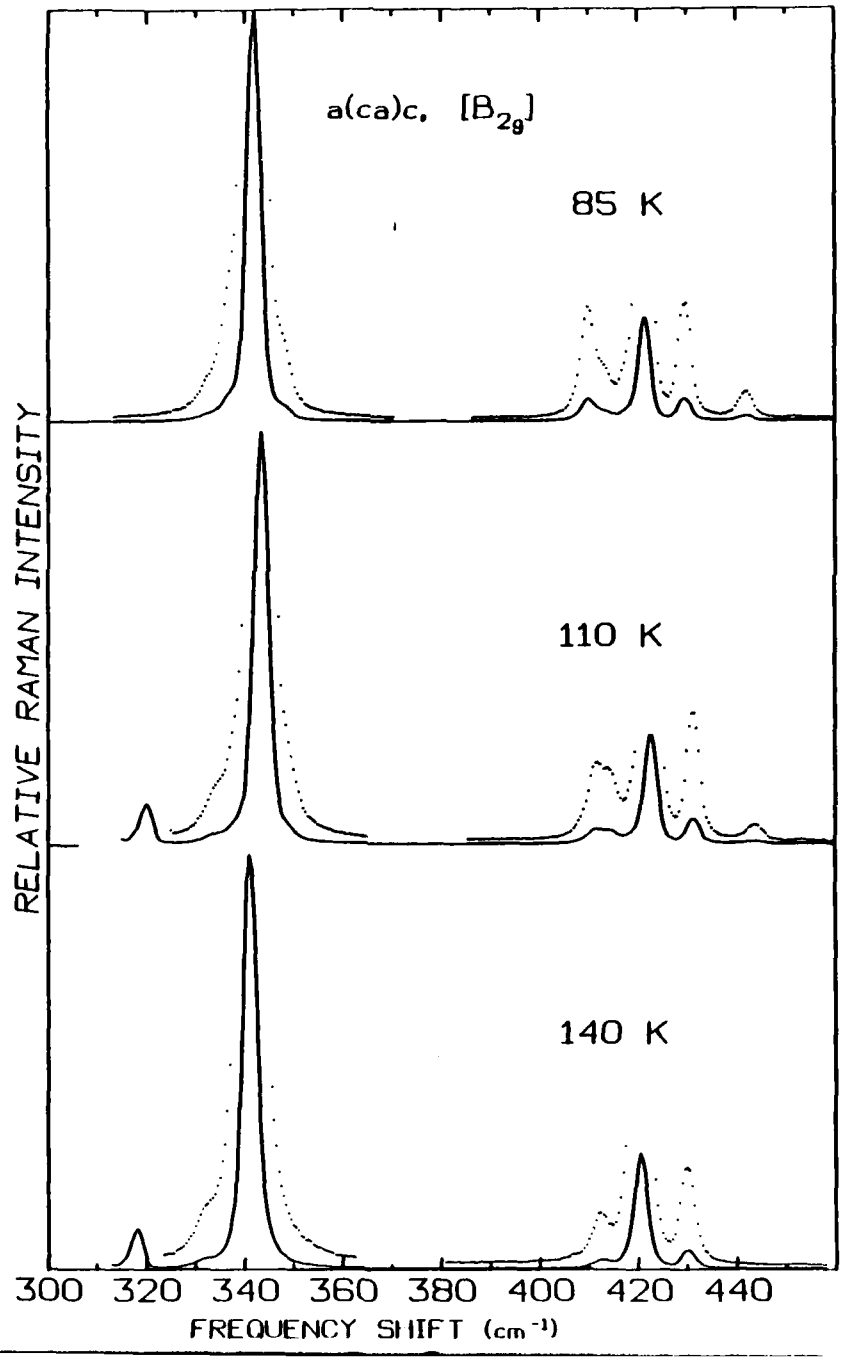
a(ca)c, [B2g]
85 K
110 K
140 K
RELATIVE RAMAN INTENSITY
300 320 340 360 380 400 420 440
FREQUENCY SHIFT (cm-1)

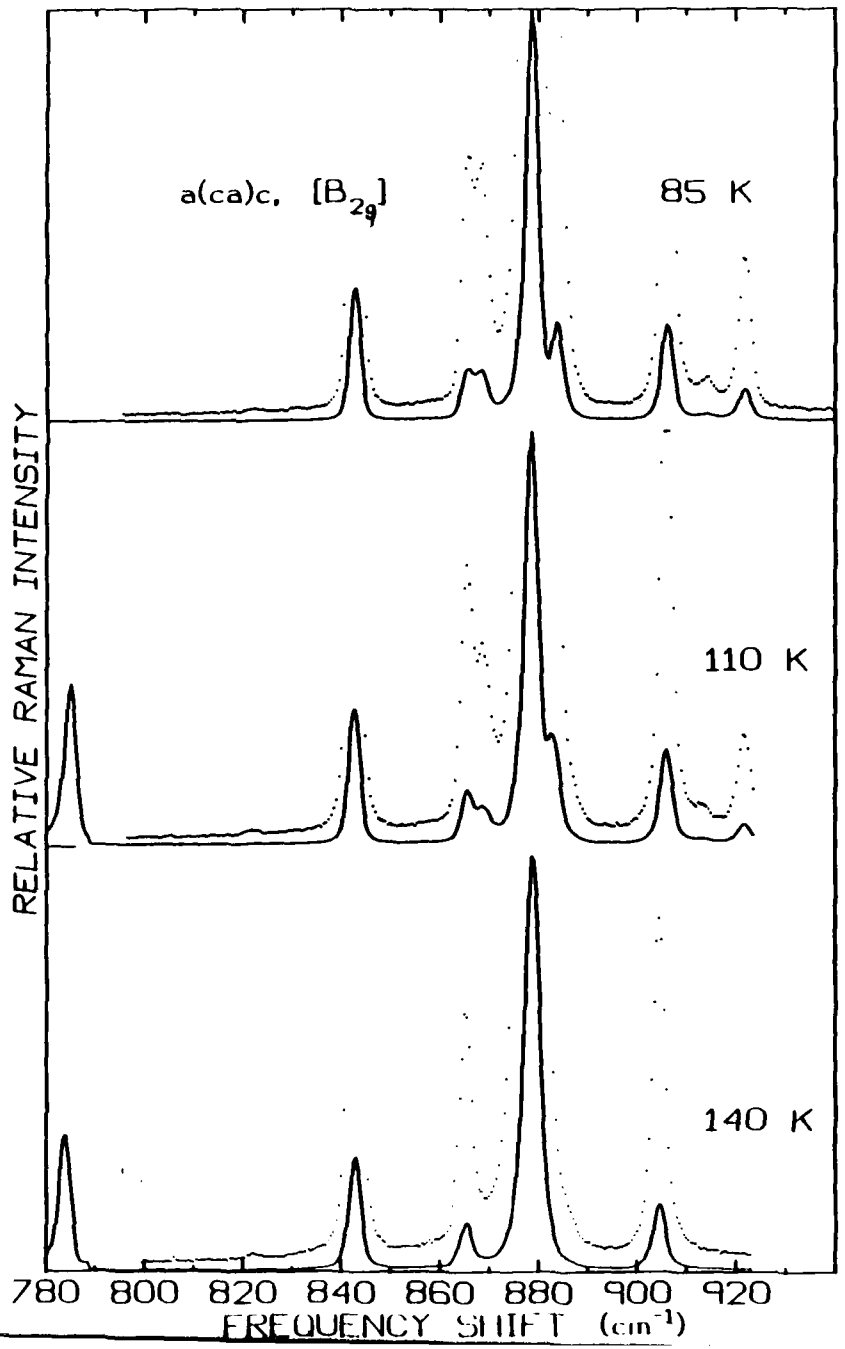
a(ca)c, [B2g]
85 K
110 K
140 K
RELATIVE RAMAN INTENSITY
780 800 820 840 860 880 900 920
FREQUENCY SHIFT (cm-1)

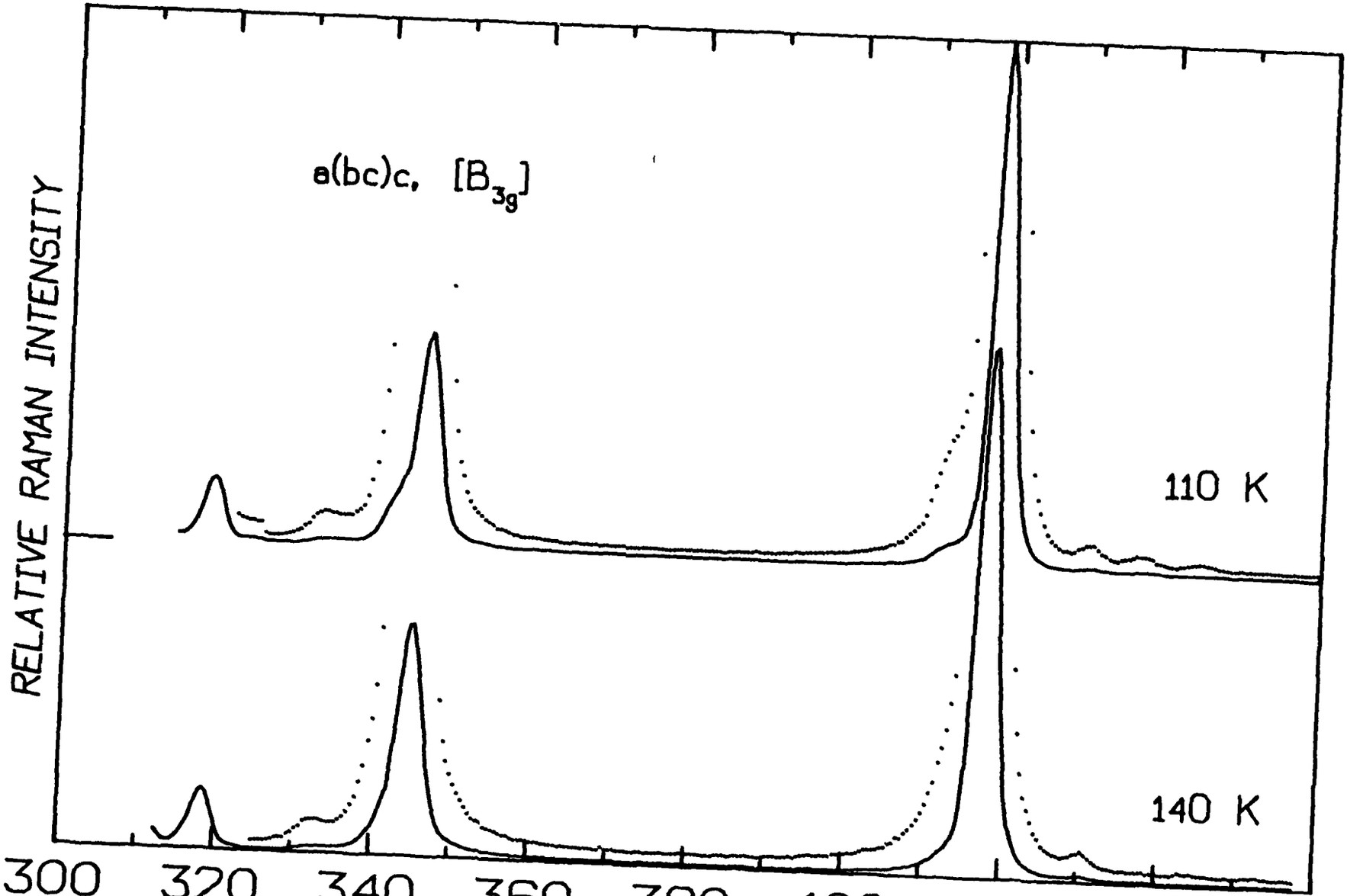
a(bc)c, [B3g]
RELATIVE RAMAN INTENSITY
110 K
140 K
300
320
340
360
380
400
420
440
460
FREQUENCY SHIFT (cm-1)

9d

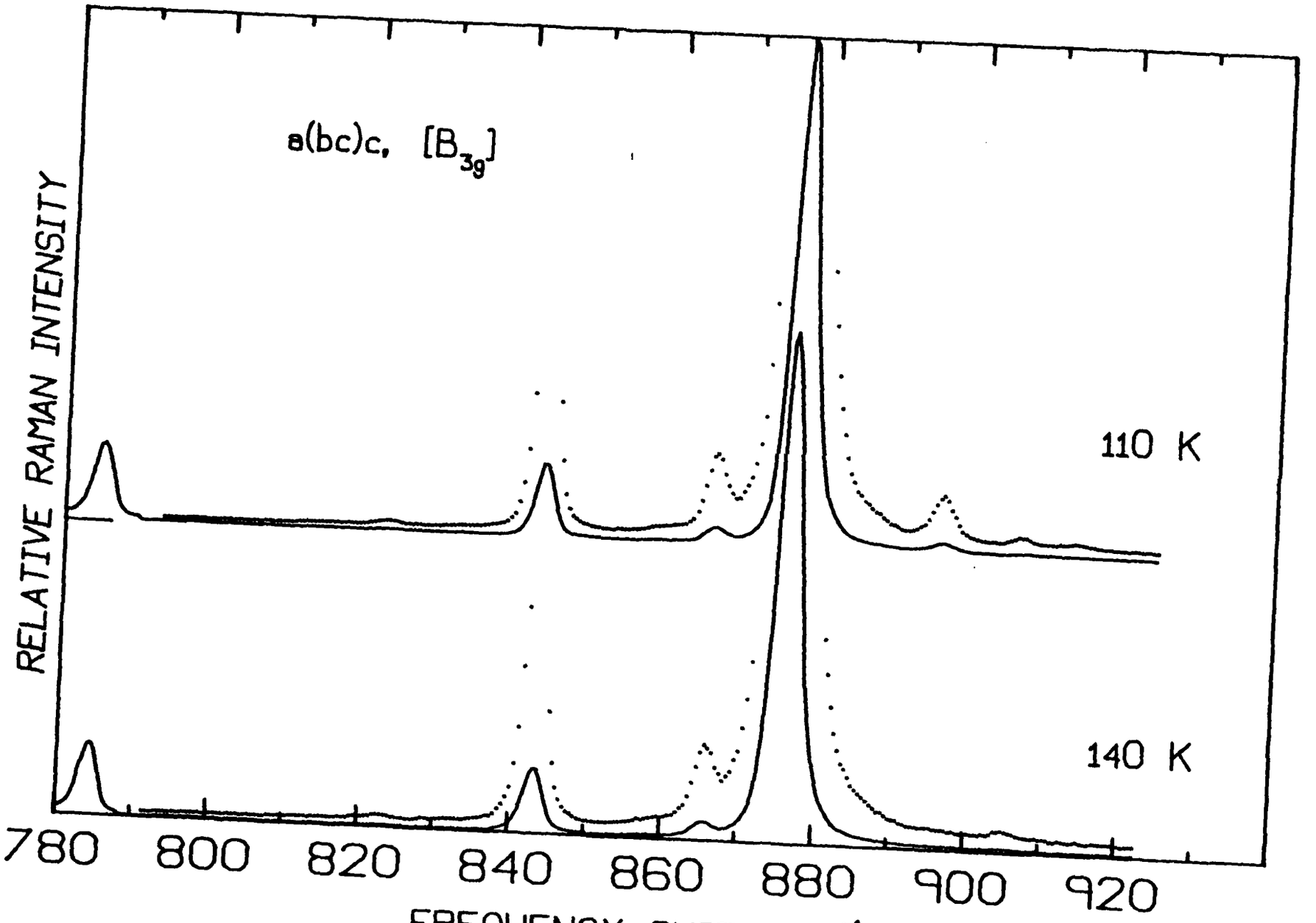
a(bc)c, [B3g]
RELATIVE RAMAN INTENSITY
110 K
140 K
780
800
820
840
860
880
900
920
FREQUENCY SHIFT (cm-1)

9d

III. DISCUSSION AND CONCLUSIONS

In the introduction to this Chapter, we stated two objectives: (1) to obtain more precise measurements of peak frequencies for comparison with those reported by Unruh (29), and (2) to determine if any line-splitting occurs in the internal modes on cooling into the incommensurate phase as observed in infrared spectra (30).

With the improved frequency calibration used here, we now find results that agree with Unruh as shown in Figures 8a) and 8b). However, we do not agree with Unruh that these small frequency differences negate, in any way, the disorder model we proposed (1). If K_2SeO_4 does have the Pnam structure, the expected splittings, from theoretical calculations (20), are listed in Table IX. Note from the Table that although the calculated B_g splitting near 875 cm^{-1} agrees with experiment, the A_g splitting does not. Also, the calculated splittings at lower frequency, e.g., near 440 cm^{-1} and 330 cm^{-1}, are considerably larger than measured. We, therefore, believe the results are inconsistent with the selection rules for the Pnam structure. Further, the disorder model does not preclude small frequency splittings of the order of those observed, as the selenate ions are certainly not completely free.

To meet our second objective, measurements were made at 110 K in the incommensurate phase. The relevant results, compared with the same spectra in the paraelectric phase are shown in Figures 9a)-9d) and Table XII. A similar splitting has been observed in infrared spectra in the laboratory of F. Gervais in France (30). The specific origin of this effect is still unknown but it must arise from the

onset of incommensurate behavior. For our purpose, it is important to know that the effect is observed in both the infrared-active and Raman-active modes.

TABLE XII

OBSERVED LINE SPLITTING OF RAMAN FREQUENCIES OF K_2SeO_4 FROM PARAELECTRIC (Pnam) TO THE INCOMMENSURATE PHASE

A_g	B_{1g}		B_{2g}		B_{3g}	
	140K	110K	140K	110K	140K	110K
332	weak	weak	332		332	
342-344	342		342		345	
412-413	vvw	clear	413		vvw	411
420	420		421		418	
430-431	431		431	431	431	431
				442 New		437 New
	444		453			
843-844	844		843		843	
866-867	vvw		866	866 868	866	sharper
876-878	877	875 880	879	878 883	876	876
						895 New
905-906	905		905	906 New	905	905
				913 922		913 New

Note that vvw stands for very very weak.

REFERENCES

1. N. E. Massa, F. G. Ullman, and J. R. Hardy, Phys. Rev. B 27, 1523 (1983).

2. S. Sawada, Y. Shiroishi, A. Yamamoto, M. Takashige, and M. Matsuo, J. Phys. Soc. Japan 43, 2099 (1977); M. Wada, A. Sawada, and Y. Ishibashi, J. Phys. Soc. Japan 45, 1429 (1978); J. Phys. Soc. Japan 47, 1185 (1979); J. Phys. Soc. Japan 50, 531 (1981).

3. K. Gesi and M. Iizumi, J. Phys. Soc. Japan 46, 697 (1979).

4. V. Katkanant, P. J. Edwardson, J. R. Hardy, and L. L. Boyer, Submitted to Phys. Rev. Lett.

5. E. Francke, M. Le Postollec, J. P. Mathieu, and H. Poulet, Solid State Commun. 33, 155 (1980).

6. M. Quilichini, J. P. Mathieu, M. Le Postollec, and N. Toupry, J. Phys. (Paris) 43, 787 (1982).

7. J. Petzelt, A. A. Volkov, G. V. Kozlov, S. P. Lebedev, and J. P. Chapella, J. Phys. (Paris) 43, 1359 (1980).

8. P. Gunter, R. Sanctuary, and F. Rohner, Phys. Stat. Solidi A 70, 583 (1982).

9. I. N. Fleorv and I. M. Iskornev, Phys. Stat. Solidi A 60, K79 (1980).

10. K. Itoh, A. Hinasada, H. Matsunaga, and E. Nakamura, J. Phys. Soc. Japan 52, 664 (1983).

11. S. R. Andrews and H. Mashiyama, J. Phys. C 16, 4985 (1983).

12. M. Quilichini and J. Pannetier, Acta Cryst. B 39, 657 (1983).

13. P. Muralt, E. Voit, and R. Kind, Phys. Stat. Solidi B 119, K65 (1983).

14. R. Osredkar, S. Juznic, V. Rutar, J. Seliger, and R. Blinc, Ferroelectric 24, 147 (1980).

15. H. G. Unruh and J. Stromich, Solid State Commun. 39, 737 (1981).

16. P. Gunter, R. Sanctuary, F. Rohner, H. Arend, and W. Seidenbusch, Solid Stat Commun. 37, 883 (1981).

17. H. Mashiyama and H. G. Unruh, J. Phys. C 16, 5009 (1983).

18. K. Hamano, Toru Hishinuma, and K. Ema, J. Phys. Soc. Japan 50, 2666 (1981); J. Phys. Soc. Japan 49, 2278 (1980).

19. J. R. Duffey and R. D. Kirby, Rev. Sci. Instru 50, 663 (1979).

20. M. S. Haque and J. R. Hardy, Phys. Rev. B 21, 245 (1980).

21. R. Loudon, Adv. Phys. 13, 423 (1964); Adv. Phys. 14, 621 (1965); Proc. Roy. Soc. (London) A 275, 218 (1963).

22. R. F. Wallis and A. A. Maradudin, Phys. Rev. B 3, 2063 (1971).

23. K. Nakamoto, Infrared and Raman Spectra of Inorganic and Coordination Compounds, Wiley-Interscience, New York (1978).

24. Private communication.

25. K. Hillstrom, A FORTRAN Program Number Name:LMCHOL (June, 1976 Version); Applied Mathematics Division, Argone National Laboratory.

26. Y. Yacoby, A. Linz, J. Phys. Rev. B 9, 2723 (1974); Y. Ycoby, S. Yust, and W. W. Kruhler, Ferroelectrics 12, 117 (1976).

27. L. L. Boyer and J. R. Hardy, Phys. Rev. B 24, 2577 (1981).

28. O. P. Lamba and S. K. Sinha, Solid State Commu. 57, 365 (1986).

29. H. G. Unruh, Raman Spectroscopy-Linear and Non-Linear, Ed. J. Lascombe and P. Huong John Wiley, 1982.

30. P. Echegut, F. Gervais, and N. E. Massa, Phys. Rev. B 31, 581 (1985); Japan. J. Appl. Phys. 24, Supp. 2, 778 (1985).

31. M. Iizumi, J. D. Axe, G. Shirane, and K. Shimaoka, Phys. Rev. B 15, 4392 (1977).

32. R. A. Cowley and A. D. Bruce, J. Phys. C 11, 3577 (1978); A. D. Bruce, R. A. Cowley and A. F. Murray, J. Phys. C 11, 3591 (1978); and A. D. Bruce and R. A. Cowley, J. Phys. C 11, 3609 (1978).

33. V. Dovorak and J. Petzelt, J. Phys. C 11, 4827 (1978).

34. C. de Lange and T. Janssen, J. Phys. C 14, 5269 (1981).

END

11-86

DTIC